Vertical Forces on the Coupling of a Pusher Tug-Barge

by

David K. Mumford

B. Sc. (Mathematics) University of British Columbia
B. A. Sc. (Mechanical) University of British Columbia

A THESIS SUBMITTED IN PARTIAL FULFILMENT OF

THE REQUIREMENTS FOR THE DEGREE OF

Master of Applied Science

in

THE FACULTY OF GRADUATE STUDIES

Department of Mechanical Engineering

We accept this thesis as conforming

to the required standard

THE UNIVERSITY OF BRITISH COLUMBIA

August 1993

In presenting this thesis in partial fulfilment of the requirements for an advanced degree at The University of British Columbia, I agree that the Library shall make it freely available for reference and study. I further agree that permission for extensive copying of this thesis for scholarly purposes may be granted by the Head of my Department or by his or her representatives. It is understood that copying or publication of this thesis for financial gain shall not be allowed without my written permission.

Department of Mechanical Engineering

The University of British Columbia
2075 Wesbrook Place
Vancouver, Canada
V6T 1W5

Date: 31 August 1993

Abstract

This thesis presents a method of calculating the vertical force on the coupling between a pusher tug-barge unit where the tug is able to pitch relative to the barge. Alternate methods assume that the hydrodynamic forces on each hull have no effect on the other hull. The method presented here assumes that there is a hydrodynamic interaction between the two hulls. A numerically-fast three-dimensional solution method (unified slender body theory) is used to develop this interaction between the two hulls in coupled modes of motion at zero speed. Only the heave and pitch modes are considered.

Experimental work was done on a coupled tug-barge model. The model was instrumented to determine the barge heave and trim, the relative pivot angle between the tug and barge and the vertical and horizontal pin forces. The experiments were run in head and stern sea conditions with two separate pivot locations. Only the horizontal forces are found to be non-linear. The peak vertical force occurs at wavelengths of $1.2l_{\text{Barge}}$ in head seas and l_{Barge} in stern seas. The amplitude of the hull motions increases with the wavelength except for the pivot angle which steadies at about $1.5l_{\text{Barge}}$. The pin force is more sensitive to the pivot location than the barge motions. The pivot angle is also sensitive to the pivot location.

Two numerical models of the tug-barge unit are compared to the experimental results. One model (Case 1) evaluates the two hulls separately while the second (Case 2) evaluates the hydrodynamic cross-coupling terms. Results show that both models underestimate the hull motions. The Case 1 model over-predicts the pin forces while the Case 2 model under-predicts them. The hydrodynamic cross-coupling terms are found to be significant. The Case 2 model is considered successful but needs to be refined numerically to improve on the solution.

Table of Contents

List of Figures

List of Graphs

Acknowledgment

Financial assistance for this project was provided by the Science Council of B.C. in the form of a GREAT award and by an NSERC scholarship. Polar Design Technologies and Robert Allan Ltd both provided very welcome assistance at various stages of the project. My wife Jeanette deserves the utmost thanks for her encouragement and assistance. I would also like to thank Dr. Bruce Dunwoody for his time and patience over the course of this work. Finally, last but not least, I must thank my fellow inmates of the Naval Architecture Laboratory: Ayhan Akinturk, Brian Konesky, Ercan Kose and Haw Wong.

Chapter 1

Introduction

1.1 General

Tug-barge systems are generally composed of a tug pulling one or more barges. However, recently an increasing number of these systems have been adopting pusher tugs due to the great economic advantages they offer. This is principally due to the lower drag (the barge is no longer in the propeller wash) with a resultant increase in operating speed and better fuel economy. A number of general references on tug-barge systems are included in section 1.2.3 and several others are included in the bibliography.

Originally the coupling between tug and barge was made using a push-knee fitted to the front of the tug and a set of lines to hold the tug against the stern of the barge and allow the barge to be manoeuvered. This method worked well with the barge trains used on the rivers in the southern U.S. and in Europe but was unable to handle open water conditions. Despite the development of notched barges and improved rope couplings these systems were still unusable in even moderately rough seas.

Better and stronger connections were needed to solve this problem. Initially most solutions consisted of a rigid connection between the tug and barge. This created a ship from the tug-barge combination while allowing it to be crewed as a tug and unmanned barge unit. Although these units were capable of withstanding much heavier seas than the earlier rope-connected systems the forces in the couplings were extremely large. In order to reduce the forces the couplings had to be allowed some relative freedom to move. The problem then became one of complexity and cost; the more degrees of

freedom were allowed the more difficult and expensive it became to control the relative motions. Most systems appear to have reached a compromise by allowing only relative pitching to occur. This is a simple engineering problem and moderately inexpensive. This solution also maintains a high degree of crew comfort.

Engineering problems are solved by assuming a maximum load on the coupling and designing the system to withstand this load. In the case of the pin-connected tug-barge a prediction of the loads on the coupling is extremely complex. The loading is sensitive to the masses and inertias of the tug and barge, the buoyancy forces on the hulls, the wave excitation forces (and their direction) and resultant movement of the hulls (providing a hydrodynamic added mass and damping) and the depth of the notch and subsequent pin location. As a result the prediction of the maximum force at the coupling requires a full evaluation of the fluid forces on the hulls. Robinson (1975) evaluated the coupling force by assuming that each hull had no effect on the other and as a result the hydrodynamic coupling terms between the tug and barge could be ignored. This thesis contends that these coupling terms are important and that an improved solution can be achieved by including them. It is assumed that in heavy seas where the maximum loads are expected to occur the tug and barge would keep station (corresponding to a zero speed condition) and that only heave and pitch modes need be considered.

A three-dimensional potential flow method was selected with the objective of achieving a numerically-fast solution. Newman's Unified Theory has shown good results for slender bodies and is very efficient. This theory combines the two-dimensional flow around a hull section with the three-dimensional flow around a slender body in a matching region where both are valid. The full three-dimensional solution is then

realized as a two-dimensional potential with an interaction coefficient to account for the radiation of waves from the full hull.

1.2 Literature Review

The literature search revealed a number of general articles on pusher tug-barge systems but a very limited amount of theoretical and experimental work. The search encompassed the COMPENDEX database as well as the older indices of engineering and scientific journals. In addition two local naval architecture firms, Polar Design and Robert Allan Ltd., were consulted for further information.

1.2.1 Experimental Work

Experimental work has been carried out at the David W. Taylor Naval Ship Research and Development Center in Bethesda, Maryland. One report "Experimental Research Relative to Improving the Hydrodynamic Performance of Ocean-Going Tug/Barge Systems" was published in four parts. Only parts 1, 2 and 4 were located. In part 1 Rossignol (1974) describes the selection and design of three types of pusher tugs; one with a rigidly connected tug/barge system and two with pin-jointed connections (one single screw and one twin-screw). In part 2 Rossignol (1975a) details the propulsion tests which were carried out using the models. In part 4 Robinson (1976) summarizes the results of the previous reports. Most seakeeping results presented in this report were for speeds of 16 - 18 knots although a zero speed case is mentioned. At 16 knots the rigidly connected system behaved similarly to a conventional ship and achieved its highest connection forces in the vertical direction. Testing at the same speed showed that the

pinned cases relieved the vertical forces but accentuated the longitudinal forces. Robinson also used a computer program to predict the vertical force and motion response in the pinned case. This program evaluated the hydrodynamic and hydrostatic forces of each model separately with the only coupling being the vertical forces and corresponding moments at the pin connection.

Rossignol (1975b) also conducted experiments with four flexibly connected barges (1/10 scale models of 200 ft. barges). Each pair of barges was joined by connectors permitting nearly complete relative pitch freedom and some relative heave but virtually no relative yaw, sway or roll freedom. The model tests were conducted for both the zero speed case in regular waves and for the forward speed problem in calm water. The most severe condition was observed at a 120° heading. All other headings showed very little barge motion or connector bending.

Donald Brown of Barge Train Inc. (1977) developed a computer program to define the dynamic response of a flexibly connected barge train. He expanded the hydrodynamic strip theory work of Salvessen, Tuck and Faltinsen (1970) to include elastically and kinematically coupled dynamic elements. The results include the pitch, heave, surge, sway, yaw and roll displacements and the forces in the connectors.

G. Van Oortsmerssen (1979), "Hydrodynamic Interaction between Two Structures, Floating in Waves", used experimental and computational results to analyze the hydrodynamic effects of two structures floating close to each other. The experimental results showed that the interaction effects on the hydrodynamic reaction forces become more significant as the structures were moved closer together. This could be shown as an oscillation of the added mass and damping coefficients about the single

structure results. The interaction effects were present throughout the frequency range and were more pronounced for horizontal than for vertical motions. These results were verified computationally.

1.2.2 Theoretical Work

The only closely related theoretical work found was by J. Bougis and P. Valier (1981). They computed the forces and moments in the rigid connections of an ocean going tug-barge system by using a three-dimensional hydrodynamic theory. These results were then successfully compared to the experimental results of Rossignol (1975).

The solution of the coupling forces between the tug and barge requires a fast and efficient three-dimensional solution method which will yield the hydrodynamic coupling terms between the two hulls. Unified slender body theory, first proposed by Newman (1978) in "The Theory of Ship Motions", derives the three-dimensional potential flow solution for a slender hull by using a matching function. The matching function provides a three-dimensional interaction between the two-dimensional solutions along the hull to give a full three-dimensional solution. "Strip theory" is used to find a near-field potential solution for the body while the slender body method gives the far-field potential. In "The Unified Theory of Ship Motions" (1980) Newman and Sclavounos expand this method for the heave and pitch motions of a slender ship moving with forward velocity in calm water. Newman and Sclavounos develop the matching function using a Fourier transformation of a "translating-pulsating" source. They include results for a Series 60 hull and a prolate spheroid with no forward velocity along with some forward speed

cases. Most results show excellent agreement with experimental and other three-dimensional solutions.

J.H. Mays' Ph.D. Thesis "Wave Radiation and Diffraction by a Floating Slender Body" (1978) deals specifically with the zero-speed case of unified slender body theory and includes results for non-symmetrical bodies. Mays compares results for several prolate spheroids of varying length to beam ratios with the three-dimensional results of other researchers as well as with the results for both strip and "ordinary" slender body theory.

The zero-speed case is also covered by P.D. Sclavounos; "The Interaction of an Incident Wave Field with a Floating Slender Body at Zero Speed" (1981). Sclavounos extends Newman's unified slender body theory to solve the diffraction potential as well as the heave and pitch conditions. He provides results for the vertical hydrodynamic force distribution and the heave and pitch added mass and damping coefficients for a Series 60 hull. The exciting forces and moments are also calculated using both the diffraction potential (to obtain the pressure on the hull) and Haskind's relations. Haskind's relations agree well with the pressure force integration around the hull surface.

Many papers relating to potential flow theory were also reviewed. Newman has published many articles leading up to the development of unified slender body theory. Other papers of interest included those by Salvessen et al (1970) and Sclavounos.

1.2.3 General Work

Yamaguchi (1985) discusses the installation of the Articouple system on pusher tug-barges in Japan. This system allows relative pitch between the tug and barge and at

the time of the article had been in use for twelve years with great success. The couplers for the tug-barges have been built in two forms: one for harbour work with a design wave height of 3 to 3.5 metres and one for open ocean work with a design wave height of 7.5 metres. Yamaguchi also includes a summary of the load analysis formulae.

Many books are available on the history of tugs; Brady (1967) provides a very general history including the development of the early pusher tugs. A general history of large tug/barge systems is provided by C. Wright (1973). He includes a list of ocean going unmanned tug/barge units. The International Tug Conventions yielded several related articles on pusher tug systems. Dr. H. H. Heuser (1970, 1976,1982) covers push-towing on German inland waterways, while L. R. Glosten (1967, 1972) details his SEA-LINK design. Boutan and Colin (1979) discuss coastal and ocean-going tug/barges; Stockdale (1970, 1972) examines hinged and articulated ships and Teasdale (1976) examines a probabilistic approach to designing a push-tow linkage.

Other sources of general information on push-tow systems included the National Ocean-Going Tug-Barge Planning Conference (1979) which provided both a summary of linkage systems for pusher tugs and a list of related articles on push-towing. Several other articles are also listed in the bibliography.

Chapter 2

Theoretical Derivation

2.1 General

Potential flow theory has been used for many years to describe the motions and loads on slender bodies such as ships. The theoretical work in this section builds on previous work by extending Newman's unified slender body theory for a ship at zero forward speed to a hinged ship (the tug-barge system). The objective is to produce an efficient and accurate method for predicting the vertical forces on the coupling between tug and barge. These forces are dependent on three motions; the heave, pitch and roll. Heave and pitch are the primary motions and are easily modeled using potential flow. It is anticipated that in heavy seas the tug-barge system will be stationary and hence the assumption of zero speed is acceptable. Implicit in this assumption is that the maximum forces will occur in heavy seas.

The hull motions can be solved by applying a set of differential equations to define the motion of the vessel. In the case of the coupled tug-barge the heave and pitch motions of each vessel are combined to define the relative pitch between the tug and barge. Initially the two-dimensional heave solution for each section is found; in unified slender body theory this forms the inner solution. The three-dimensional solution for a slender body is then found thus defining the outer solution. A matching region is developed between the inner and outer solutions using Struve and Bessel functions. The hydrodynamic pressure forces and moments are calculated from the three-dimensional flow solution while the hydrostatic forces and moments are derived from the hull

profiles. Balancing the forces and moments on each hull gives the vertical shear force and moment about the hinge. By constraining the motion of the tug and barge to be equal at this point the pin force can be calculated.

The following sections summarize the theoretical derivation of unified slender body theory as described by Newman (1978), Newman & Sclavounos (1980), Mays (1978) and Sclavounos (1981).

2.2 Unified Slender Body Theory

Physically unified slender body theory (or unified theory) solves the radiation problem by matching the solution for the inner region with the solution for the outer region. In the inner region the longitudinal flow gradients are much smaller than the transverse flow gradients and the solution can be reduced to the two-dimensional (strip theory) solution. This solution meets all the boundary conditions except the radiation condition and is valid for transverse distances small compared with the ship length. The solution in the outer region is valid for distances large compared with the beam where the flow gradients are of comparable magnitude in all directions. This solution meets all the boundary conditions except for the hull boundary condition. By combining the far-field expansion of the inner (strip) problem with the inner expansion of the outer problem in this matching region a complete solution can be found that is accurate at all wavelengths. This full solution can be described as the two-dimensional solution combined with an interaction coefficient.

Newman (1978) and Newman and Sclavounos (1980) both solve the radiation problem with the latter article supplying comparisons to experimental results, ordinary

slender body theory and strip theory. Sclavounos (1981) extended this work to the diffraction problem. Results have shown the unified theory to be accurate for slender hulls (Series 60 hulls and prolate spheroids).

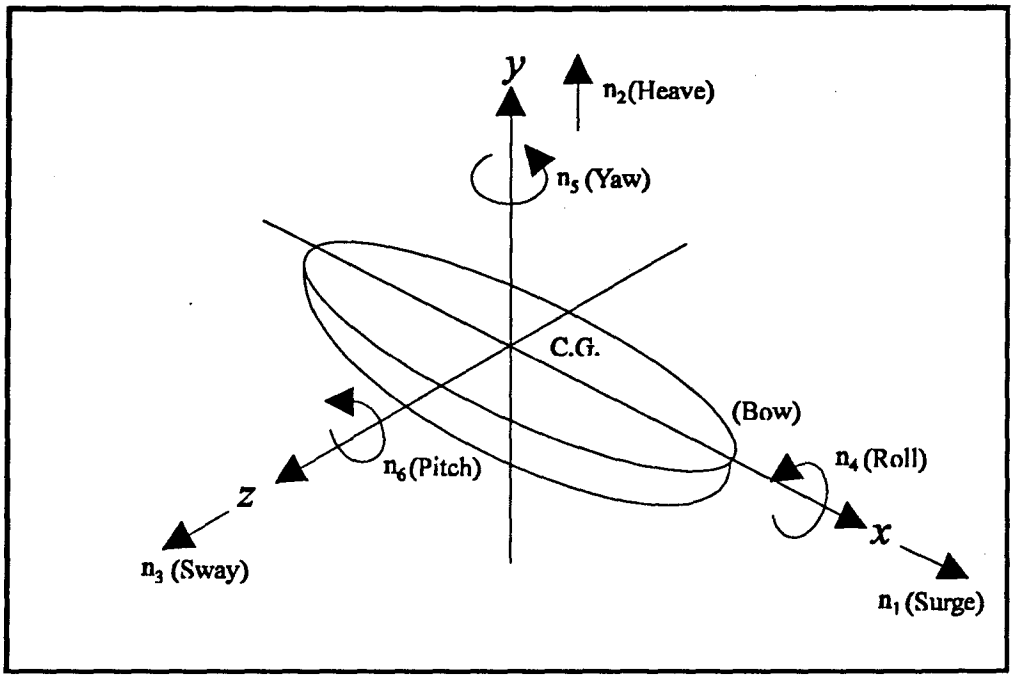

Figure 2.1 : Coordinate System and six modes of motion

2.2.1 Boundary Conditions

The model orientation within a Cartesian coordinate system is shown in Figure 2.1. The free surface in the undisturbed condition is taken at $y = 0$ and the hull is assumed to be symmetric about the centre-plane at $z = 0$. The following assumptions are made:

1. Small harmonic motions allow the theory to be linearized. i.e.

$$\Phi(x,y,z;t) = \phi(x,y,z)e^{-i\omega t} \tag{2.1}$$

2. Viscous effects are ignored.
3. Flow is assumed to be incompressible and irrotational.
4. Each mode is independent of the other modes such that

$$\phi = \sum_{i=-1}^{n} \phi_i \tag{2.2}$$

These independent potentials are defined as :

ϕ_0 Potential due to incident waves (i.e. no ship present)

ϕ_1 Radiation potential associated with motion in surge (in calm water)

ϕ_2 Radiation potential associated with motion in heave

...

ϕ_6 Radiation potential associated with motion in pitch

ϕ_{-1} Diffracted potential (Newman uses ϕ_7)

The deep water incident wave potential is given by

$$\phi_0 = \frac{igA}{\omega} e^{ky - ik(x\cos\theta + z\sin\theta)} \tag{2.3}$$

where A is the wave amplitude and θ is the angle of incidence. θ is measured from the x-axis with $\theta = 180°$ representing the head sea condition.

The radiated potentials are used to solve for the motion in the respective modes while the diffracted potential does not need to be solved. Sclavounos (1981) provides a solution for this potential.

The fluid boundaries can be derived from the original assumptions.

1. The three-dimensional Laplace equation defines the fluid motion:

$$\nabla^2\Phi = \frac{\partial^2\Phi}{\partial x^2} + \frac{\partial^2\Phi}{\partial y^2} + \frac{\partial^2\Phi}{\partial z^2} = 0 \qquad (2.4)$$

2. The free surface condition can be reduced from Bernoulli's equation to yield:

$$-\omega^2\phi + g\frac{\partial\phi}{\partial z} = 0 \qquad (\text{on } y = 0) \qquad (2.5)$$

This equation can be rewritten as:

$$k\phi - \frac{\partial\phi}{\partial z} = 0 \qquad (2.6)$$

$$\text{where: } k = \frac{\omega^2}{g} \qquad (2.7)$$

k is the wave number (or deep-water dispersion relationship). The wavelength is λ where:

$$\lambda = \frac{2\pi}{k} \qquad (2.8)$$

3. The velocity of the incident and diffracted waves is equal and opposite on the surface of the body.

$$(\phi_{0,j} + \phi_{-1,j})n_j = 0 \qquad (2.9)$$

4. The body boundary condition is defined as

$$\phi_{,j}\, n_j = n_j\dot{r}_j = i\omega n_j r_j \qquad (2.10)$$

where n_j is the normal vector pointing out of the fluid domain and r_j is the motion in mode j.

5. The above boundary conditions require that the velocity potentials ϕ_j represent outgoing waves far from the body with the fluid velocities ($\nabla\Phi$) vanishing as $y \to -\infty$. The radiation condition takes the form

$$\phi \propto \frac{1}{\sqrt{r}} e^{-ikr} \text{ as } r \to \infty \tag{2.11}$$

2.2.2 Two-Dimensional Solution

The assumptions and boundary conditions (other than the radiation condition) remain valid for the two-dimensional solution when the longitudinal flow effects are ignored. By reducing $\phi(x,y,z)$ to $\phi(y,z)$ the local hull cross-section can represent the boundary surface in the inner region of flow (close to the body). The inner region can be defined as transverse distances small compared to the ship length.

The two-dimensional potential solution should yield a potential ϕ_j for each mode. Since only heave (j=2) and pitch (j=6) are being considered and ϕ_6 can be represented by $\phi_6 = x\phi_2$ in the three-dimensional solution only the potential for ϕ_2 needs to be calculated. This potential will be described as ϕ_{2D}. The following section describes a method of determining ϕ_{2D}; the numerical solution is contained in Appendix A.

2.2.2.1 Solution for Two-Dimensional Potential

The potential ϕ_{2D} can be described as the integration of a line of two-dimensional pulsating sources located on the hull surface. Figure 2.2 represents the two-dimensional hull segment in the y-z plane with sources on half the hull. The source potentials are solved using mirror terms above the free surface to create the correct boundary condition.

The potential of the source terms ϕ_S is

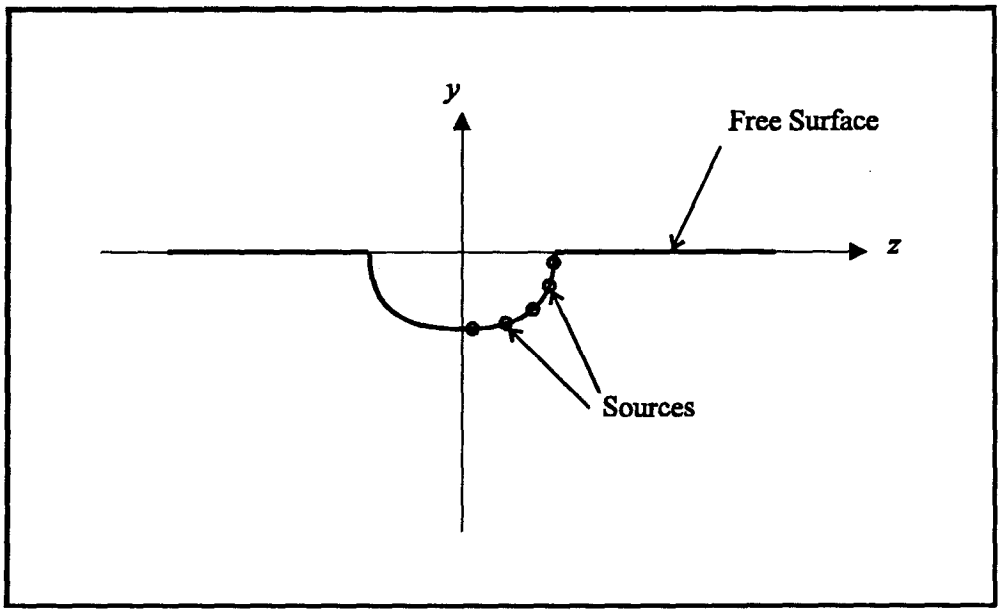

Figure 2.2 Two-Dimensional Section

$$\phi_S = \frac{1}{2}\ln\left(\frac{(z-\xi)^2+(y-\eta)^2}{(z-\xi)^2+(y+\eta-2y_f)^2}\right)+2\pi i e^{k(y+\eta-2y_f)-ik|z-\xi|}$$
$$+2\int_{-\infty}^{0}\frac{p\cos(p(y+\eta-2y_f))+k\sin(p(y+\eta-2y_f))}{p^2+k^2}e^{p|z-\xi|}dp \qquad (2.11)$$

This represents a direct source term, a propagating wave term and an integral over the free surface respectively. The derivation of ϕ_S is in Appendix A.

To obtain ϕ_j for the full hull ϕ_S must be integrated around the hull section using the source strength distribution $A_j(c)$. The parameter c refers to the arc length around the hull section as defined in Appendix A.

$$\phi_j(y,z) = \int_C A_j(c)\phi_S(y,z,\eta(c),\xi(c))dc \qquad (2.12)$$

The numerical solution for the $A_j(c)$ is described in Appendix A.

The outer expansion of the two-dimensional solution yields

$$\phi_j(y,z) \cong \tfrac{1}{2} i\sigma_j e^{ky-ik|z|} \tag{2.13}$$

where σ_j is the two-dimensional source strength. The source strength is related to the far-field wave amplitude; the solution is presented in Appendix A.

2.2.3 Three-Dimensional Solution

Slender body theory is used to provide an outer solution for the body while an inner solution is derived from the strip theory results above. The outer solution meets all the boundary conditions except for the hull itself. The asymptotic behaviour of the inner solution in the far field and the outer solution close to the ship can be used to find a unique solution by requiring that the two solutions be compatible in a suitably defined overlap region. Figure 2.3 illustrates the inner, outer and matching regions for the complete solution.

2.2.3.1 Outer Region

The outer region is the area far from the hull (at radial distances greater than the beam) where the flow can be considered independently of the hull geometry details. In this region the velocity potential can be approximated by a line distribution of three-dimensional sources along the centre-line of the ship.

This line distribution can be described by :

$$\varphi_j = \int_L q_j(\xi) G(x-\xi, y, z)\, d\xi \tag{2.14}$$

where φ_j is the three-dimensional potential.

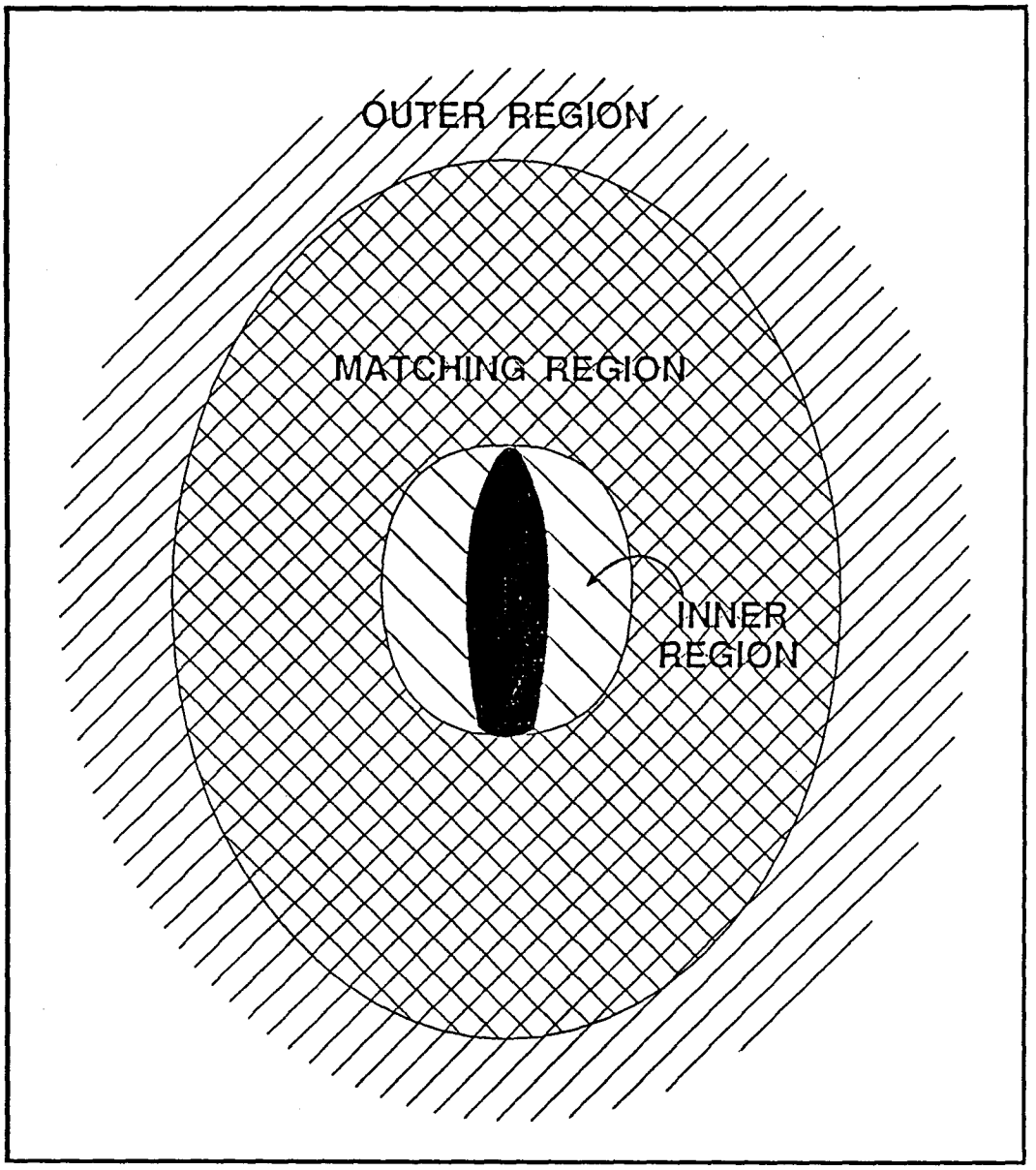

Figure 2.3 Regions of Validity

Here q_j is the source strength distribution and G is the velocity potential of a "translating-pulsating" source on the x-axis at the point ξ. In order to match the outer expansion of the inner solution equation (2.14) must be expanded for small kr, where $r = \sqrt{y^2 + z^2}$. Newman and Sclavounos (1980 : equations 15 to 19) use a Fourier

transform on both sides of this equation to solve the inner expansion of the outer solution for the source strengths. By taking the inverse transform of this equation a linear operator $L(q_j)$ is obtained such that :

$$L(q_j) = [\gamma + \pi i] q_j(x) + \tfrac{1}{2} \int_L \operatorname{sgn}(x-\xi) \ln(2k|x-\xi|) \frac{d}{d\xi} q_j(\xi) d\xi$$
$$- \frac{\pi}{4} k \int_L \left[Y_0(k|x-\xi|) + H_0(k|x-\xi|) + 2i J_0(k|x-\xi|) \right] q_j(\xi) d\xi \qquad (2.15)$$

This corresponds to equation (2.13) in Sclavounos (1981) and can also be derived from Newman and Sclavounos (1980 : equation 43). The inner expansion of the outer solution transforms to :

$$\varphi_j(x,y,z) = q_j(x) R_{2D} - \frac{1}{2\pi}(1+kz) L(q_j) \qquad (2.16)$$

in the physical x-space. R_{2D} is the two-dimensional source potential for the outgoing far-field waves.

2.2.3.2 Inner Region

In the inner region the two-dimensional Laplace equation (2.4), the free-surface equation (2.5) and the body boundary condition (2.10) must all hold for φ_j. The general solution of these conditions can be obtained in the form

$$\varphi_j = \phi_{jP} + C_j(x) \phi_{jH} \qquad (2.17)$$

where ϕ_{jP} is the particular solution and ϕ_j is the homogeneous solution. The coefficient $C_j(x)$ is an "interaction" coefficient which will be solved by matching with the outer solution.

Newman (1978) shows that the homogeneous solution is of the form $\phi_j + \overline{\phi_j}$ where $\overline{\phi_j}$ is the complex conjugate of ϕ_j.

$$\varphi_j = \phi_j + C_j(x)\left(\phi_j + \overline{\phi_j}\right) \tag{2.18}$$

In the overlap region where y and z are larger than the beam of the hull but less than the hull length the potentials can be written in terms of their effective source strengths :

$$\phi_j = \sigma_j R_{2D}(y,z) \tag{2.19}$$

Combining equations (2.18) and (2.19) gives

$$\varphi_j = \left\{\sigma_j + C_j(x)\left(\sigma_j + \overline{\sigma_j}\right)\right\}R_{2D} - 2iC_j(x)\overline{\sigma_j}\,\mathrm{Im}(R_{2D}) \tag{2.20}$$

By setting $\mathrm{Im}(R_{2D}) = \frac{1}{2}(1+kz)$ in the overlap region (at small kr) the outer expansion of the inner solution is

$$\varphi_j = \left\{\sigma_j + C_j(x)\left(\sigma_j + \overline{\sigma_j}\right)\right\}R_{2D} - iC_j(x)\overline{\sigma_j}(1+kz) \tag{2.21}$$

Matching the inner expansion of the outer solution (2.14) and the outer expansion of the inner solution above gives

$$q_j = \left\{\sigma_j + C_j(x)\left(\sigma_j + \overline{\sigma_j}\right)\right\}R_{2D} \tag{2.22}$$

$$\frac{1}{2\pi}L(q_j) = iC_j(x)\overline{\sigma_j} \tag{2.23}$$

The outer source strength q_j can be determined by eliminating $C_j(x)$ and solving the following equation

$$q_j(x) - \left(\frac{\sigma_j + \overline{\sigma_j}}{2\pi i\overline{\sigma_j}}\right)L(q_j) = \sigma_j \tag{2.24}$$

The matching function $C_j(x)$ is determined from

$$C_j(x) = \frac{q_j - \sigma_j}{\sigma_j + \sigma_j} \tag{2.25}$$

2.2.4 Hydrodynamic Terms

The hydrodynamic force is found by integrating the hydrodynamic pressure around the surface of the hull. The pressure can be found from the total potential flow around the hull. This consists of the motion terms (j=2, 6 for heave and pitch) which define the added mass and damping and the incident and diffracted wave pressures which define the excitation force.

2.2.4.1 Added Mass and Damping

The three dimensional added mass and damping is calculated by integrating the three-dimensional potential in equation (2.18) around the hull surface. This equates to integrating the pressure on the hull surface for a ship experiencing steady-state small amplitude heave and pitch motions in a calm sea. The full hydrodynamic term can be written as:

$$-\omega^2 m_{ij} + i\omega c_{ij} = -i\omega\rho \iint_S n_i n_j \phi_{2D} + n_i n_j C_j(x)\left(\phi_{2D} + \overline{\phi_{2D}}\right) dS \tag{2.26}$$

where the potential $\phi_j = n_j \phi_{2D}$. The first integral equates to the two-dimensional added mass and damping and can be written

$$-\omega^2 m_{ij}^{2D} + i\omega c_{ij}^{2D} = -i\omega\rho \int_c n_i n_j \phi_{2D}\, dc \tag{2.27}$$

Therefore equation (2.28) reduces to

$$-\omega^2 m_{ij} + i\omega c_{ij} = \int_L n_i n_j \left(-\omega^2 m_{22}^{2D} + i\omega c_{22}^{2D}\right) + n_i C_j(x) n_j \left(2i\omega c_{22}^{2D}\right) dx \tag{2.28}$$

where equation (2.25) can be written as

$$C_j = \frac{\frac{q_j}{n_j} - \sigma_{2D}}{\sigma_{2D} + \overline{\sigma_{2D}}} \tag{2.29}$$

Equation (2.26) can then be simplified to

$$-\omega^2 m_{ij} + i\omega c_{ij} = \int_L n_i n_j \left(-\omega^2 m_{22}^{2D} + i\omega c_{22}^{2D}\right) + n_i \frac{q_j - n_j \sigma_{2D}}{\sigma_{2D} + \overline{\sigma_{2D}}} \left(2i\omega c_{22}^{2D}\right) dx \tag{2.30}$$

2.2.4.2 Excitation Force

The excitation force is the hydrodynamic force caused by the interaction of the hull with the incident and diffracted waves. This force can be expressed as

$$F_j = AX_j \tag{2.31}$$

where A is the amplitude of the incident wave and

$$X_j = -i\omega\rho \iint_S n_j (\phi_0 + \phi_{-1}) dS \tag{2.32}$$

This equation requires the evaluation of the diffracted potential which Sclavounos (1981) solves. Alternately it can be simplified by using the Haskind relations (reciprocity between the far-field waves and the excitation force). By using the body-boundary condition $\frac{\partial \phi_j}{\partial n} = i\omega n_j$ and applying Green's theorem equation (2.32) can be reduced to:

$$X_j = \rho \iint_S \left(i\omega n_j \phi_0 - \varphi_j \frac{\partial \phi_0}{\partial n} \right) dS \tag{2.33}$$

Including the matching terms the excitation force can be written as:

$$X_j = \rho \iint_S \left(i\omega n_j \phi_0 - \phi_j \frac{\partial \phi_0}{\partial n} \right) dS - \rho \iint_S C_j(x)(\phi_j + \overline{\phi_j}) \frac{\partial \phi_0}{\partial n} dS \qquad (2.34)$$

Sclavounos (1981) shows that this method of evaluating the excitation force produces results very similar to those found after evaluating the diffracted potential.

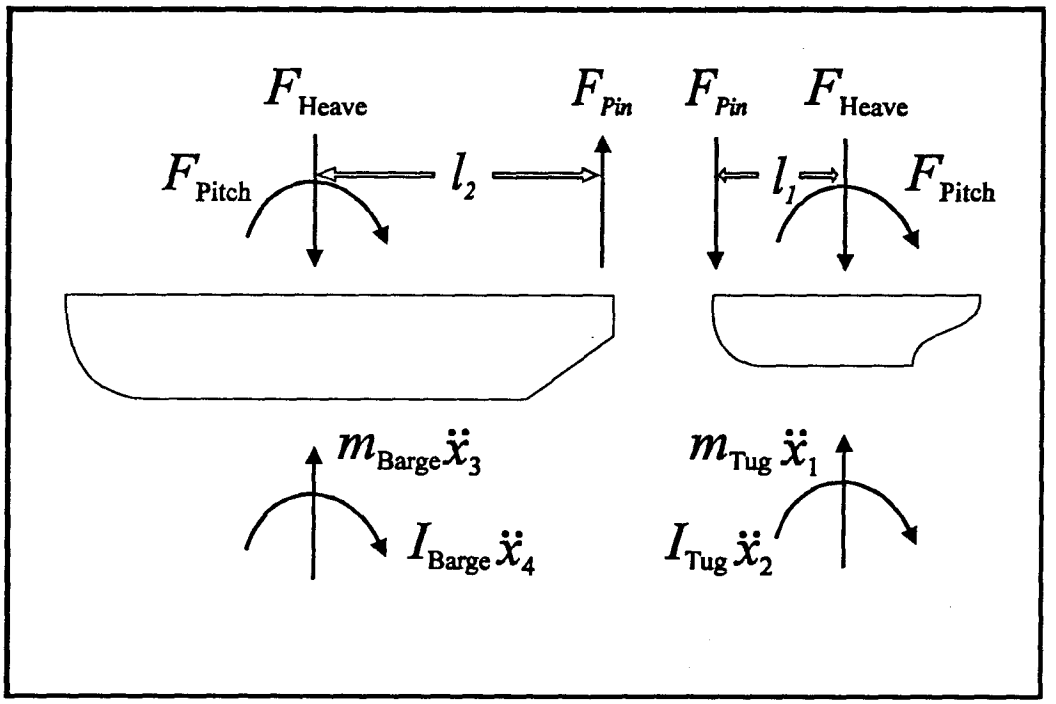

Figure 2.4: Force Diagram for Coupled Tug/Barge

2.3 Determination of Coupling Force

The coupling force on the hinge between the tug and barge is determined by summing the forces on each hull and then constraining the motions of each vessel to be equal at the hinge. Figure 2.4 represents the forces on the coupled tug-barge unit. The lengths l_1 and l_2 are the distances from the centres of gravity of the tug and barge

respectively to the pivot point. The motions of the two hulls are described by the vector $\{x\}$ where i=1 is the tug heave, i=2 is the tug pitch, i=3 is the barge heave and i=4 is the barge pitch.

The force associated with each motion can be calculated by starting from the standard assumption that:

$$[M]\{\ddot{x}\}+[C]\{\dot{x}\}+[K]\{x\}=\{F\} \tag{2.35}$$

The damping $[C]$ and stiffness $[K]$ matrices reduce to 0 for rigid body modes and the force $\{F\}$ can be split into the pressure integration around the hulls and a vector of the pin forces and moments. Equation (2.35) thus reduces to:

$$[M]\{\ddot{x}\}=\left\{\int_S pn_j\,dS\right\}+\{B\}F_{\text{Pin}} \tag{2.36}$$

where:

$[M]$ for the four modes required can be written as:

$$[M]=\begin{bmatrix} m_{\text{tug}} & 0 & 0 & 0 \\ 0 & \int_{V_{\text{tug}}}\rho(x^2+y^2)\,dV & 0 & 0 \\ 0 & 0 & m_{\text{barge}} & 0 \\ 0 & 0 & 0 & \int_{V_{\text{barge}}}\rho(x^2+y^2)\,dV \end{bmatrix} \tag{2.37}$$

and

$$\{B\} = \begin{Bmatrix} -1 \\ -l_1 \\ 1 \\ -l_2 \end{Bmatrix} \tag{2.38}$$

The mass matrix is composed of the mass and moment of inertia for each hull while the $\{B\}$ vector represents the direction and moment arm of the force at the pivot location. The pressure integration term can be further reduced to

$$\left\{\int_S p n_j \, dS\right\} = \left\{-\int_S \rho\left(g(y - y_{fs}) + \frac{\partial \phi}{\partial t}\right) n_j \, dS\right\} \tag{2.39}$$

The gravity term in this equation represents the hydrostatic force on the hull while the $\frac{\partial \phi}{\partial t}$ term gives the hydrodynamic forces. Substituting the hydrodynamic forces described in sections 2.1.4.1 and 2.1.4.2 into equation (2.39) yields

$$\left\{\int_S p n_j \, dS\right\} = -\left\{\int_S \rho g(y - y_{fs}) n_j \, dS\right\} - \left[-\omega^2 m_{ij} + i\omega c_{ij}\right]\{x\} - \left\{-i\omega\rho \int_S (\phi_0 + \phi_{-1}) n_j \, dS\right\} \tag{2.40a}$$

or:

$$\left\{\int_S p n_j \, dS\right\} = -[\mathrm{HS}]\{x\} - [\mathrm{HD}]\{x\} - \{\mathrm{F}\} \tag{2.40b}$$

The coupling between the tug and barge means that the vertical motion of the barge stern is equal to the vertical motion of the tug bow. This provides a constraint on the vector $\{x\}$ which can be used to solve for F_{Pin} and the hull motions.

$$x_1 + x_2 l_1 = x_3 - x_4 l_2 \tag{2.41a}$$

or:

$$\{B\}^T \begin{Bmatrix} x_1 \\ x_2 \\ x_3 \\ x_4 \end{Bmatrix} = 0 \tag{2.41b}$$

For harmonic motion the $\{\ddot{x}\}$ term can be written as $-\omega^2\{x\}$ and equation (2.36) can be written as:

$$\left(-\omega^2[M]+[\text{HD}]+[\text{HS}]\right)\{x\} = \{\text{-F}\}+\{B\}F_{\text{Pin}} \tag{2.42}$$

$$\{x\} = \left(-\omega^2[M]+[\text{HD}]+[\text{HS}]\right)^{-1}\left\{\{\text{-F}\}+\{B\}F_{\text{Pin}}\right\} \tag{2.43}$$

Pre-multiplying by $\{B\}^T$:

$$\{B\}^T\left(-\omega^2[M]+[\text{HD}]+[\text{HS}]\right)^{-1}\left\{\{\text{-F}\}+\{B\}F_{\text{Pin}}\right\} = 0 \tag{2.44}$$

This can be solved for the force F_{Pin} at the pivot such that

$$F_{\text{Pin}} = \frac{\{B\}^T\left(-\omega^2[M]+[\text{HD}]+[\text{HS}]\right)^{-1}\{\text{F}\}}{\{B\}^T\left(-\omega^2[M]+[\text{HD}]+[\text{HS}]\right)^{-1}\{B\}} \tag{2.45}$$

The application of the constraint differs from the method used by Robinson (1976) to obtain the shear force. Robinson assumed that the hulls did not affect each other except for the connecting pin. He solved the heave and pitch for each unconnected hull and then repeated this computation for a unit force oscillating each unconnected hull at the pin location. The pin force and hull motions were found by equating the motion and force at the pin location.

Chapter 3

Experimental Work

3.1 General

The model testing was carried out in the towing tank at the Ocean Engineering Centre of B.C. Research. The experiments were performed in head and following seas with two different pivot locations in regular sinusoidal waves. The only previous work found on pusher tug and barge units was by Rossignol (1974, 1975a) and Robinson (1977); a brief summary is included in Chapter 1. This work was performed on purpose-built models moving at different velocities. Although part of the report was missing no results for the zero speed case were found.

3.2 Experimental Objectives

1. To find the loads on the coupling of the tug-barge model,
2. to find the motions of the barge and relative motions of the tug,
3. to investigate the effect on the pin forces of moving the coupling location,
4. to examine the effect of head and following seas on the tug-barge model, and
5. to provide a comparison for the results of the numerical simulation.

3.3 Experimental Apparatus

1. Tug-barge model coupled together
2. Four Omega load cells - effective range 0 - 200 lb. force,
3. Three potentiometers - barge heave and trim and pivoting of the tug,
4. Capacitance wave probe,
5. ST41B signal conditioner,
6. Two DT 2801 data acquisition systems (8 Channel),
7. Data acquisition program (ASYSTANT PLUS),
8. Two IBM-compatible Computers,
9. Wave maker with a regular wave generator,
10. Towing tank : Width = 12 feet, Depth = 8 feet

3.4 Model Set-Up

The tug and barge models were generously lent by Robert Allan Ltd., a Vancouver naval architecture firm. The lines plans for each model are shown in Figures 3.1 and 3.2. The waterline length of the barge model is 2.70 metres while the tug is 0.91 metres in length. The total length when coupled is 3.35 metres. The barge beam measures 0.64 metres giving a length to beam ratio of 5.234 for the coupled system. Although a higher ratio would be preferable no other models were available.

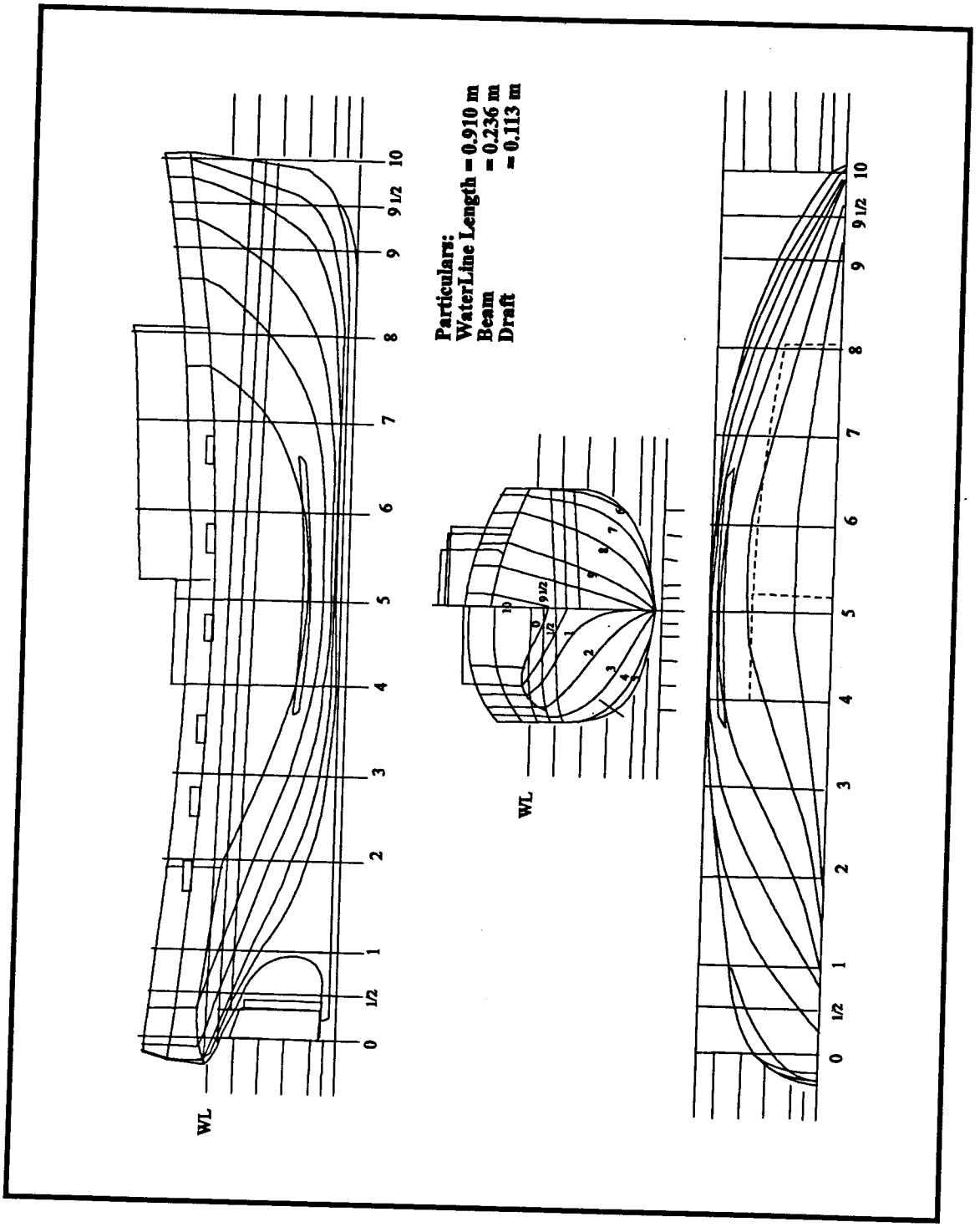

Figure 3.1 : Tug Lines

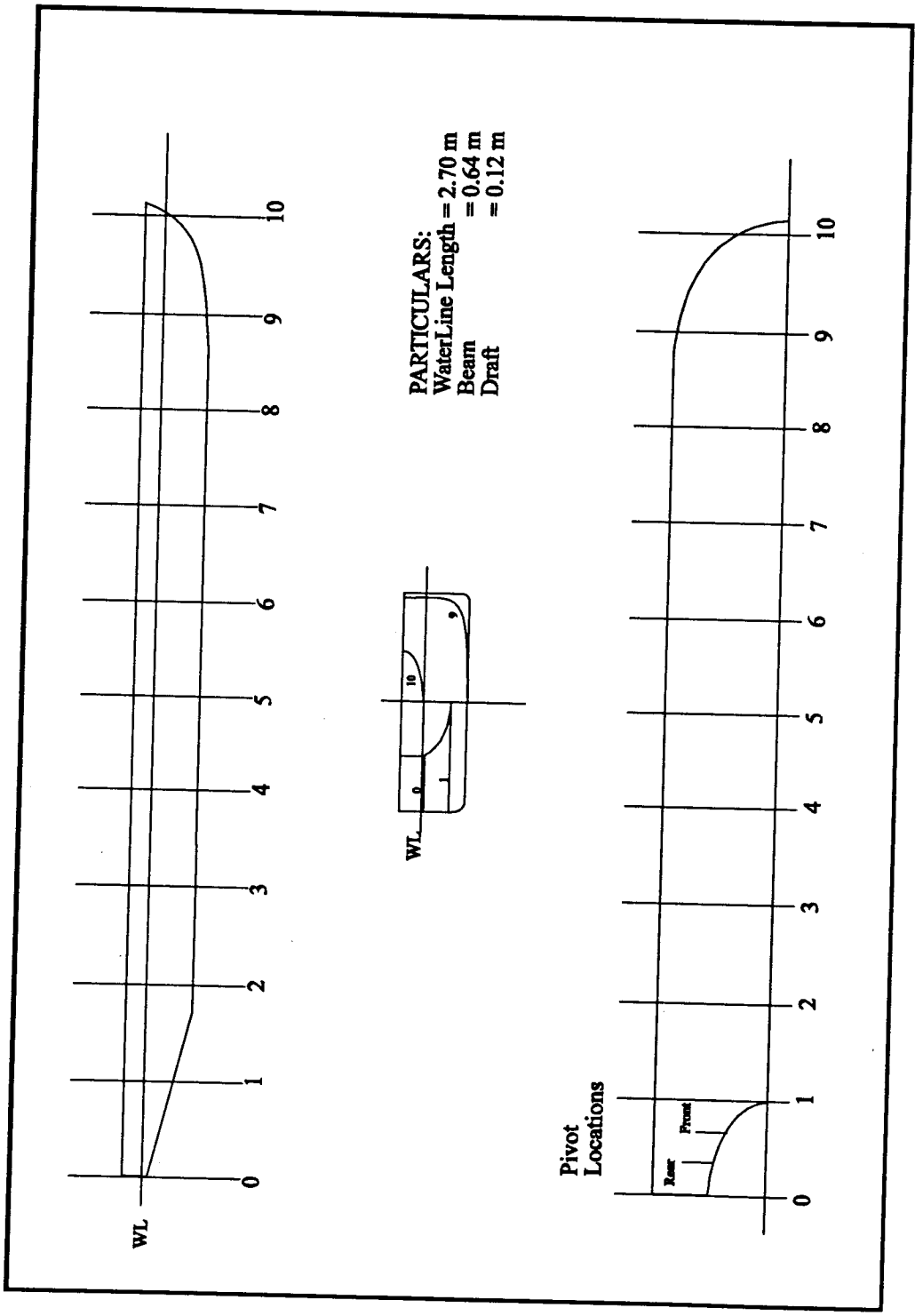

Figure 3.2 : Barge Lines

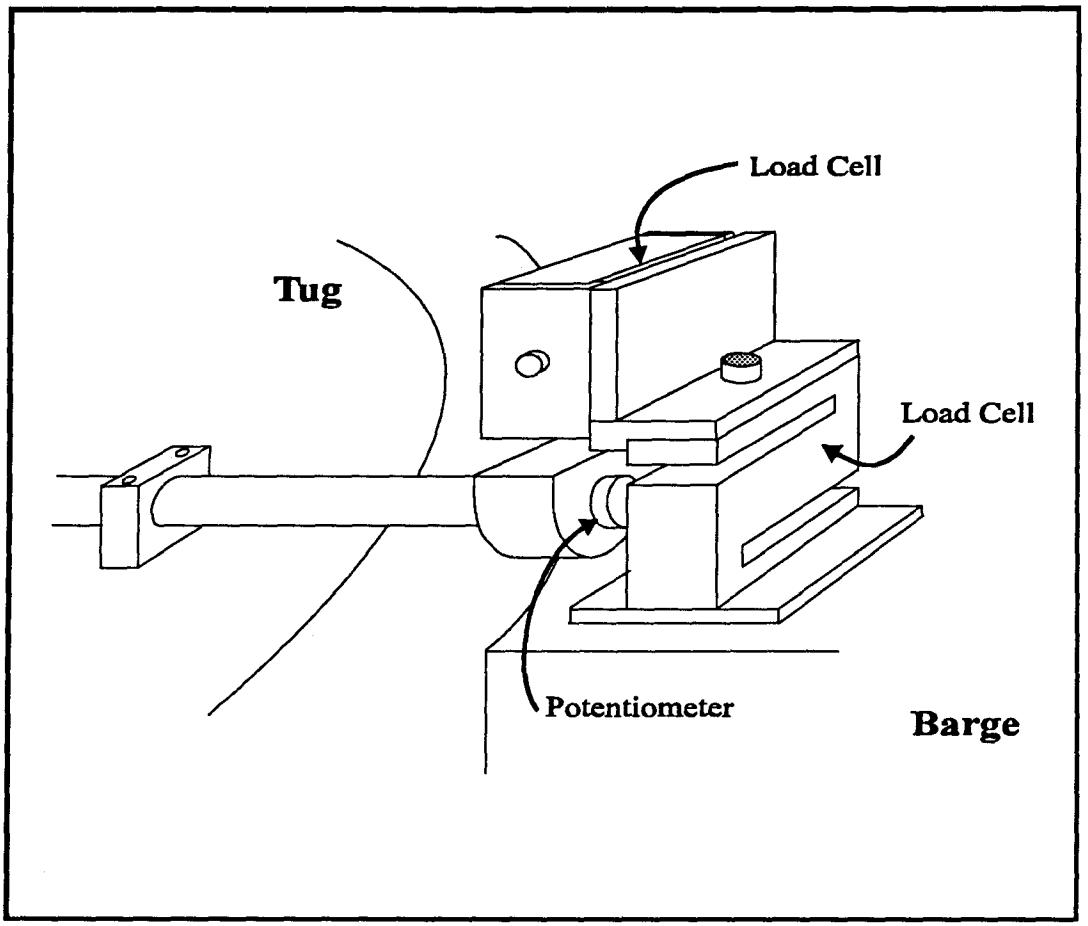

Figure 3.3 Bearing Design

A bearing system was designed (Figure 3.3) to join the tug and barge. This system consisted of a shaft with a bearing at each end. The shaft was attached to the tug by two brackets and locked in place using set screws. A horizontal and a vertical load cell were mounted to the bearing at each end and these were attached to the barge. A potentiometer was inset into the starboard side of the shaft to measure the relative pivoting of the tug.

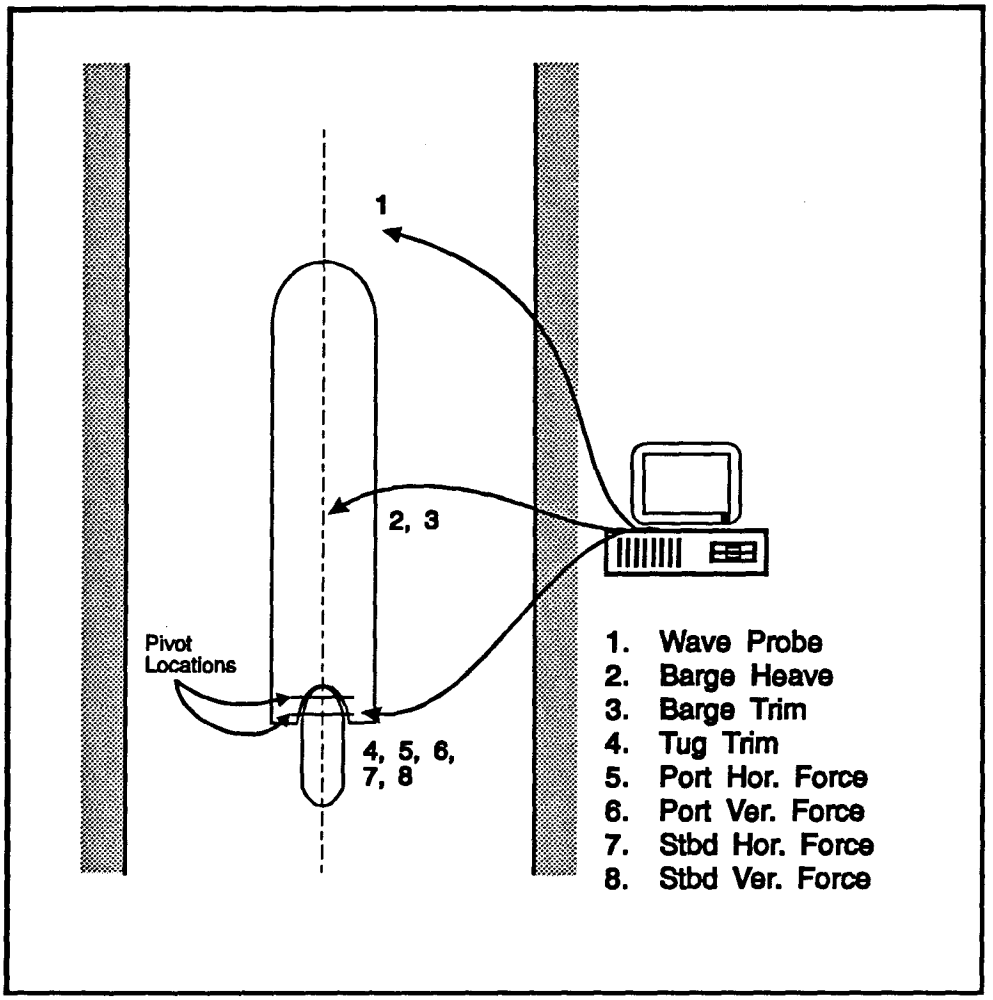

Figure 3.4 Tow Tank Set Up

The remaining instrumentation consisted of the wave probe and the heave and pitch potentiometers for the barge. The latter two were attached at the centre of the barge on the heave post. The wave probe was set in the water ahead and to one side of the model to avoid reflection off the bow. Figure 3.4 is a schematic of the tow tank set up.

3.5 Procedure

1. The barge and tug models were individually weighted and balanced.
2. The load cells, potentiometers and the wave probe were all calibrated individually.
3. The fully ballasted tug and barge models were set up in the tow tank. The gap between the shaft on the barge and the foredeck of the tug was measured in calm water conditions. Wood blocks were then cut to match this gap and the shaft was fixed to the tug.
4. The tug-barge unit was positioned midway up the towing tank and a sinusoidal series of regular waves was sent down the tank by the wave maker. In order to minimize the effects of reflection data was recorded as soon as the waves became regular; 1400 points were recorded at 50 Hz for each run. The incident wave amplitude was kept as large as possible without sinking the model. The frequency range was determined from the barge length - the model was tested at wavelengths between $0.5l_{Barge}$ and $2.5l_{Barge}$. This corresponded to a range of 0.45 Hz to 1.05 Hz.
5. The model was tested in head and following seas.
6. The shaft mounting was moved forward on the tug and barge changing the pivot location by 95 mm. Approximate locations are illustrated in Figure 3.4. Steps 3 to 5 were repeated for this configuration.

3.6 Results

The final ballasted mass of the barge was 186.82 kg (including the heave post and bearing system). The tug mass was 10.68 kg. Both were ballasted to float with no trim. The procedure of section 3.4 was followed for setting up the models in the tank. A small amount of room was left around the bow of the tug and the notch to ensure that no interference would occur. The tug beam was approximately 3/4 of the width of the notch at the stern of the barge.

As described in section 3.4 two separate cases were considered; one with the pivot shaft mounted as far back as possible and one with the shaft as close to the bow of the tug as practicable. Both shaft locations are marked on the line drawings of the tug and barge in Figures 3.1 and 3.2 respectively. The distance between the shafts is 95 mm (slightly greater than 10% of the tug length).

The two hulls were connected and tested in both head and stern seas before the pivot was moved forward and the tests repeated. The width of the B.C. Research towing tank meant that certain results fell close to the natural frequencies of the tank. These were calculated as: $\omega_n = 0.653$ Hz and $\omega_n = 0.924$ Hz (Appendix C). These corresponded to wavelengths of $\lambda_n = 1.355 l_{\text{Barge}}$ and $\lambda_n = 0.677 l_{\text{Barge}}$. The effect of these frequencies was observed as an increased oscillation of the model. This effect was reduced primarily by using wooden beaches to damp the wave motion, recording results as soon as the generated waves became uniform and allowing the tank to settle between runs. Some evidence of the effect of the natural frequencies was present in the slight variations in the results.

3.6.1 Calibration

The barge heave and the wave probe were calibrated in metres, the barge pitch and the tug pivot in degrees and the load cells in Newtons. The loads were expected to be small so the load cells were calibrated from 0.49 Newtons (50 grams) up to 22.3 Newtons with the emphasis on data below 5 Newtons. The measurement of the tug pivot angle was difficult and proved to have the largest error. A regression analysis of each curve proved that all gauges were linear. A sample calibration plot is included in Appendix C.

3.6.2 Loads and Motions

Data analysis for the loads and motions consisted of examining every wave for each run. ASYSTANT PLUS, a data acquisition program used by BC Research, allows the user to examine the data within the program or to convert the files to ASCII format. The tug-barge data was converted and examined in both the time and frequency domains.

The ASCII format data was first run through a computer program which converted the data from volts to the correct units based on the calibration data. The program then determined the mean μ, the standard deviation σ and the frequencies of each wave. The mean was subtracted from each point to give a wave oscillating about zero. The mean was also checked against the results of a steady state run.

The converted data was examined in the time domain by importing each wave into a spreadsheet and plotting it. The waves were checked in detail to confirm whether they were regular sinusoids and to ensure that the program had correctly predicted the frequencies and standard deviations. Standard deviations were checked by comparing the

observed wave peaks with $\sqrt{2}\sigma$. Some reflection effects were evident at about 0.65 Hz and 0.9 Hz (close to the natural frequencies of the tank noted earlier) but the results for the motions and the vertical loads were regular sine waves in most cases. The horizontal motions produced generally poor results; the waves were primarily irregular indicating higher order harmonics. The horizontal measurement would represent the drag on the hull plus the force component of the moment due to surge between the vertical centre of gravity and the hinge point. These effects are not linear. Graphs 3.1 and 3.2 illustrate a regular and an irregular sinusoidal response respectively.

The converted data was then examined in the frequency domain by using Fast Fourier Transforms. The actual transform method was taken from "Numerical Recipes in C" and used 2^n points; n = 10 was chosen to give 1024 points.

The FFT results gave both the magnitude and the phase angle for each wave. In order to compare the tug-barge motions effectively the phase angle of the wave probe was shifted to correspond to the centre of gravity (and the centre of buoyancy) of the barge. The phase shift was determined using the following equation:

$$\gamma = \frac{x}{\lambda}$$

where $\lambda = 2\pi\frac{g}{\omega^2}$ and γ is the phase angle in radians.

As noted earlier the waves were regular sinusoids in most cases; producing a single peak in the FFT analysis. Some waves showed higher order harmonics, especially the horizontal forces. Graphs 3.3 and 3.4 illustrate a regular and an irregular FFT response respectively.

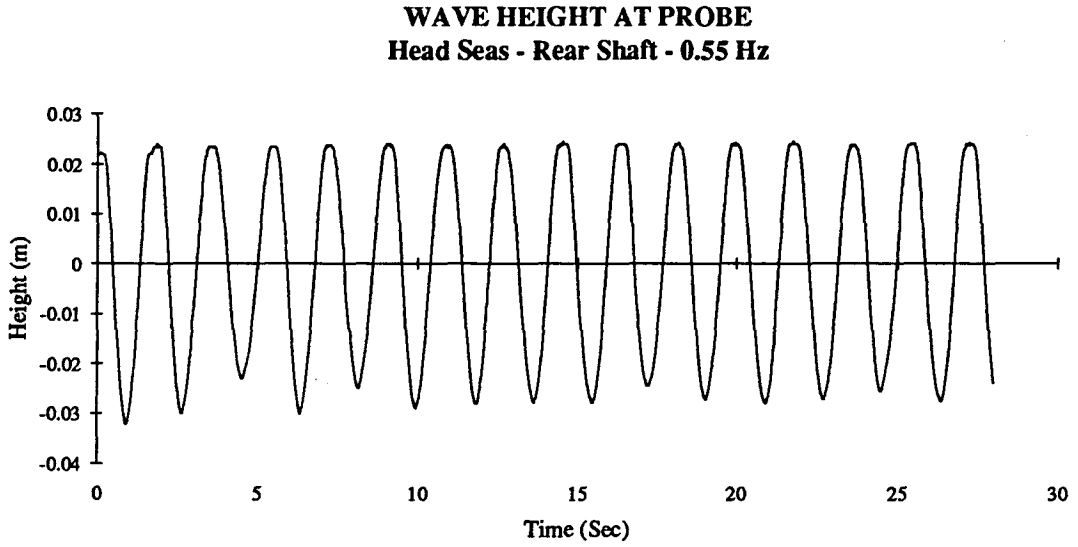

Graph 3.1 : Regular Sinusoidal Response

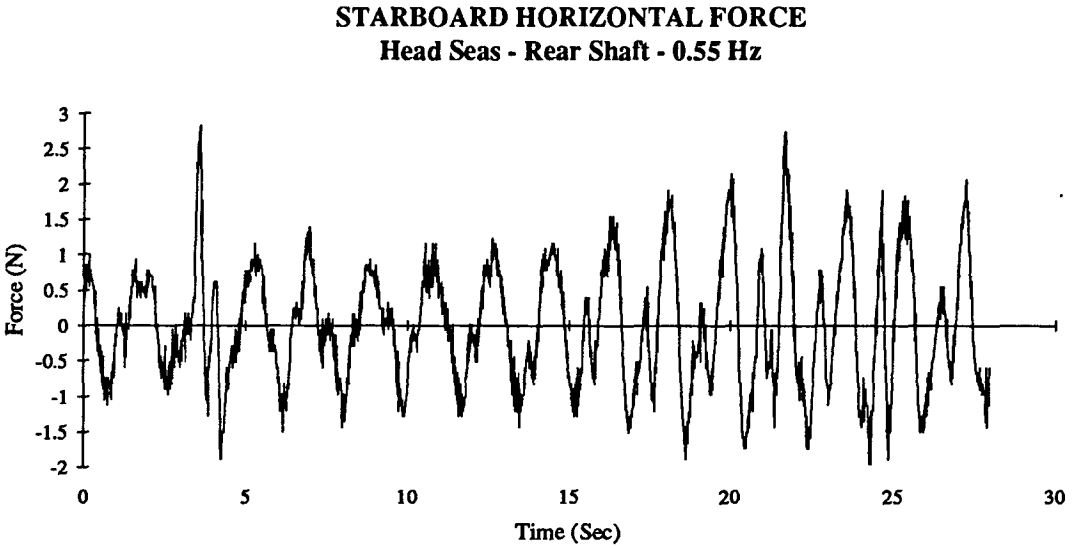

Graph 3.2 : Irregular Sinusoidal Response

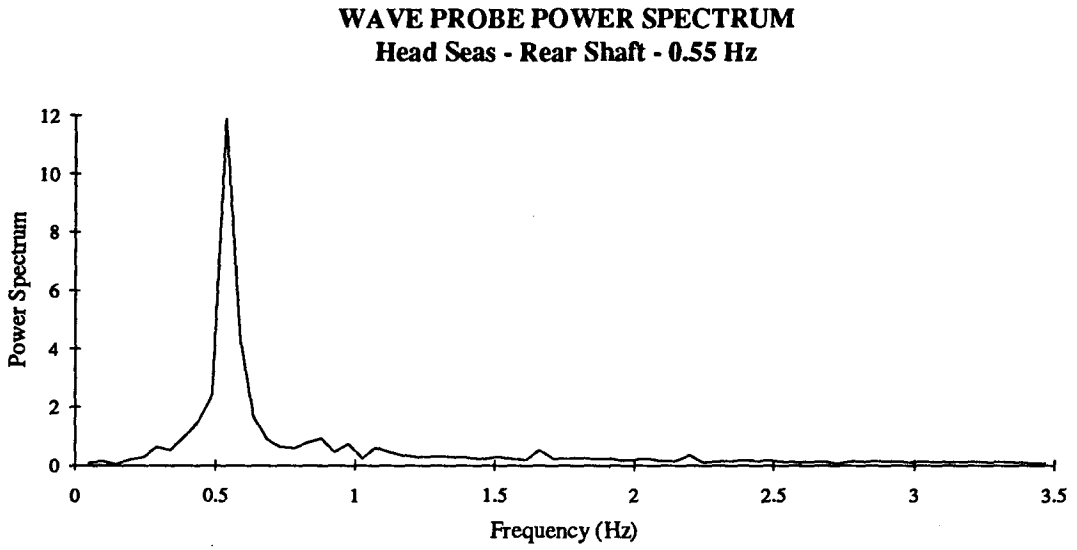

Graph 3.3 : Regular FFT Response

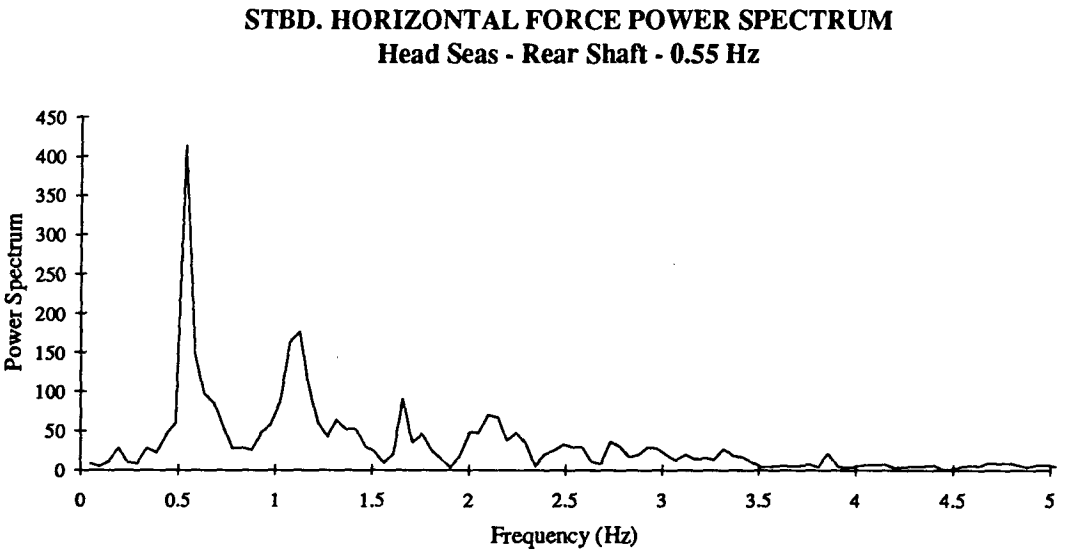

Graph 3.4 : Irregular FFT Response

A summary of the experimental results is in Appendix C. These numbers represent the amplitudes of each wave. They were determined using the results from both the time and frequency domain analyses. The wave probe results were very consistent in both amplitude and frequency; the standard deviation of the wave probe was used to find the amplitude ($\sqrt{2}\sigma$). The amplitudes of the other seven channels were determined using the following formula:

$$\frac{A_i}{A_\zeta}\zeta$$

where A_i is the area under the FFT peak of channel *i*, A_ζ is the area under the FFT from the wave probe and ζ is the amplitude of the wave probe (from the standard deviation). The phase angles of the barge heave and trim are relative to the wave probe (at the centre of gravity of the barge) while the phase angles of the pivot angle and load cells are measured at the pivot location. Each wave amplitude is non-dimensionalized using the following equations from Robinson (1977).

Barge heave: $$\frac{z_{Barge}}{\zeta_{Wave}}$$

Angular displacements: $$\frac{\theta}{360\frac{\zeta_{Wave}}{\lambda_{Wave}}}$$

Forces: $$\frac{Fl_{Barge}}{\Delta_{Barge}}\zeta_{Wave}$$

where:

z_{Barge} : Barge heave amplitude

ζ_{Wave} : Wave amplitude

θ : Angular rotation (degrees)

λ_{Wave} : Wave length

F : Force

l_{Barge} : Length of barge

Δ_{Barge} : Displacement of barge

These non-dimensionalized values are plotted for each motion and force against λ_{Wave}/l_{Barge} for each sea condition. The two pivot locations are compared on each graph with the shaft location closest to the tug bow designated the front shaft. The phase difference to the wave probe (at the centre of gravity of the barge) is also graphed.

3.6.2.1 Heave

Graphs 3.5 and 3.6 show that the magnitude of the barge heave is almost unaffected by the small change in the pivot location due to the large mass of the barge versus the tug. The results are also very similar regardless of wave direction. The barge heave at shorter wave lengths (higher frequencies) is close to the first transverse natural frequency of the tank itself ($\approx 0.7 l_{Barge}$) and the results proved less stable. The barge displacement increases with the wavelength (i.e. as frequency decreases) and the heave motion moves into phase with the wave.

The phase angles are shown in graphs 3.7 and 3.8 for each sea direction. The barge heave and the exciting wave are in phase for wavelengths above $1.5 l_{Barge}$. This corresponds to the barge rising and falling with the wave as it passes; intuitively this would require a wavelength greater than the barge length. When the wave length is approximately $0.5 l_{Barge}$ the barge heave and the exciting wave are out of phase; the barge motion is fairly steady as more than two wave peaks are under the model at this frequency. Between these wavelengths the phase angle relationship is transformed from out of phase to in phase. The effect of the natural frequency of the tank can be seen as an out of phase motion for the front shaft model at a wavelength of $1.35 l_{Barge}$. Phase results are similar for both head and stern seas.

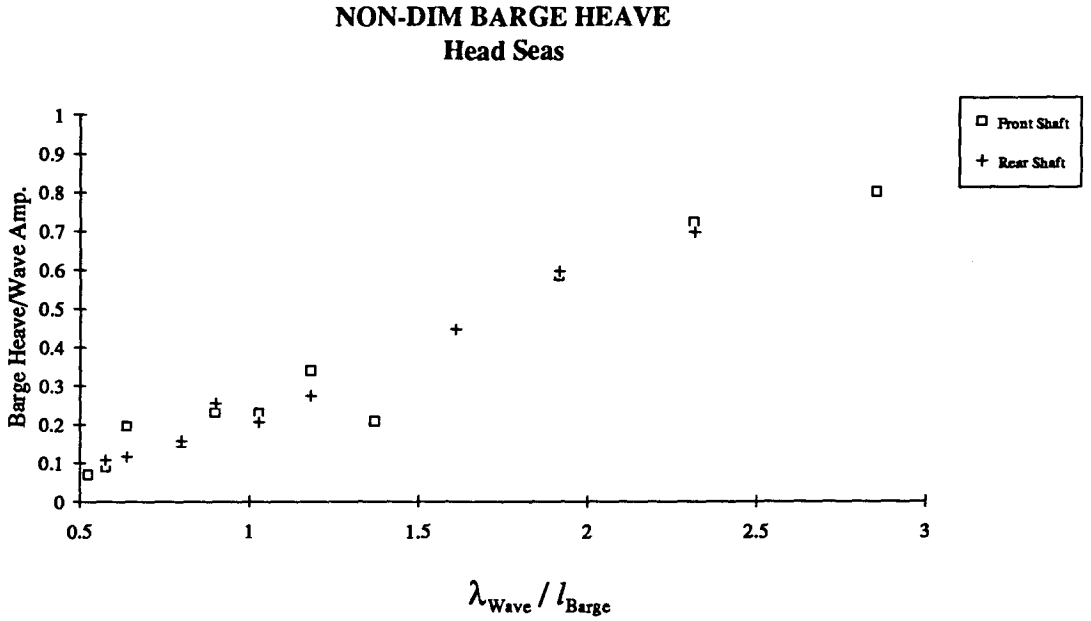

Graph 3.5 : Non-Dimensionalized Barge Heave - Head Seas

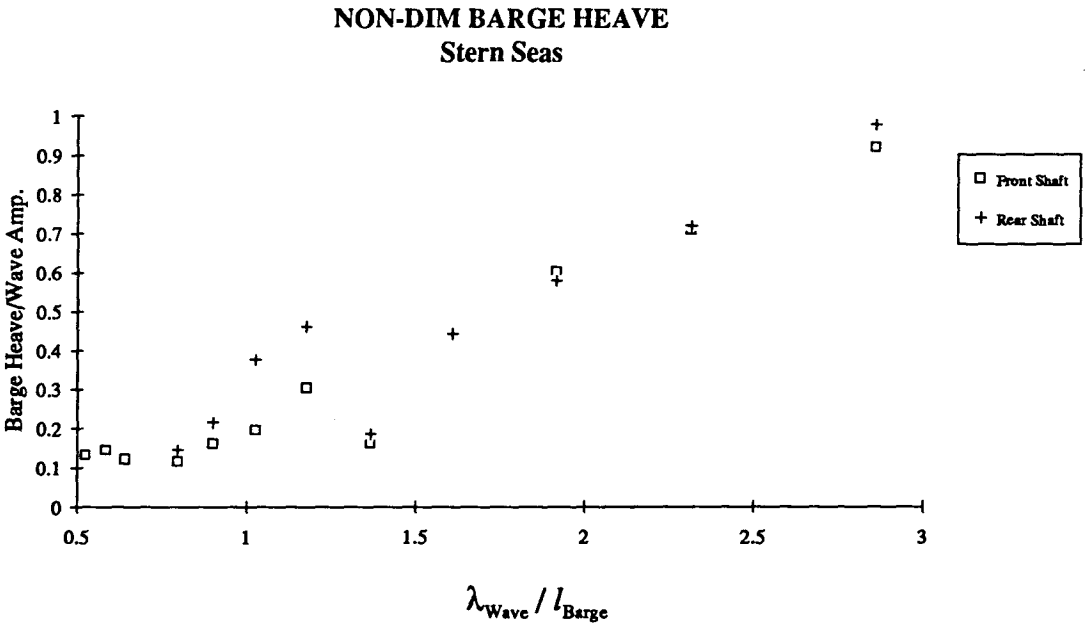

Graph 3.6 : Non-Dimensionalized Barge Heave - Stern Seas

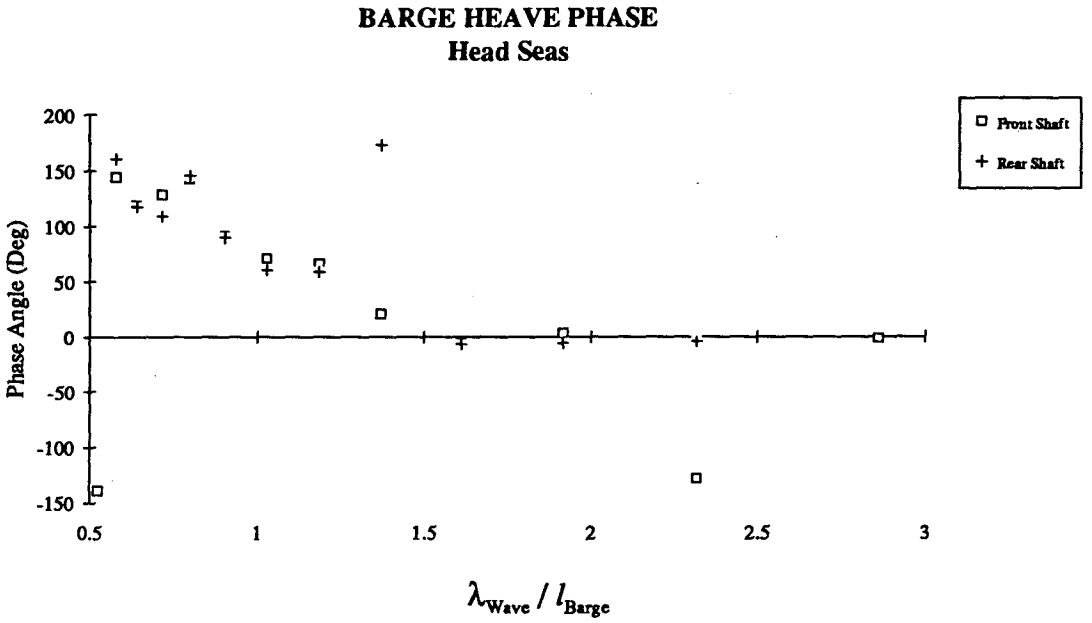

Graph 3.7 : Barge Heave Phase - Head Seas

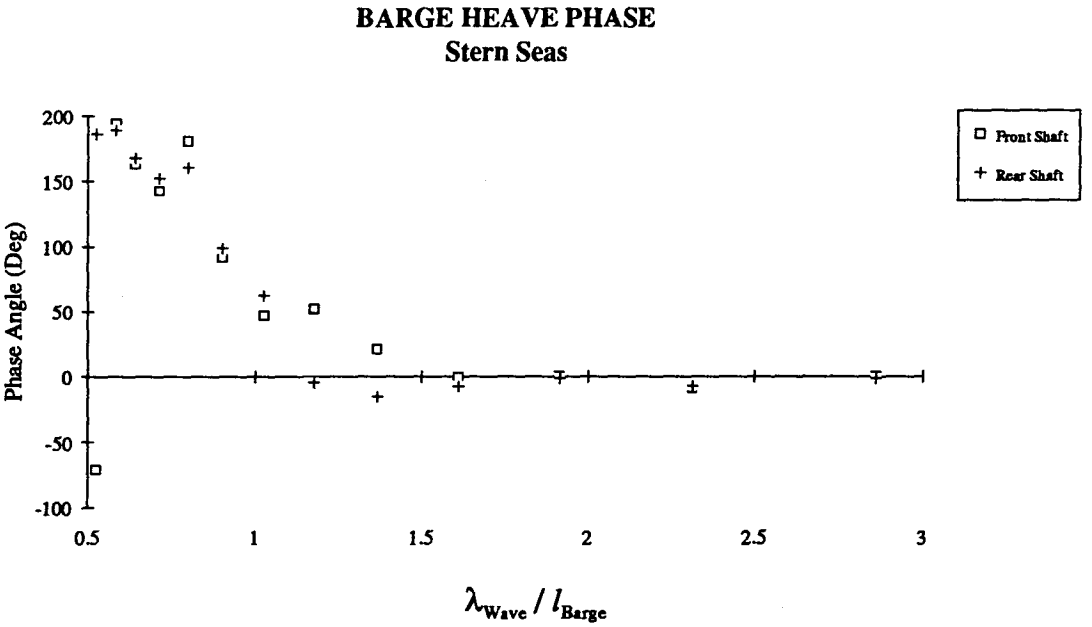

Graph 3.8 : Barge Heave Phase - Stern Seas

3.6.2.2 Barge Trim

The barge trim magnitude is plotted in Graphs 3.9 and 3.10 for head and following seas respectively. The rear shaft position gives a slightly larger trim angle than the forward mounting at wavelengths greater than $1.5l_{Barge}$ for both head and following seas. This may be due to moving the bearing unit mass towards the barge stern when the shaft is moved back. The trim angle magnitudes are very similar for both headings. The trim angle increases steeply between wavelengths of $0.5l_{Barge}$ and $1.5l_{Barge}$ before leveling off at the longer wavelengths as the barge trim becomes a constant 90° out of phase.

Graphs 3.11 (head seas) and 3.12 (stern seas) indicate that the phase angle is unaffected by the change in shaft position. The barge trim is approximately 180° out of phase at wavelengths close to $0.5l_{Barge}$. In head seas this phase difference changes rapidly to a 90° phase lag before λ_{Wave} reaches $0.75l_{Barge}$ (in stern seas the phase difference becomes a 90° phase lead). This phase difference remains constant as the wavelength increases. Physically this lag (or lead) can be described as the barge rising up the slope of the wave- the maximum slope of a cosine wave is reached at 90° or -90°.

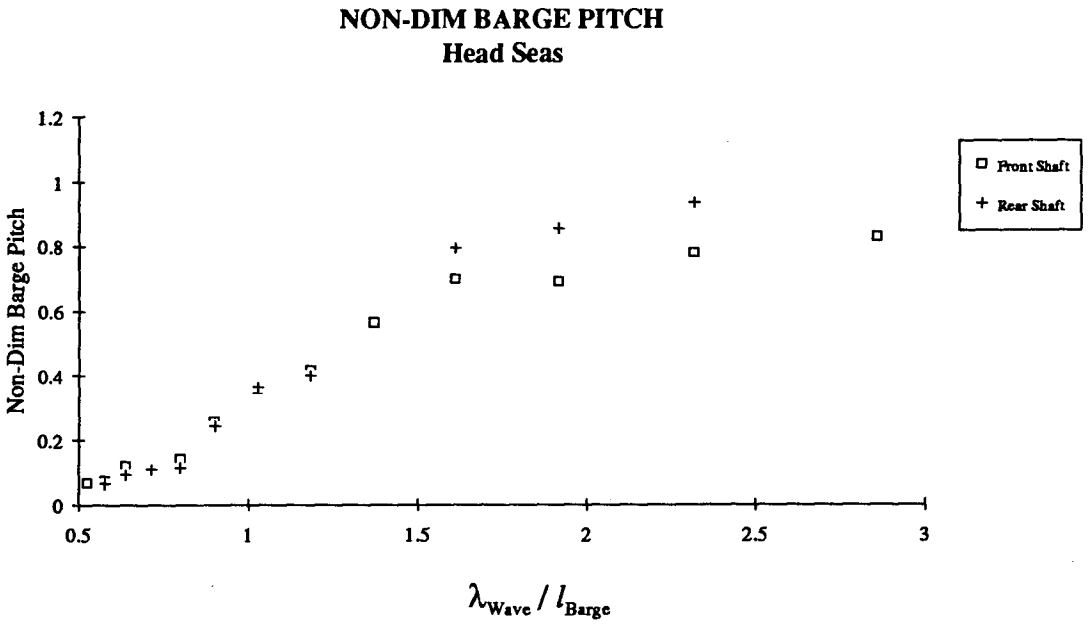

Graph 3.9 : Non-Dimensionalized Barge Pitch - Head Seas

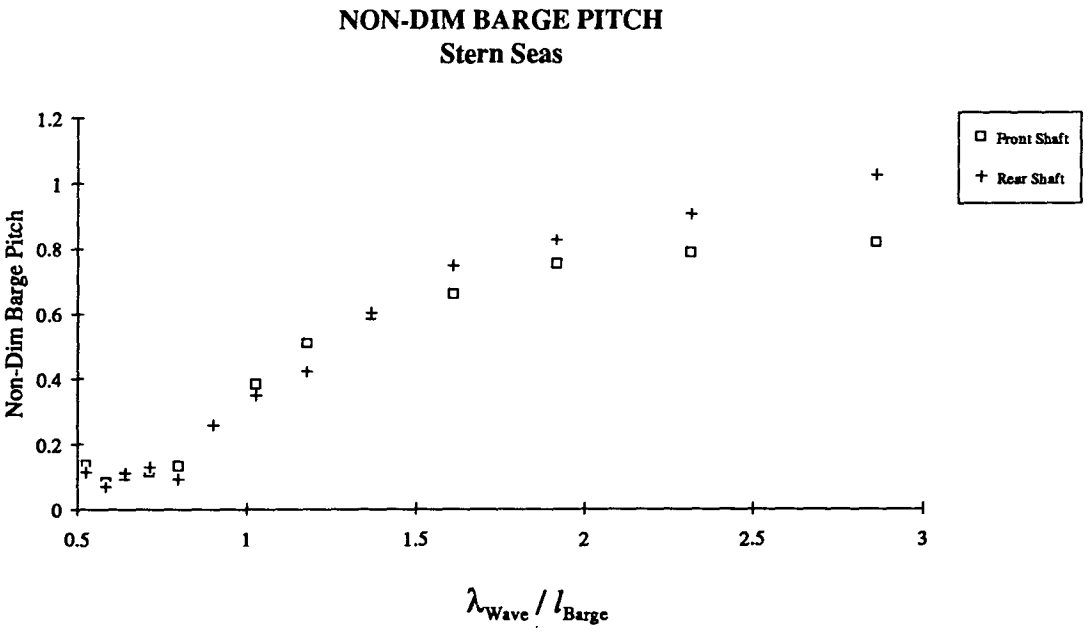

Graph 3.10 : Non-Dimensionalized Barge Pitch - Stern Seas

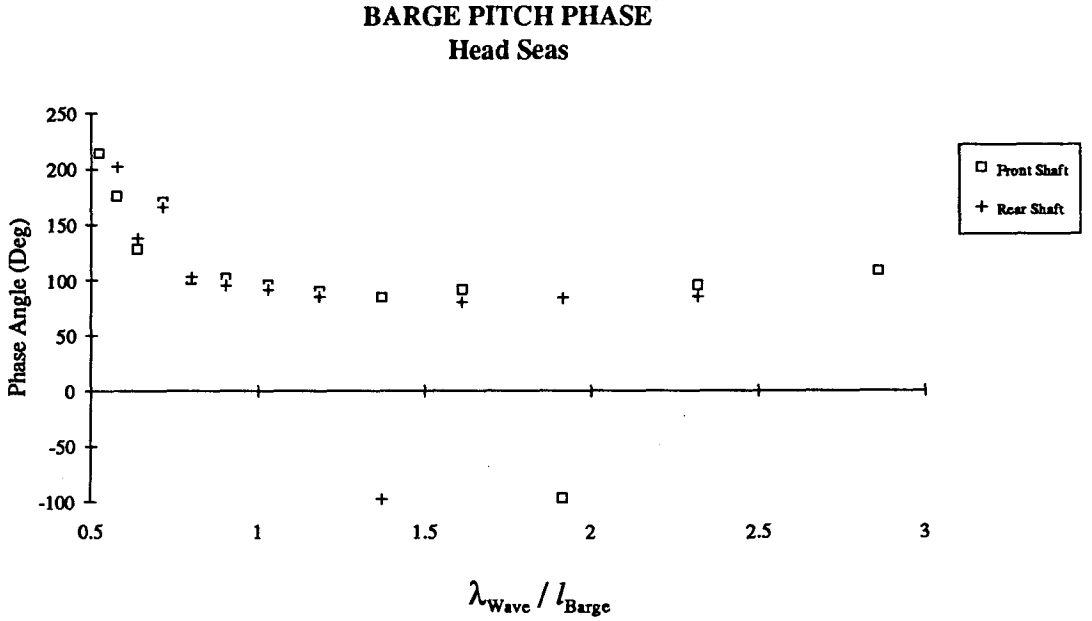

Graph 3.11 : Barge Pitch Phase - Head Seas

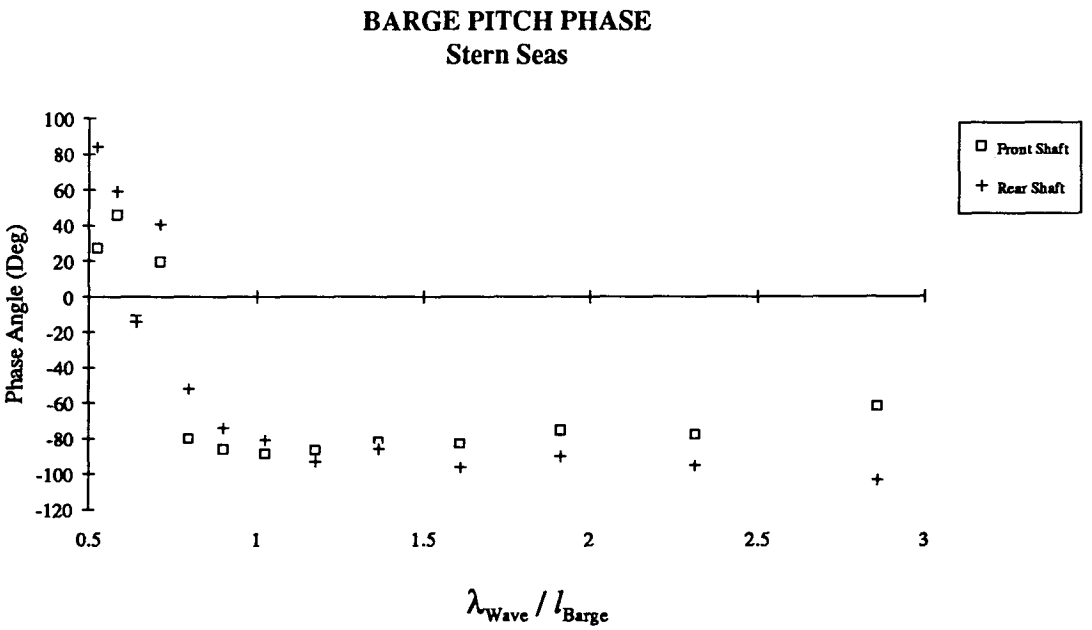

Graph 3.12 : Barge Pitch Phase - Stern Seas

3.6.2.3 Pivoting

The magnitude of the pivot angle in head seas (graph 3.13) and stern seas (graph 3.14) is affected by both the wave direction and the pivot location. Moving the shaft back results in a larger pivot angle between the tug and barge for both sea directions at wavelengths longer than the barge length. The pivot location appears to have little effect on the pivot angle for wavelengths shorter than this.

The head sea condition produces very small pivot angles at short wavelengths. The pivot angle reaches a minimum in both sea directions at a wavelength of $0.6l_{Barge}$ but the angle magnitude in stern seas is approximately 4 times larger than in head seas. The pivot angle in stern seas reaches a maximum at a wavelength of approximately $1.1l_{Barge}$ while the head sea condition reaches its peak at approximately $1.5l_{Barge}$. At higher wavelengths the two sea conditions produce similar pivot angles. One possible reason is that in stern seas the bluff stern of the barge is directly affected by the incident waves at shorter wavelengths as well as the direct effect of the waves on the tug. In head seas the barge bow presents a smoother hydrodynamic profile to the incident waves while the tug is sheltered by the greater beam of the barge.

The phase angles in graphs 3.15 and 3.16 are measured at the pivot location relative to the wave phase at the centre of gravity of the barge. The phase difference of the pivot angles in both sea conditions is unaffected by the change in pivot location. The head sea case increases from a 90° phase lead to a 150° phase lag. The stern sea results reflect this by decreasing from a 90° phase lag to a 150° phase lead. These phase differences can be physically described as the position of the tug on the incident wave when the centre of gravity of the barge is at the incident wave peak.

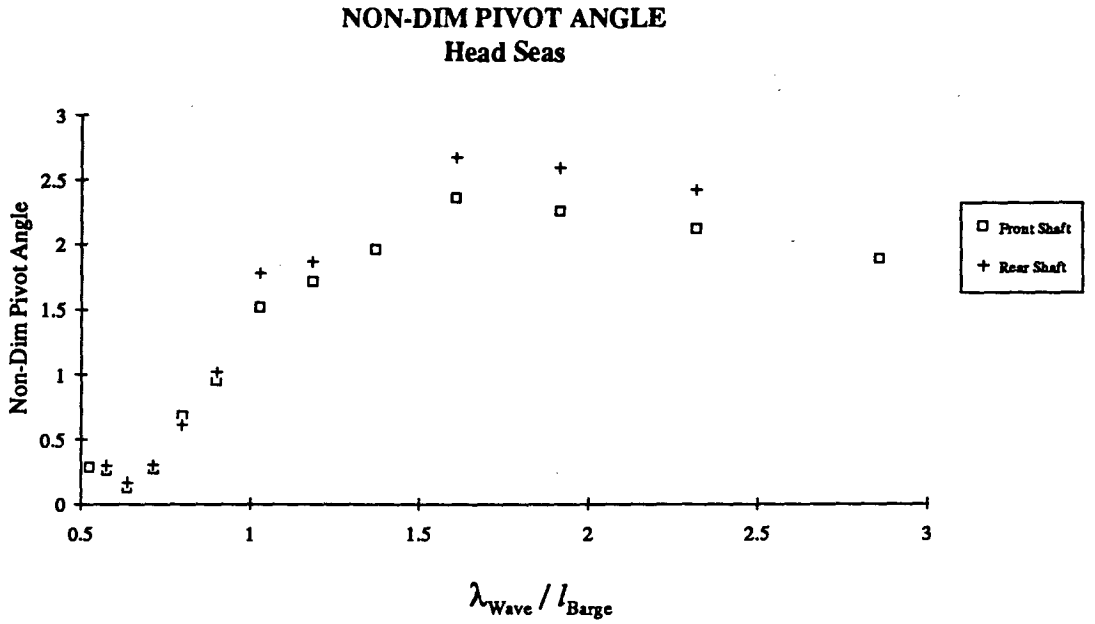

Graph 3.13 : Non-Dimensionalized Pivot Angle - Head Seas

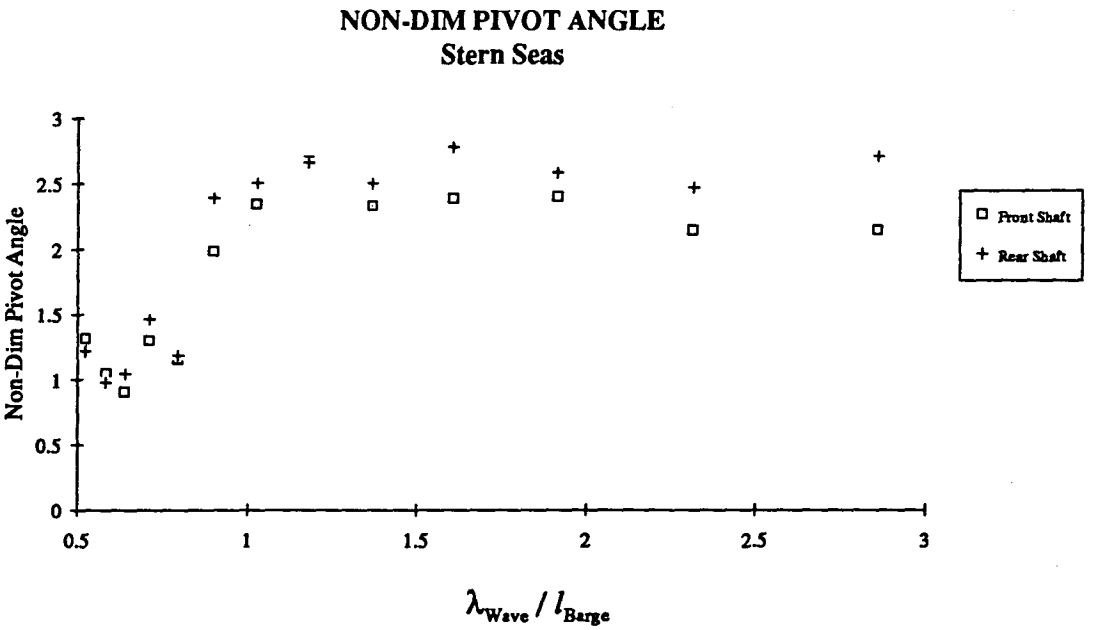

Graph 3.14 : Non-Dimensionalized Pivot Angle - Stern Seas

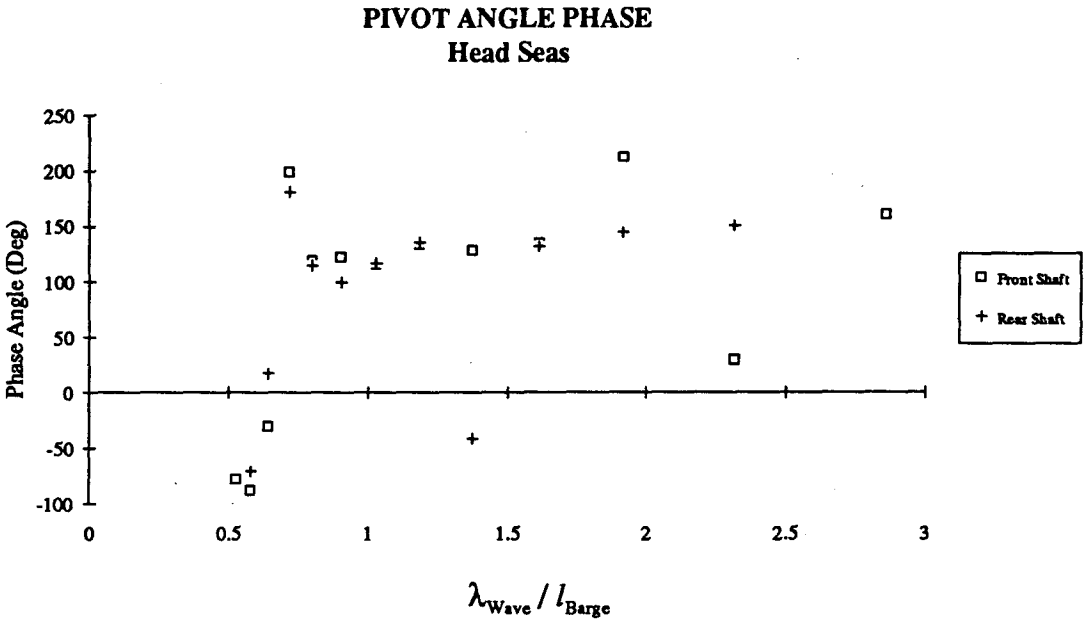

Graph 3.15 : Pivot Angle Phase - Head Seas

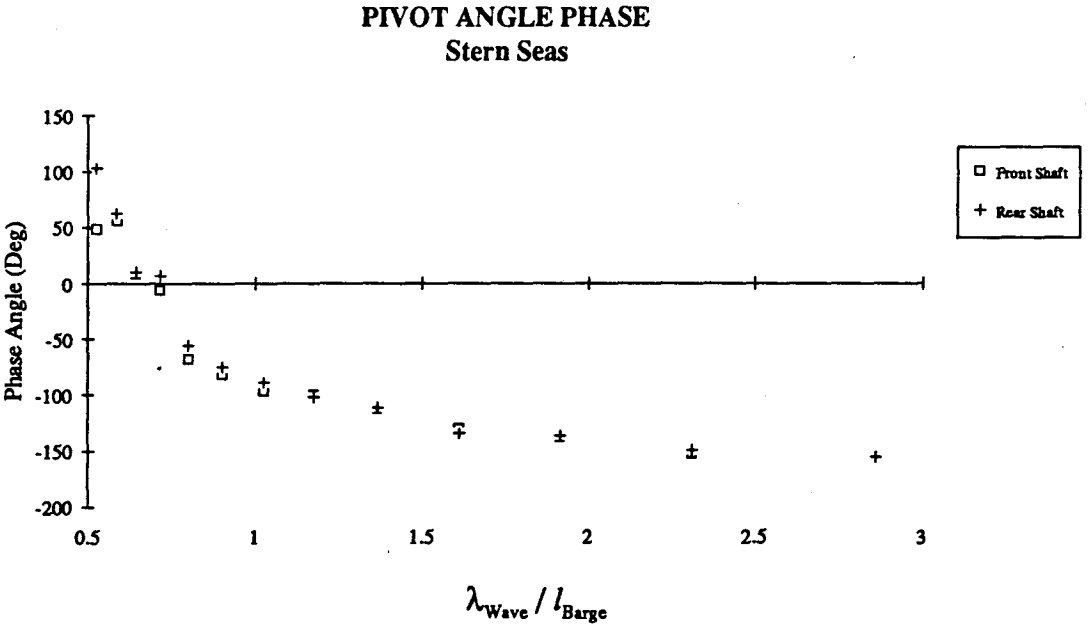

Graph 3.16 : Pivot Angle Phase - Stern Seas

3.6.2.4 Horizontal Force

The horizontal forces could not be analyzed as a linear response to the wave excitation. The force measurement showed second and higher order harmonics caused by the surge of the tug and barge relative to each other. The total force would be the sum of the drag force on the aft hull (i.e. the tug in head seas) and the force due to the non-sinusoidal surging of the hulls about the pivot axis.

3.6.2.5 Vertical Pin Force

Graphs 3.17 and 3.18 indicate that the force on the coupling is much higher when the pivot location is moved back. The rearward mounting produces higher forces at all wavelengths except those shorter than the barge length in head seas where the force is the same for both pivot locations.

The wave direction is also important with stern seas producing much higher peak forces than the head sea case. As in the pivot angle discussion the possible cause is that in the stern sea direction the barge stern is directly affected by the wave action. The peak force occurs at $\lambda_{Wave} \approx 1.2 l_{Barge}$ (equivalent to the total model length) in head seas and at $\lambda_{Wave} \approx l_{Barge}$ in stern seas. A minimum force occurs at $\lambda_{Wave} \approx 0.6 l_{Barge}$ for both wave directions and pivot locations. The force in stern seas at this wavelength is approximately 4 times larger than the force in head seas (at the rear shaft position). These results are similar to the pivot angle results in section 3.6.2.4. At wavelengths longer than $2 l_{Barge}$ the stern and head seas both produce similar forces.

The phase angles are measured at the pivot with respect to the incident wave at the centre of gravity of the barge. The rear shaft position has a lower phase difference than the forward shaft location at all tested frequencies. This difference is expected due to the distances between the shafts. It is about d/λ in magnitude where d is the distance between the pivot locations.

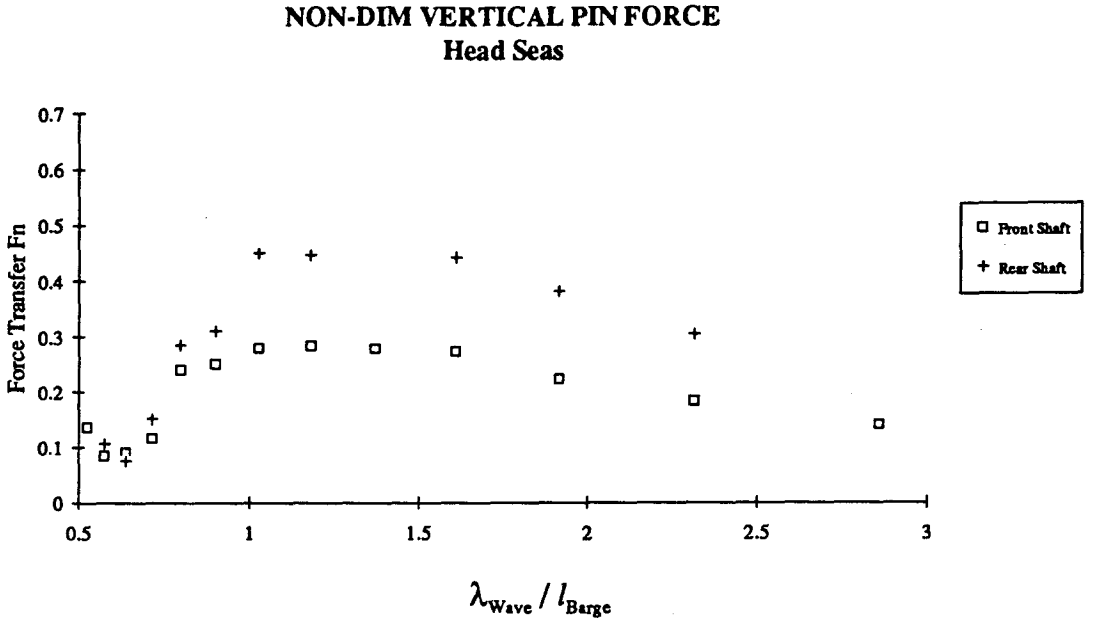

Graph 3.17 : Non-Dimensionalized Vertical Pin Force - Head Seas

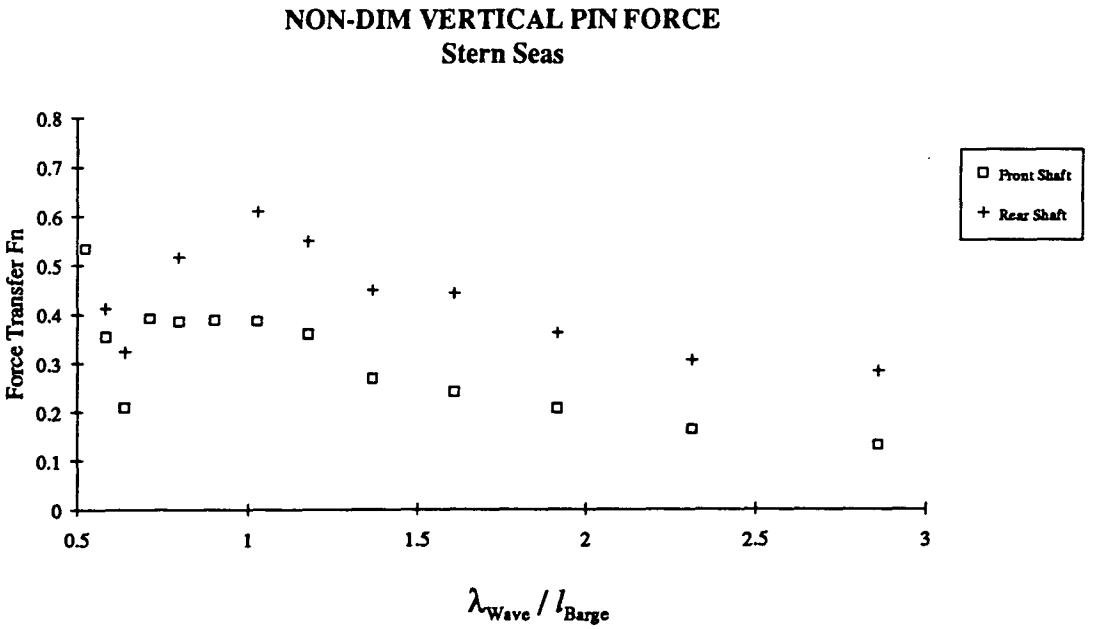

Graph 3.18 : Non-Dimensionalized Vertical Pin Force - Stern Seas

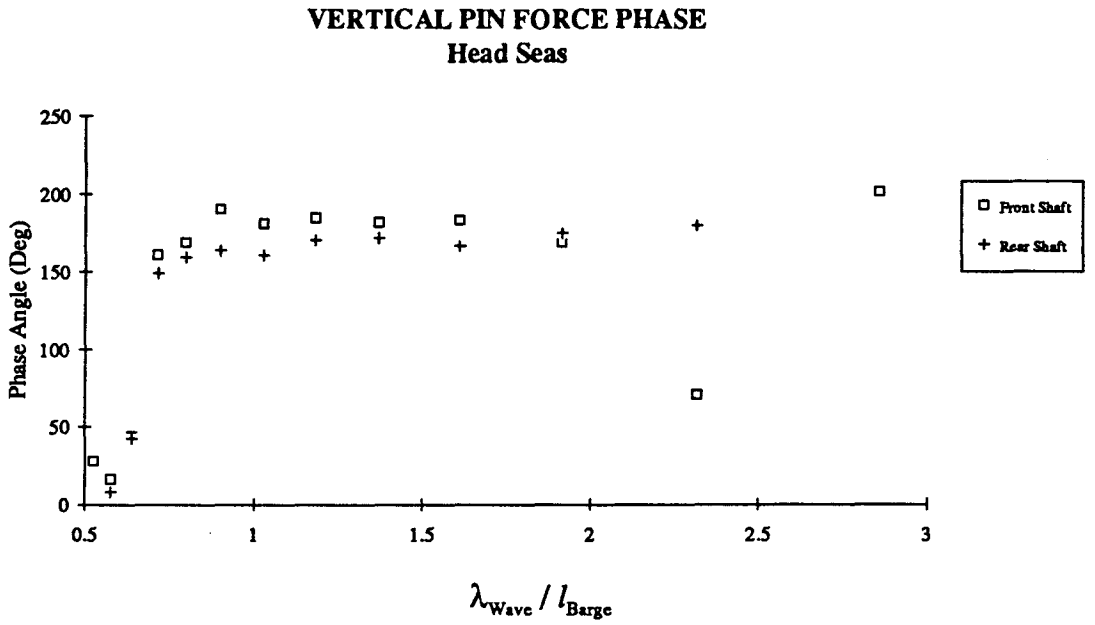

Graph 3.19 : Vertical Pin Force Phase - Head Seas

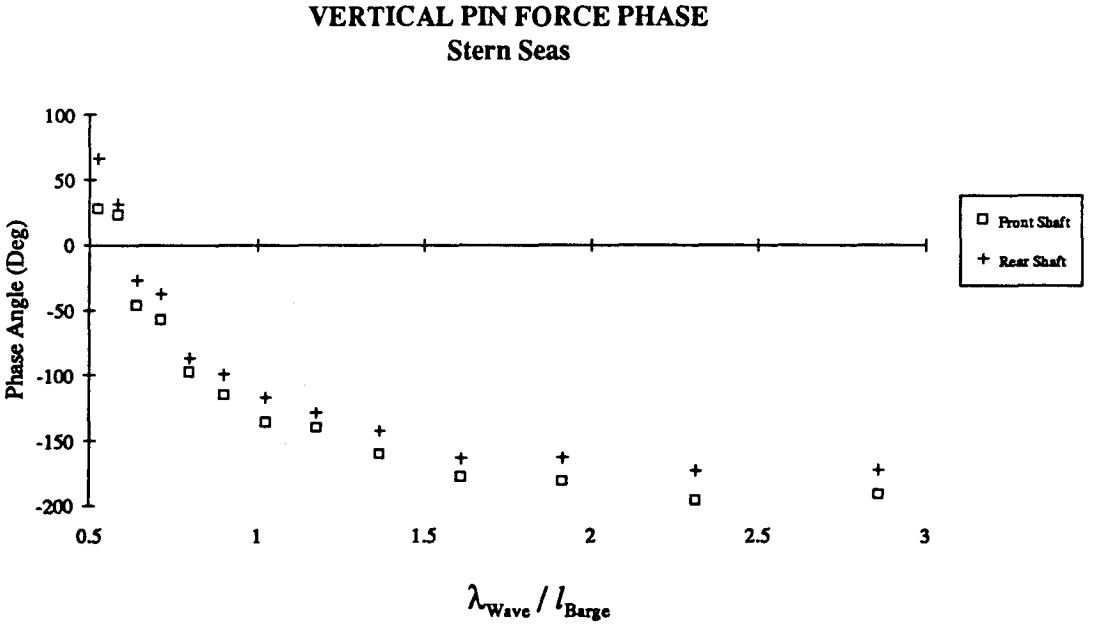

Graph 3.20 : Vertical Pin Force Phase - Stern Seas

3.7 Conclusions

The vertical loads on the coupling between the tug and barge are affected by both the pivot location and the wave direction; if the pivot point is moved back on the tug the forces increase. The pivot angle also increases as the pivot location is moved rearwards but the barge heave and trim are almost unaffected. This can be attributed to the much larger displacement of the barge than the tug.

The pin forces are highest in stern seas at wavelengths slightly greater than the length of the barge. The head sea case produces a maximum pin force at wavelengths close to the barge length. This force may be lower than the stern sea result because of the sheltering effect of the barge beam on the much smaller tug in head seas. The pin forces are proportional to the pivot angle between the tug and barge with the pin forces increasing with this angle. The pivot angle in the stern sea condition is much larger than in head seas at wavelengths less than $1.5l_{\text{Barge}}$. The barge heave and trim are similar in both sea conditions.

The phase angles describe the relative position of the barge and tug to the incident wave at the centre of gravity of the barge. The phase angles of the pin forces reflect a slight change when the shaft is moved rearward (as expected) but no effect is seen on the phase of the pivot angles.

The principal aim of these experiments was to provide a basis for comparison of the theoretical work in Chapter 2. Chapter 4 describes a numerical application of the work in Chapter 2 and compares it to these experimental results.

Chapter 4

Numerical Solution

4.1 General

The numerical solution of the potential flow theory was written in the language C++ on a personal computer. C++ is an Object-Oriented Programming language which allows the user to write compact code which can be easily modified. The numerical solution follows the theoretical derivation in Chapter 2.

The full solution for a single vessel involves discretizing the hull into several two-dimensional sections. The potential and velocity flow are found around each section allowing the far-field source strength σ_{2D} to be determined. These far-field source strengths are then used to determine the three-dimensional source strengths q_j and an interaction function $C_j(x)$ thus defining the unified solution. The three-dimensional hydrodynamic and excitation forces are calculated with this interaction function.

Results show that both the two and the three-dimensional solutions for the hydrodynamic forces agree with experimental and previous results. These forces are combined with the hydrostatic forces and masses for the tug-barge system to solve for the vertical force on the coupling. Two cases are considered; the first assuming no interaction between the two hulls, and the second assuming an interaction effect between the two hulls. The first case follows the previous work of Robinson by solving the hydrodynamic terms for each hull separately. The second case combines the two hulls as a single hinged unit and solves the hydrodynamic terms by including the interaction between the two hulls.

4.2 Two-Dimensional Results

The numerical solution of a symmetric two-dimensional hull section uses pulsating sources located on a line segment describing the hull profile. Integrating the potentials of these sources around the hull solves the two-dimensional potential (for the heave mode). This determines the far-field source strength σ_{2D} and the added mass and damping for each section where

$$\sigma_{2D} = -i2\left(\lim_{x\to\infty} \phi_{2D}\right)e^{-ky}e^{ikx} \tag{4.1}$$

and

$$-\omega^2 m_{ij} + i\omega c_{ij} = -i\omega\rho\iint_S n_i n_j \phi_{2D}\, dS \tag{4.2}$$

The numerical solution for these terms is derived in Appendix A.

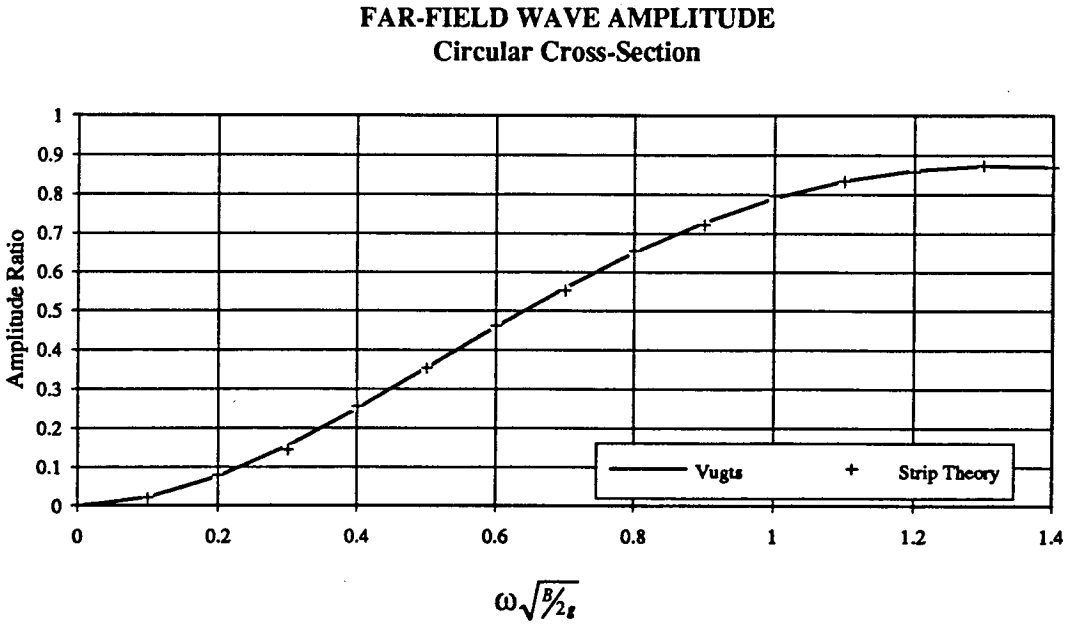

Graph 4.1 : Far-Field Wave Amplitude A_{2D}

The far-field wave amplitude A_{2D} is related to the source strength σ_{2D} by $A_{2D} = 2\frac{g}{\omega}\sigma_{2D}$. Graph 4.1 compares the calculated results for A_{2D} to those of Vugts (1968).

The added mass and damping predictions of the code are compared with the corresponding charts by Bhattacharya (1978). Graph 4.2 and Graph 4.3 show the non-dimensionalized added mass and damping respectively plotted against non-dimensionalized frequency for a beam to draft ratio of 2.0 and a section coefficient of $\beta_A = 0.8$. The factors for non-dimensionalizing the added mass and damping are

$$C = \frac{m_{22}^{2D}}{\rho \frac{\pi}{8} B^2} \tag{4.3}$$

$$\overline{A} = \sqrt{\frac{\omega^3 c_{22}^{2D}}{\rho g^2}} \tag{4.4}$$

A further comparison of these results was made to the strip theory results obtained by Newman for the same hull. In his paper on Unified Slender Body Theory (1979) Newman compares strip theory and unified slender body theory with experimental results obtained by Gerritsma (1966). The strip theory results are integrated around the hull and compare very accurately with those of Newman. The heave, pitch and coupled added mass and damping are shown in graphs 4.4 to 4.9.

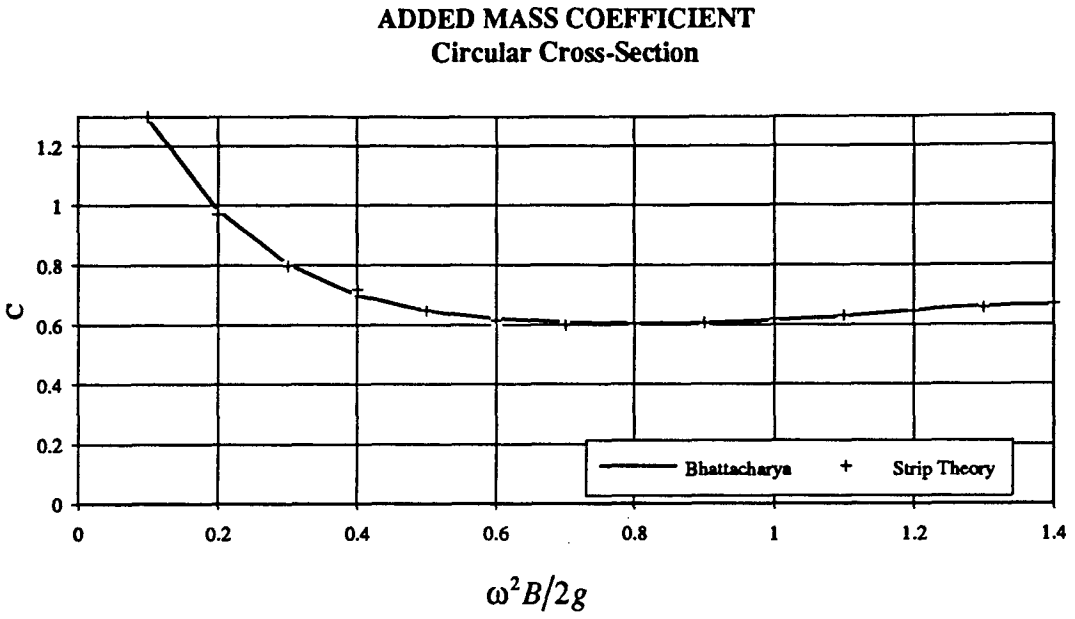

Graph 4.2 : Non-Dimensionalized 2-D Added Mass (C)

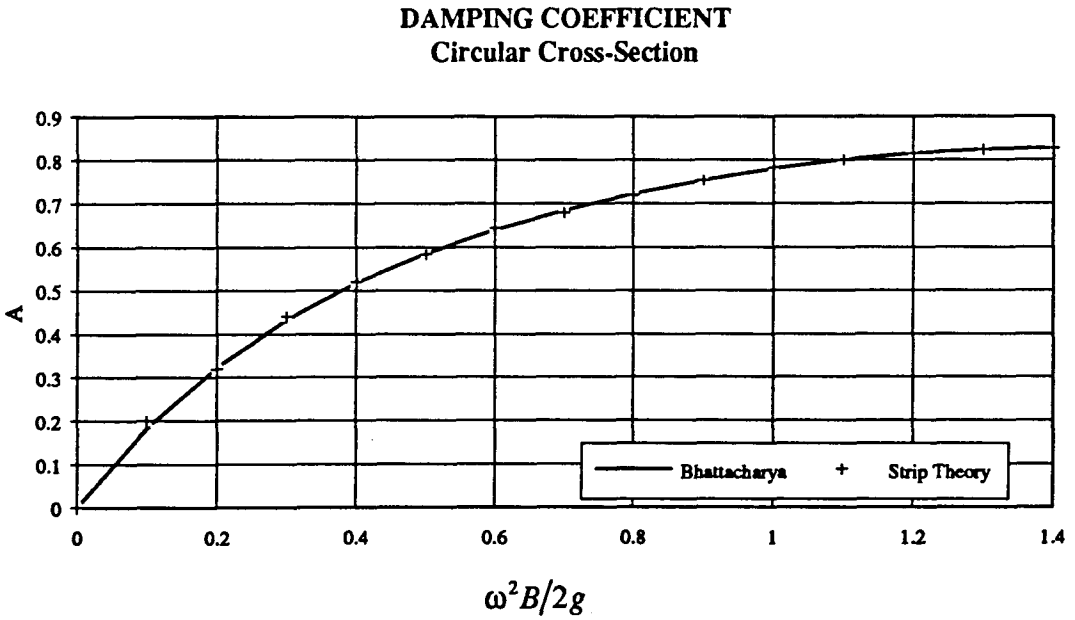

Graph 4.3 : Non-Dimensionalized 2-D Damping ($\overline{A}$)

4.3 Three-Dimensional Results

The numerical model for a single vessel uses Simpson's method to integrate an odd number of equally spaced two-dimensional hull profiles along the hull. Appendix B details this integration using equation (2.22) combined with the sectional far-field source strength σ_{2D} to find the three-dimensional source strengths q_j. Equation (2.22) is repeated here

$$q_j(x)-\left(\frac{\sigma_j+\overline{\sigma}_j}{2\pi i\overline{\sigma}_j}\right)L(q_j)=\sigma_j \tag{4.5}$$

where :

$$\begin{aligned} L(q_j)=&[\gamma+\pi i]q_j(x)+\tfrac{1}{2}\int_L \operatorname{sgn}(x-\xi)\ln(2k|x-\xi|)\frac{d}{d\xi}q_j(\xi)d\xi \\ &-\frac{\pi}{4}k\int_L\left[Y_0(k|x-\xi|)+H_0(k|x-\xi|)+2iJ_0(k|x-\xi|)\right]q_j(\xi)d\xi \end{aligned} \tag{4.6}$$

Due to the slender body assumption the two end terms are assumed to have source strength values of 0. The interaction function $C_j(x)$ is determined from equation (2.29)

$$C_j=\frac{\frac{q_j}{n_j}-\sigma_{2D}}{\sigma_{2D}+\overline{\sigma_{2D}}} \tag{4.7}$$

This allows the calculation of the hydrodynamic and wave excitation forces using a form of equation (2.18)

$$\varphi_j=n_j\phi_{2D}+n_jC_j(x)\left(\phi_{2D}+\overline{\phi_{2D}}\right) \tag{4.8}$$

The hydrodynamic force equation (2.30) is

$$-\omega^2m_{ij}+i\omega c_{ij}=\int_L n_in_j\left(-\omega^2m_{22}^{2D}+i\omega c_{22}^{2D}\right)+n_i\frac{q_j-n_j\sigma_{2D}}{\sigma_{2D}+\overline{\sigma}_{2D}}\left(2i\omega c_{22}^{2D}\right)dx \tag{4.9}$$

and the excitation force comes from equation (2.34)

$$X_j = \rho \iint_S \left(i\omega n_j \phi_0 - \phi_j \frac{\partial \phi_0}{\partial n} \right) dS - \rho \iint_S n_j C_j(x) \left(\phi_{2D} + \overline{\phi_{2D}} \right) \frac{\partial \phi_0}{\partial n} dS \qquad (4.10)$$

where X_j is the excitation force due to a unit amplitude wave. The excitation force is the only force that is dependent on the incident wave angle.

The results for this application of unified slender body theory match the three-dimensional results of both Newman and Mays (as well as the experimental results of Gerritsma included by Newman). Graphs 4.4 to 4.9 plot the added mass and damping results for the heave, pitch and coupled heave-pitch modes of a Series 60 hull with a block coefficient of 0.70. Graphs 4.10 and 4.11 plot the excitation force and moment respectively on the same hull in head seas against the experimental values found by Vugts (1971). Graphs 4.12 and 4.13 show the excitation force and moment in bow seas. The results of Sclavounos (1981) for the Haskind relations are identical.

The coupled heave-pitch terms must be symmetric by definition. Both of these terms were evaluated to determine the numerical error. The following equation was used:

$$\text{error} = \left(\frac{t_{ij} - t_{ij}^{\text{Avg}}}{\sqrt{t_{ii} t_{jj}}} \right) \times 100\% \qquad (4.11)$$

This error proved to be negligible for all cases.

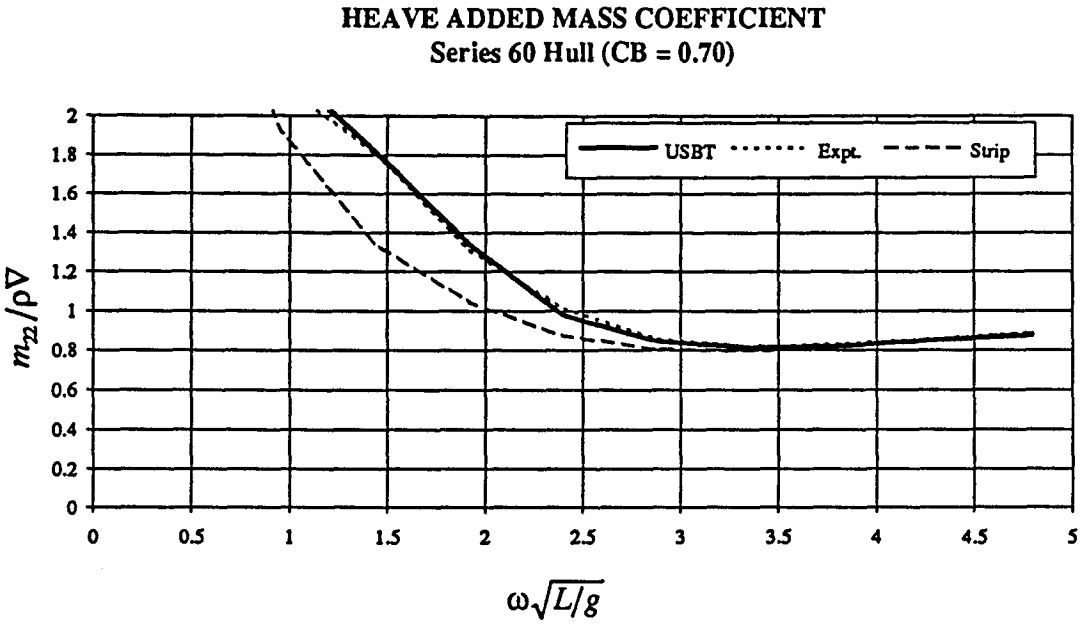

Graph 4.4 : Non-Dimensionalized Added Mass (m_{22})

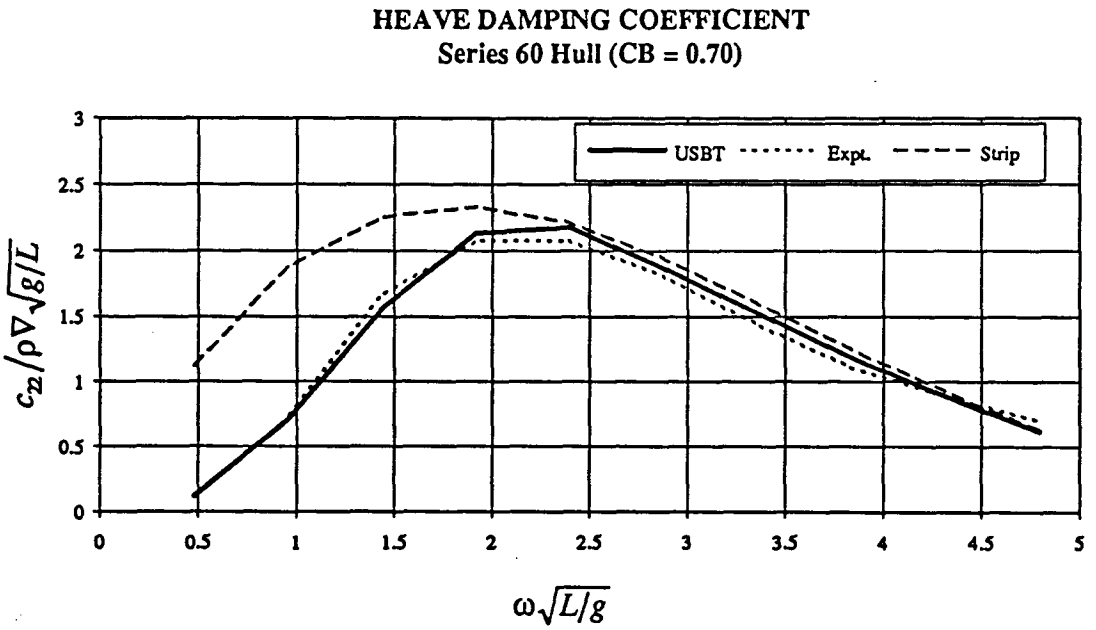

Graph 4.5 : Non-Dimensionalized Damping (c_{22})

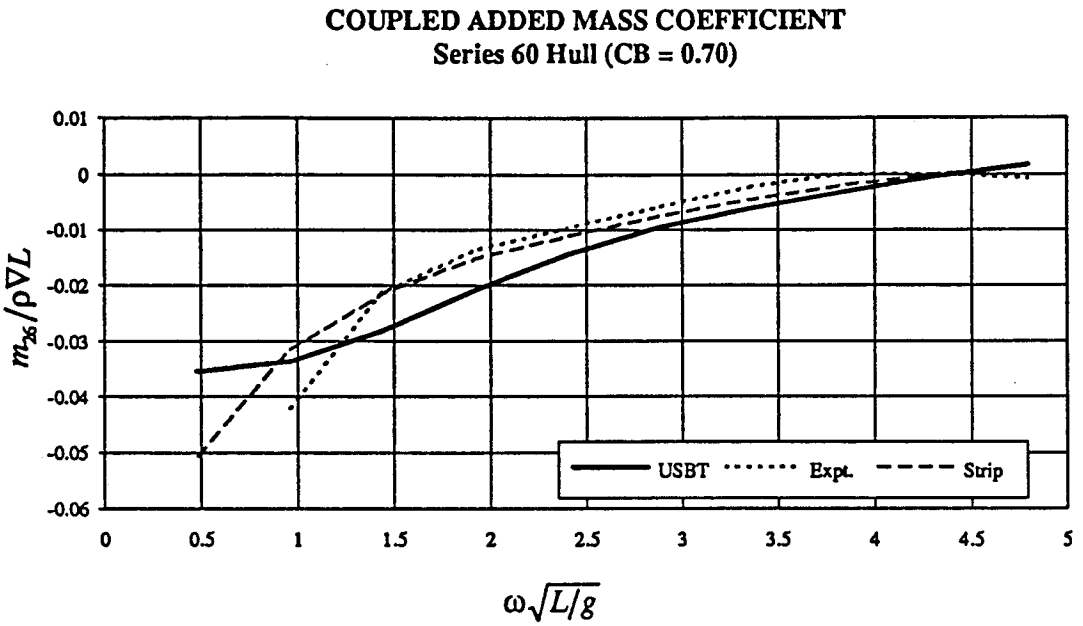

Graph 4.6 : Non-Dimensionalized Added Mass (m_{26})

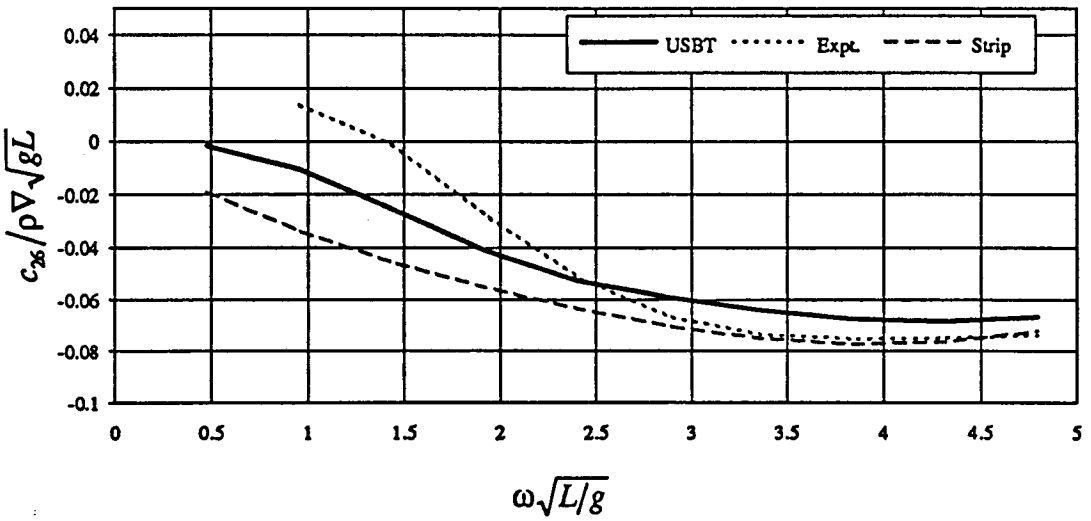

Graph 4.7 : Non-Dimensionalized Damping (c_{26})

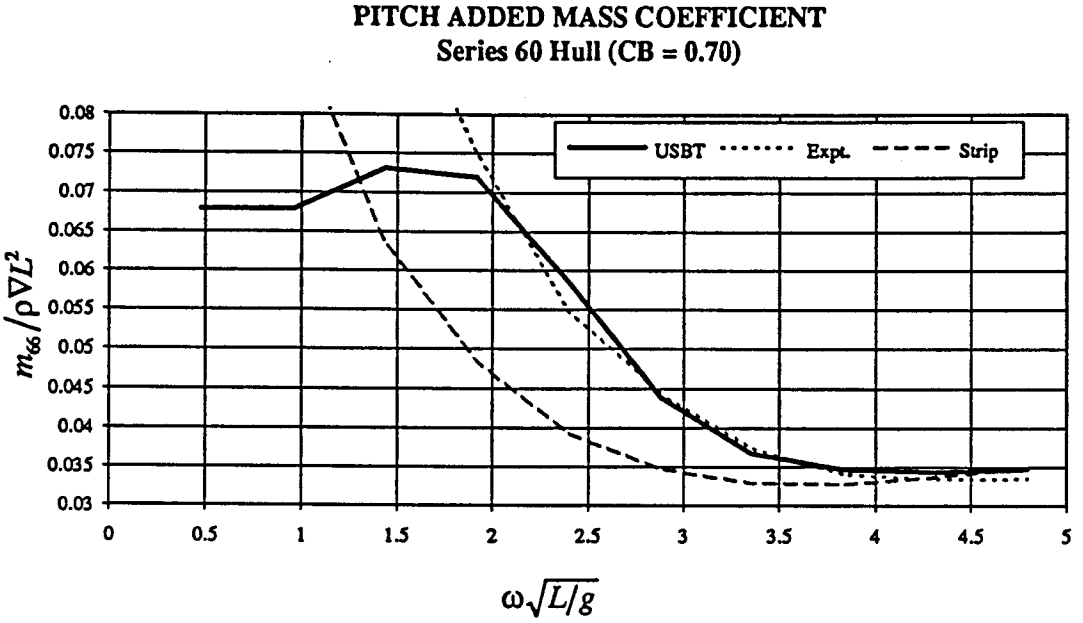

Graph 4.8 : Non-Dimensionalized Added Mass (m_{66})

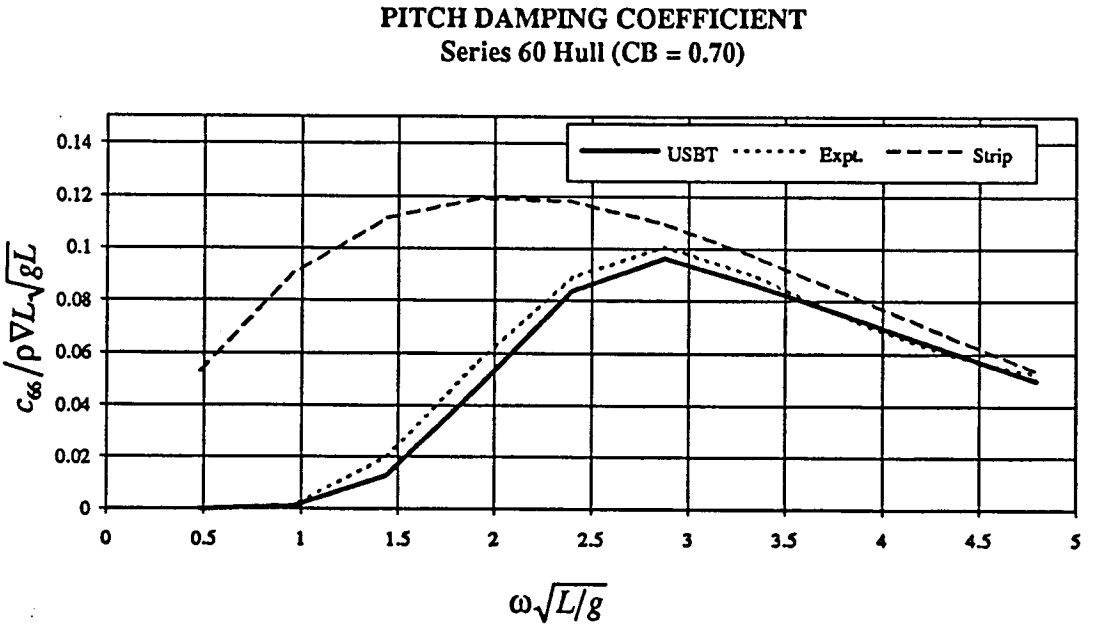

Graph 4.9 : Non-Dimensionalized Damping (c_{66})

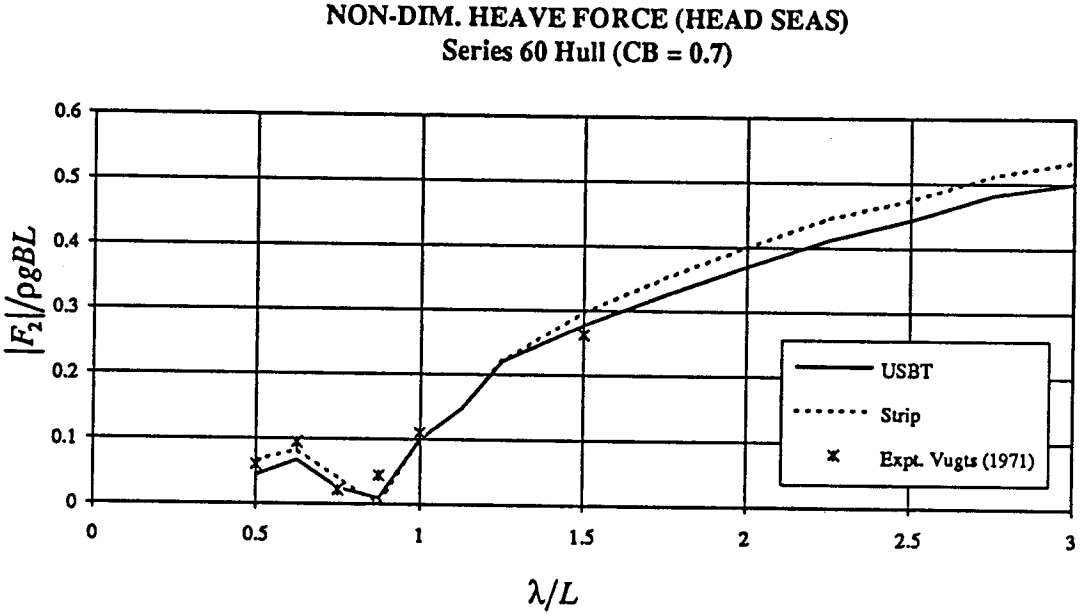

Graph 4.10 : Non-Dimensionalized Heave Excitation Force in Head Seas

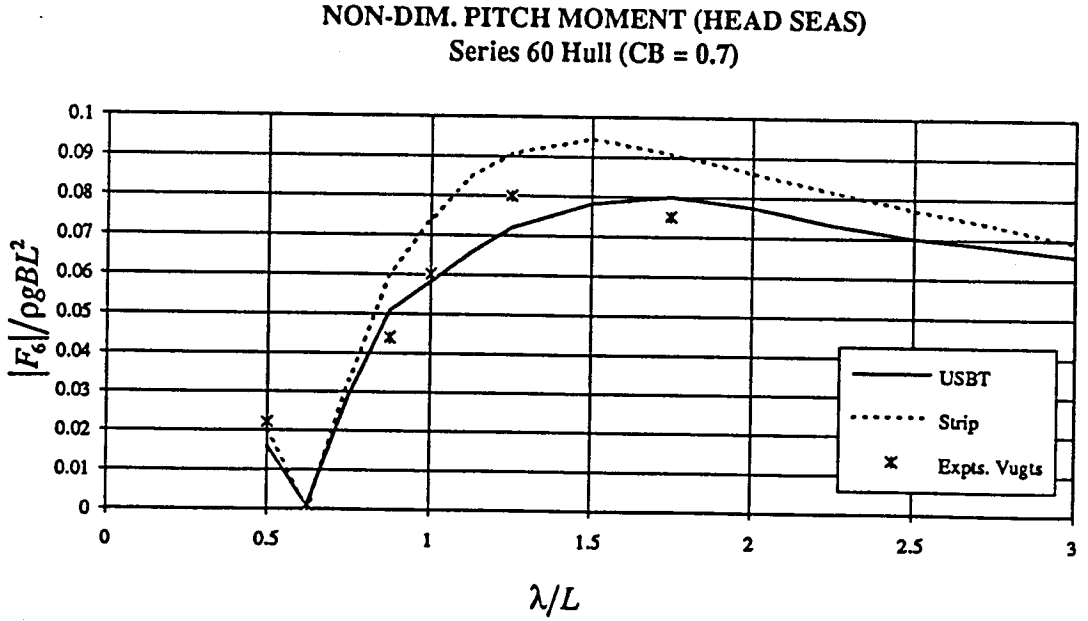

Graph 4.11 : Non-Dimensionalized Pitch Excitation Moment in Head Seas

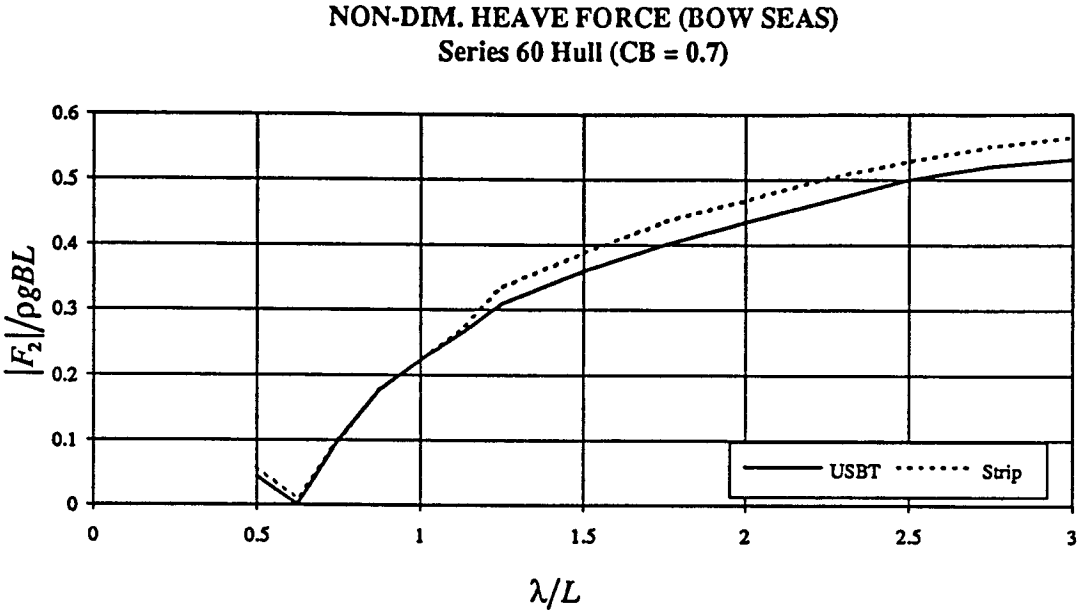

Graph 4.12 : Non-Dimensionalized Heave Excitation Force in Bow Seas

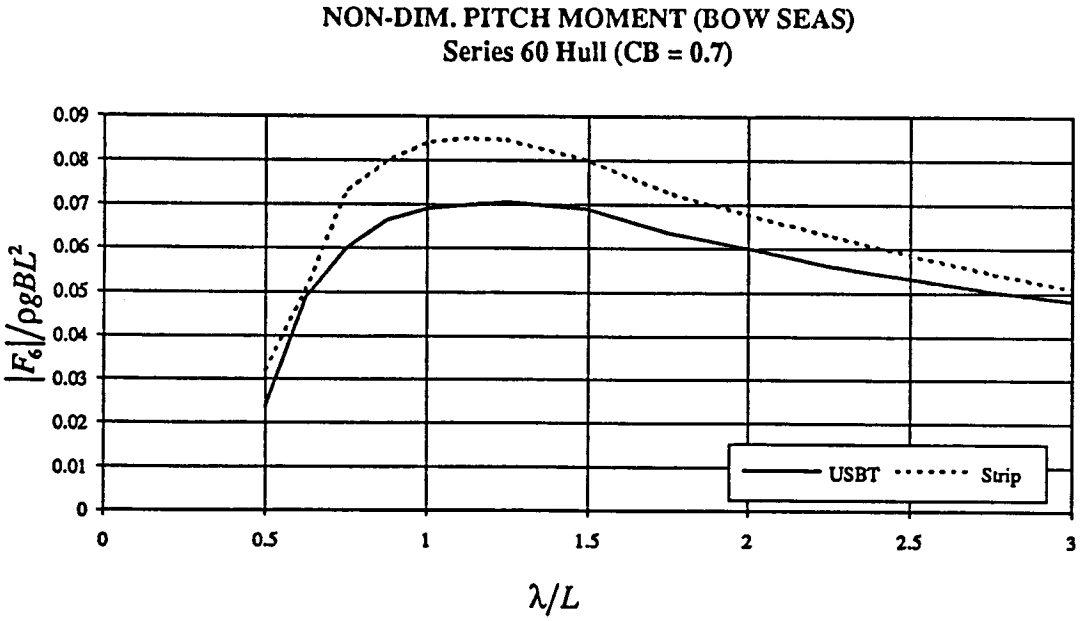

Graph 4.13 : Non-Dimensionalized Pitch Excitation Moment in Bow Seas

4.4 Coupled Tug-Barge

The vertical pin force and the corresponding motions of the tug and barge are obtained by solving equation (2.45).

$$F_{Pin} = \frac{\{B\}^T\left(-\omega^2[M]+[\mathrm{HD}]+[\mathrm{HS}]\right)^{-1}\{\mathrm{F}\}}{\{B\}^T\left(-\omega^2[M]+[\mathrm{HD}]+[\mathrm{HS}]\right)^{-1}\{B\}} \tag{4.12}$$

where

$$\{B\} = \begin{Bmatrix} -1 \\ -l_1 \\ 1 \\ -l_2 \end{Bmatrix} \tag{4.13}$$

The mass and hydrostatic matrices are independent of the coupling between the tug and barge. The hydrodynamic terms consist of the added mass and damping and the excitation force which all depend on the interaction between the two hulls. Two cases can be considered for calculating these hydrodynamic forces :

Case 1: The forces can be calculated independently for each hull assuming no interaction with the other hull

Case 2: The forces can be calculated for a hinged system assuming some interaction between the two hulls.

The former case has been solved by Robinson (1977) for models moving at a scale speed of 16 knots. No literature has been found on the latter case.

4.4.1 Case 1 : Separate Solution

For Case 1 the hydrodynamic forces are calculated exactly as for a single hull so that a (2×2) hydrodynamic matrix and a (1×2) excitation force vector are found for both

the tug and barge. When the two hulls are combined in equation (4.12) the hydrodynamic matrix is of the form

$$[HD]=\begin{bmatrix} -\omega^2 m_{22}^{Tug}+i\omega c_{22}^{Tug} & -\omega^2 m_{26}^{Tug}+i\omega c_{26}^{Tug} & 0 & 0 \\ -\omega^2 m_{62}^{Tug}+i\omega c_{62}^{Tug} & -\omega^2 m_{66}^{Tug}+i\omega c_{66}^{Tug} & 0 & 0 \\ 0 & 0 & -\omega^2 m_{22}^{Barge}+i\omega c_{22}^{Barge} & -\omega^2 m_{26}^{Barge}+i\omega c_{26}^{Barge} \\ 0 & 0 & -\omega^2 m_{62}^{Barge}+i\omega c_{62}^{Barge} & -\omega^2 m_{66}^{Barge}+i\omega c_{66}^{Barge} \end{bmatrix} \tag{4.14}$$

where the added mass and damping are solved by equation (4.9) for each hull. The excitation forces are solved using equation (4.10) for each mode.

Numerically the stern of the barge is difficult to model using slender body theory due to the transom stern and notch. The numerical application of unified theory assumes that the source strength at each end of the hull is zero but the wide stern profile would obviously produce a non-zero source term. The stern of the barge is treated as rounded with the last station forced to a zero source strength. This simplification is not expected to affect the results greatly.

4.4.2 Case 2 : Combined Solution

For Case 2 the mode shapes used to calculate the three-dimensional sources in equation (4.5) are set up as

$$\text{Mode 1} = \begin{cases} 1 & \text{if } \frac{-L_{Tug}}{2} \le x \le \frac{L_{Tug}}{2} \quad \text{i.e. on tug} \\ 0 & \text{if } x > \frac{L_{Tug}}{2} \quad \text{i.e. on barge} \end{cases}$$

$$\text{Mode 2} = \begin{cases} x & \text{if } \frac{-L_{Tug}}{2} \le x \le \frac{L_{Tug}}{2} \quad \text{i.e. on tug} \\ 0 & \text{if } x > \frac{L_{Tug}}{2} \quad \text{i.e. on barge} \end{cases}$$

$$\text{Mode 3} = \begin{cases} 0 & \text{if } x < \frac{-L_{barge}}{2} \text{ i.e. on tug} \\ 1 & \text{if } \frac{-L_{barge}}{2} \le x \le \frac{L_{barge}}{2} \text{ i.e. on barge} \end{cases}$$

$$\text{Mode 4} = \begin{cases} 0 & \text{if } x < \frac{-L_{barge}}{2} \text{ i.e. on tug} \\ x & \text{if } \frac{-L_{barge}}{2} \le x \le \frac{L_{barge}}{2} \text{ i.e. on barge} \end{cases}$$

These four modes are the same as for the Case 1 model except that the coupling terms between the tug and barge can be calculated using the interaction coefficient $C_j(x)$. Equation (4.9) is used for the three-dimensional added mass and damping for the Case 2 model with one modification. The coupling terms between tug and barge (i.e. $-\omega^2 m_{13} + i\omega c_{13}$ - tug heave coupled with barge heave) are determined from the $\int_L n_i \frac{q_j}{\sigma_{2D} + \bar{\sigma}_{2D}} \left(2i\omega c_{22}^{2D}\right) dx$ term. This produces a complete (4×4) symmetric hydrodynamic matrix. The interaction terms for the excitation force in equation (4.10) are also evaluated in this manner.

4.4.2.1 Numerical Model

The combined tug-barge model uses 41 equally spaced sections to allow a Simpson's integration along the hull. Figure 4.1 illustrates the complete model (not to scale) with the individual sections marked. Sections 0 and 40 are modeled as sections having no beam - the source strengths are assumed to be zero at each end. Section 8 is the intersection between the tug and barge and is built as a tug section while section 9 is built as a barge section.

The actual hinge between the tug and barge allows the tug to pivot inside a notch at the rear of the barge. The computer model of this hinge was achieved by breaking the

model at station 8. The tug mode shapes are then defined from station 0 to station 8 and the barge mode shapes from section 9 to section 40. Although this results in the loss of the bow of the tug a comparison of the hydrodynamic matrices and of the excitation force vectors for the two separate models proves this to be a reasonable assumption.

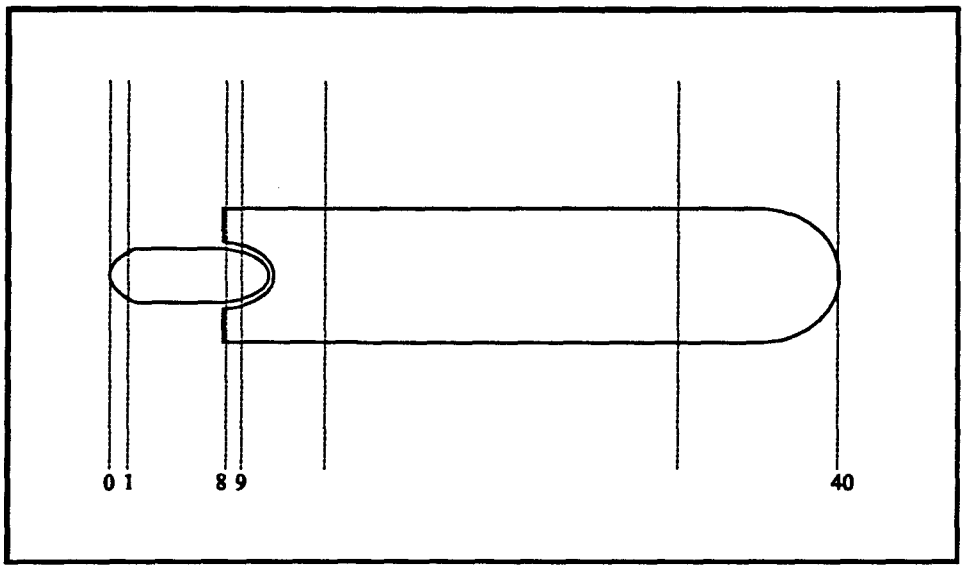

Figure 4.1 Overview of Tug-Barge Sections

4.5 Coupled Tug-Barge Results

The results for the tug-barge system consist of the vertical shear force at the pin, the barge heave and pitch and the tug heave and pitch. As all results are complex numbers the phase angles can also be determined. The experimental results of Chapter 3 replace the tug heave and pitch with the pivot angle between the tug and barge while the phase angles are determined from either the wave or the FFT analysis. In addition the experimental results are evaluated with the incident wave at the centre of gravity of the barge. This is replicated in both numerical models within a global coordinate system.

4.5.1 Barge Heave

The numerical results for the barge heave are presented in Graphs 4.14 and 4.15. These graphs compare the results for the Case 1 and Case 2 tug-barge models with the experimental results of Chapter 3. The magnitude of the heave predicted by both numerical models is very similar. The experimental results in this range are not ideal due to the proximity of the natural frequency of the tank at $\lambda_n = 0.677 l_{\text{Barge}}$. Both models correctly predict that the change in pivot location will have little effect on the heave in either head or stern seas. The calculated heave motion in both sea conditions is less than expected.

Graphs 4.16 and 4.17 show the phase difference The results for the two models are very accurate in both head and stern seas. As expected the change in pivot location does not affect the phase angles.

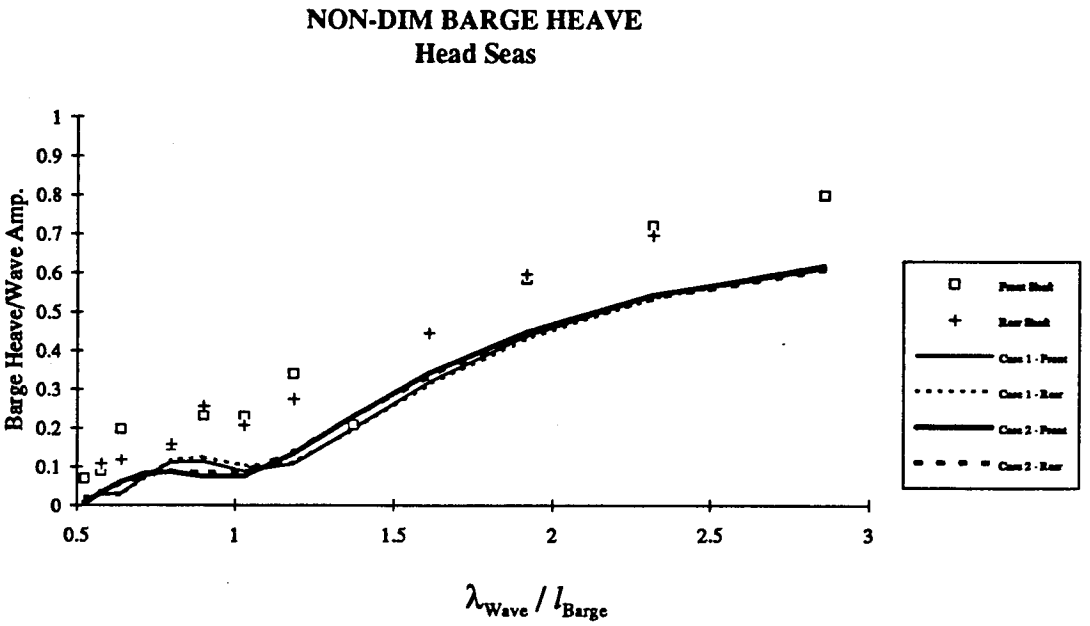

Graph 4.14 : Non-Dimensionalized Barge Heave in Head Seas

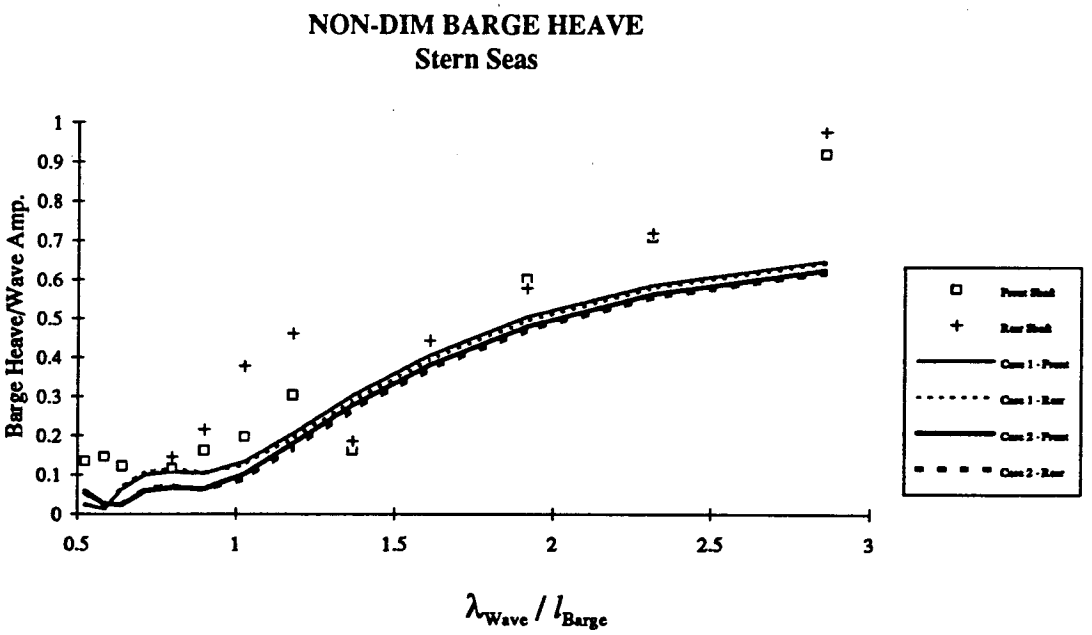

Graph 4.15 : Non-Dimensionalized Barge Heave in Stern Seas

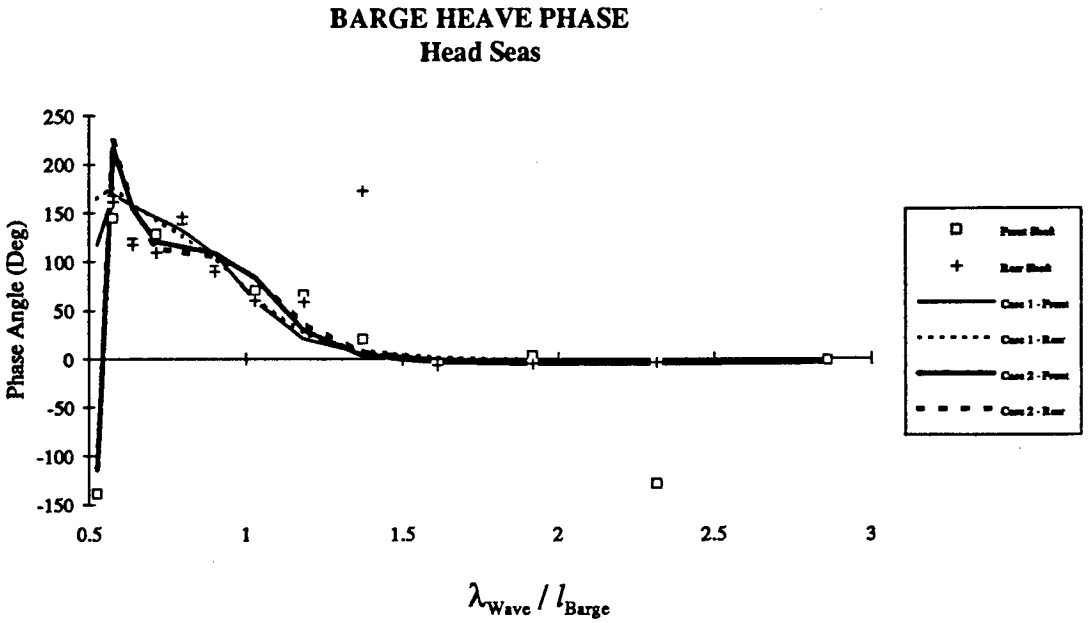

Graph 4.16 : Barge Heave Phase in Head Seas

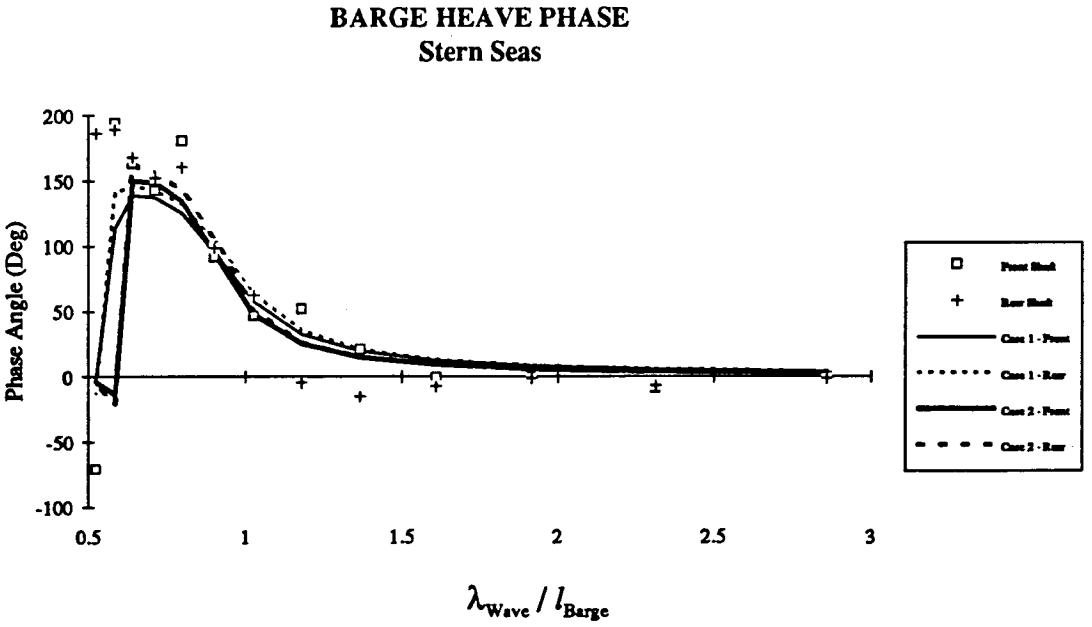

Graph 4.17 : Barge Heave Phase in Stern Seas

4.5.2 Barge Trim

The barge trim in head and stern seas is plotted in Graphs 4.18 and 4.19 respectively. Both numerical models are virtually unaffected by the change in pivot position for either head or stern seas. As suggested in Chapter 3 the experimental variance in the barge trim may be due to moving the bearing assembly.

The numerical models both underpredict the magnitude of the barge trim in head and stern seas. The uncoupled (Case 1) model calculates a slightly larger trim magnitude in both sea conditions.

The phase angles are accurately determined by both the Case 1 and Case 2 models. These results are plotted in graphs 4.18 for head seas and 4.19 for stern seas.

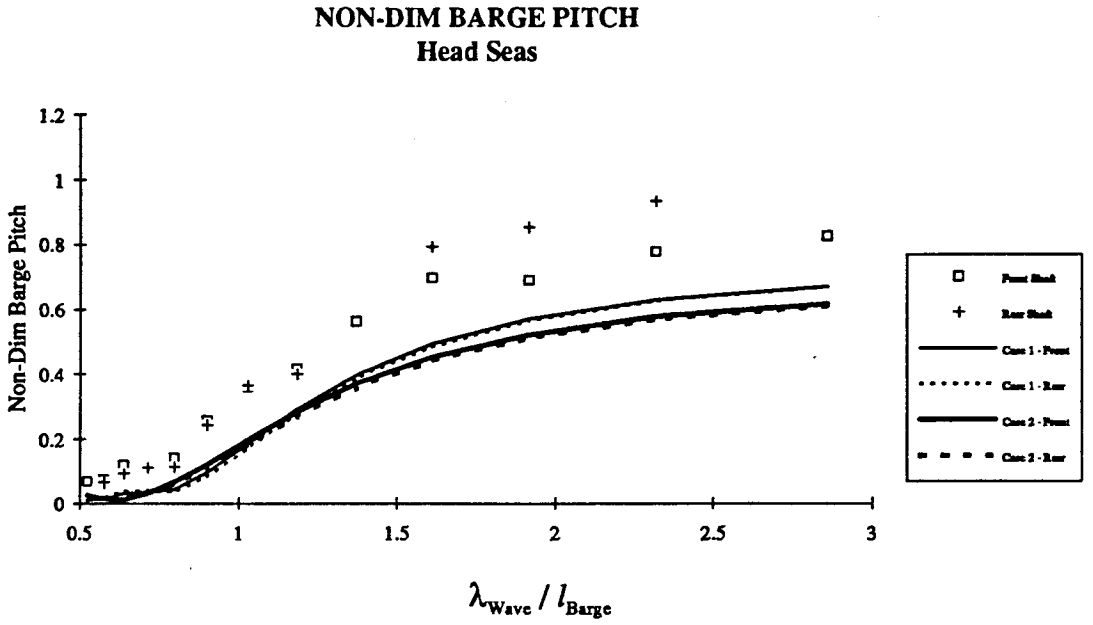

Graph 4.18 : Non-Dimensionalized Barge Pitch in Head Seas

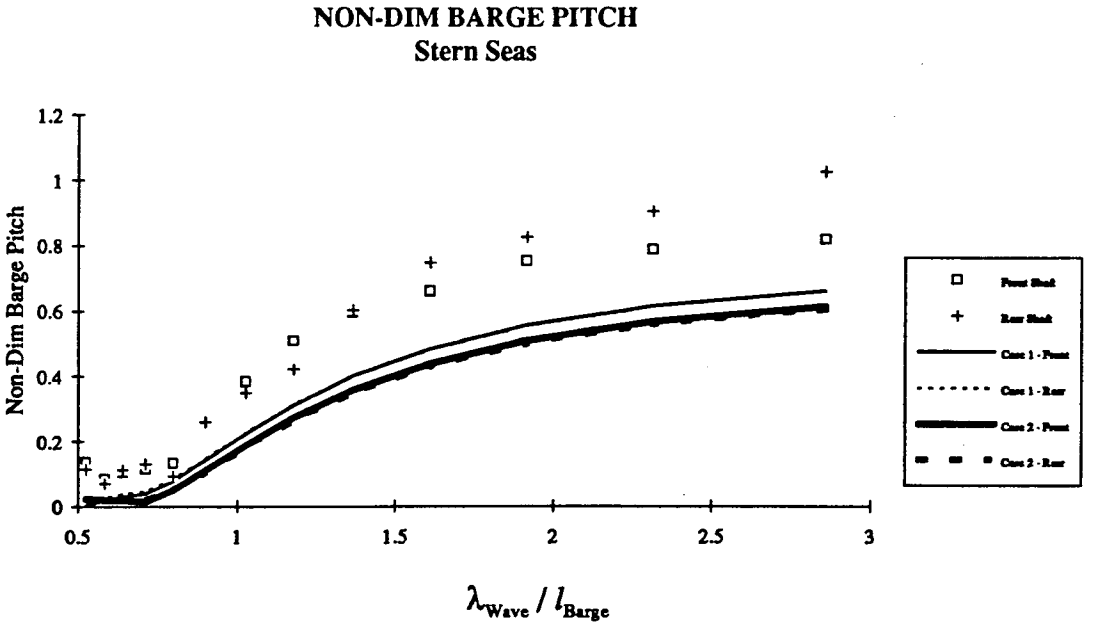

Graph 4.19 : Non-Dimensionalized Barge Pitch in Stern Seas

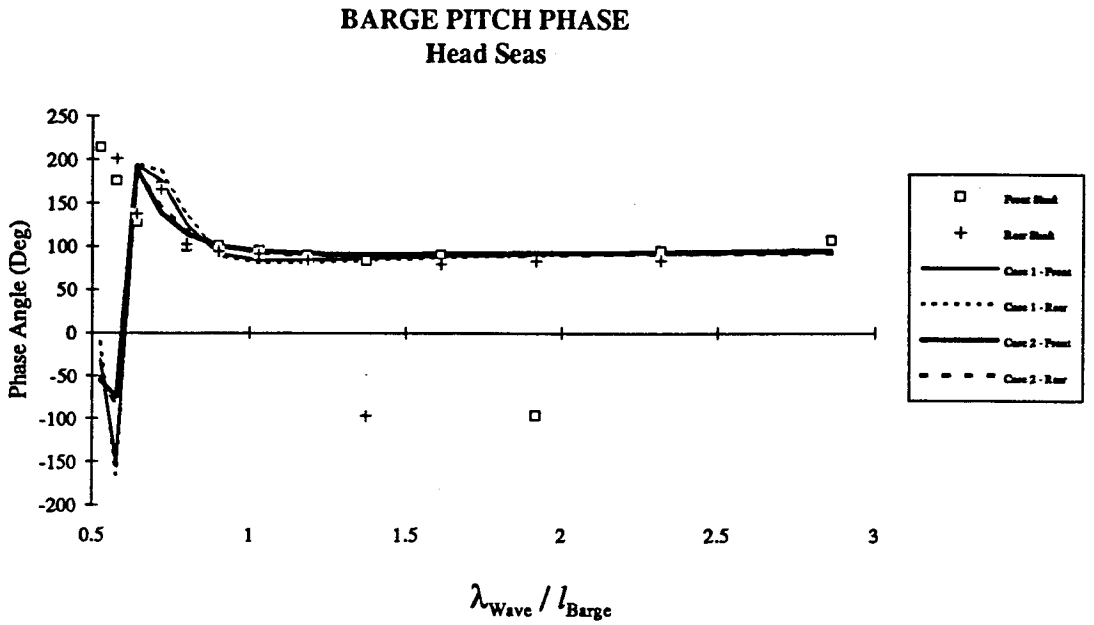

Graph 4.20 : Barge Pitch Phase in Head Seas

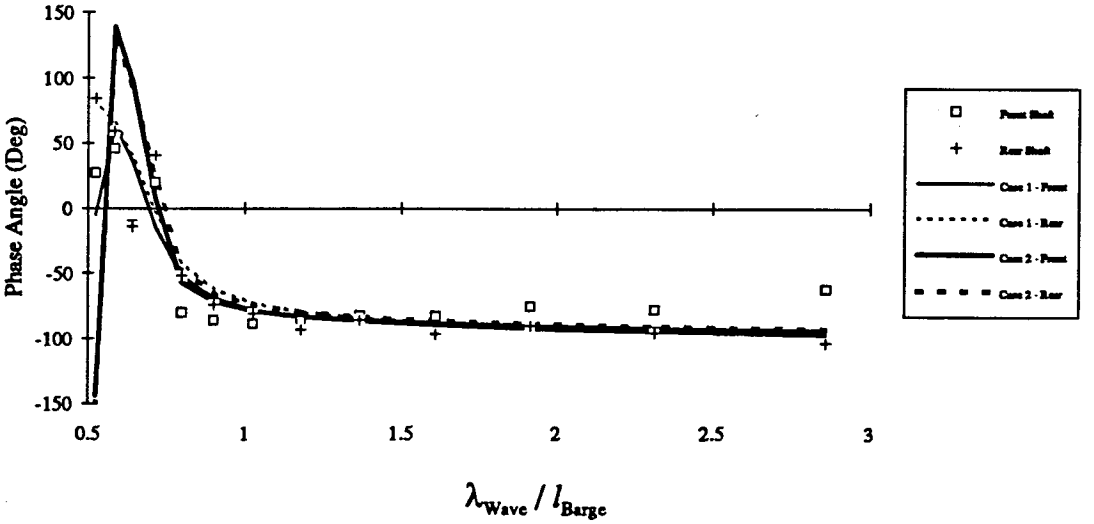

Graph 4.21 : Barge Pitch Phase in Stern Seas

4.5.3 Pivot Angle

The numerical pivot angle is obtained by subtracting the complex trim of the tug from the complex trim of the barge. The results for head seas are plotted in Graph 4.22 and for stern seas on graph 4.23. Both graphs reflect the increase in the pivot angle which occurs when the pivot location is moved rearward.

In head seas (Graph 4.22) the short wavelength results agree very well up to $\lambda \approx l_{Barge}$. At longer wavelengths both models underpredict the pivot angle with the coupled model (Case 1) producing a larger angle. Comparing the pivot angle to the barge trim in Section 4.4.3.2 suggests that the tug trim is considerably underpredicted in the Case 2 model. The numerical simplification of splitting the tug and barge at the barge stern adds the tug bow to the barge. This reduces the added mass and damping of the tug which reduces the calculated trim at longer wavelengths (due to the higher added mass at long wavelengths; see graph 4.4).

In stern seas (Graph 4.23) the Case 1 model again calculates a higher pivot angle than the Case 2 model although both still underpredict this angle. Neither model predicts the saddle point at $\lambda \approx 0.6 l_{Barge}$. The numerical models do show a steeper rise to the maximum pivot angle in stern seas but not as steep as the experimental results. The models do predict a slightly larger pivot angle in stern seas than in head seas in agreement with the experimental trend.

Both the Case 1 and Case 2 models predict the phase angles correctly. The results are plotted in graphs 4.24 for head seas and 4.25 for stern seas.

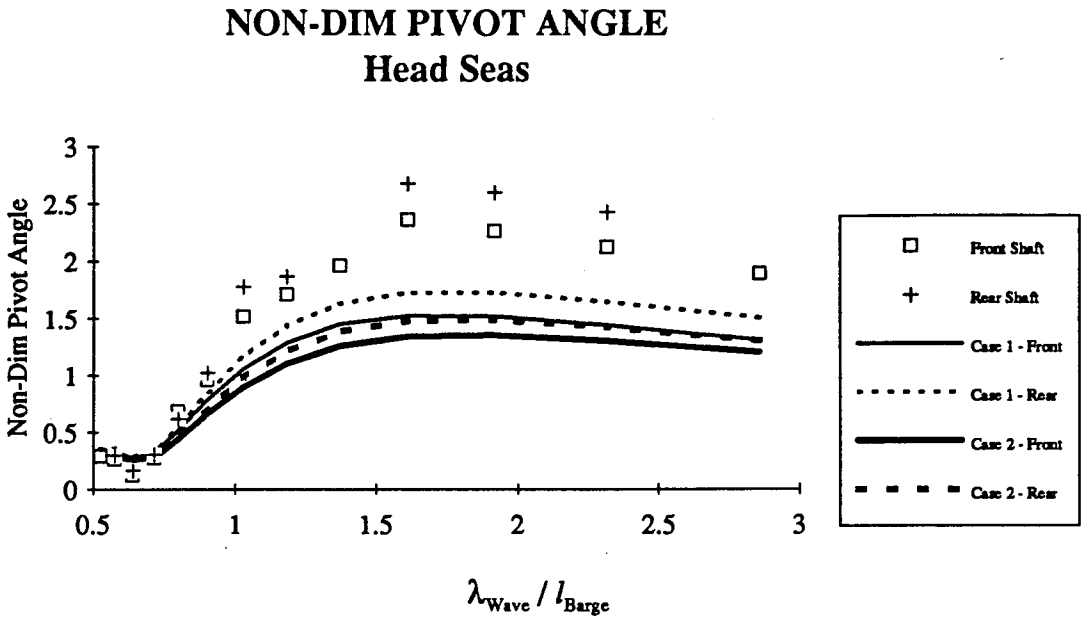

Graph 4.22 : Non-Dimensionalized Pivot Angle in Head Seas

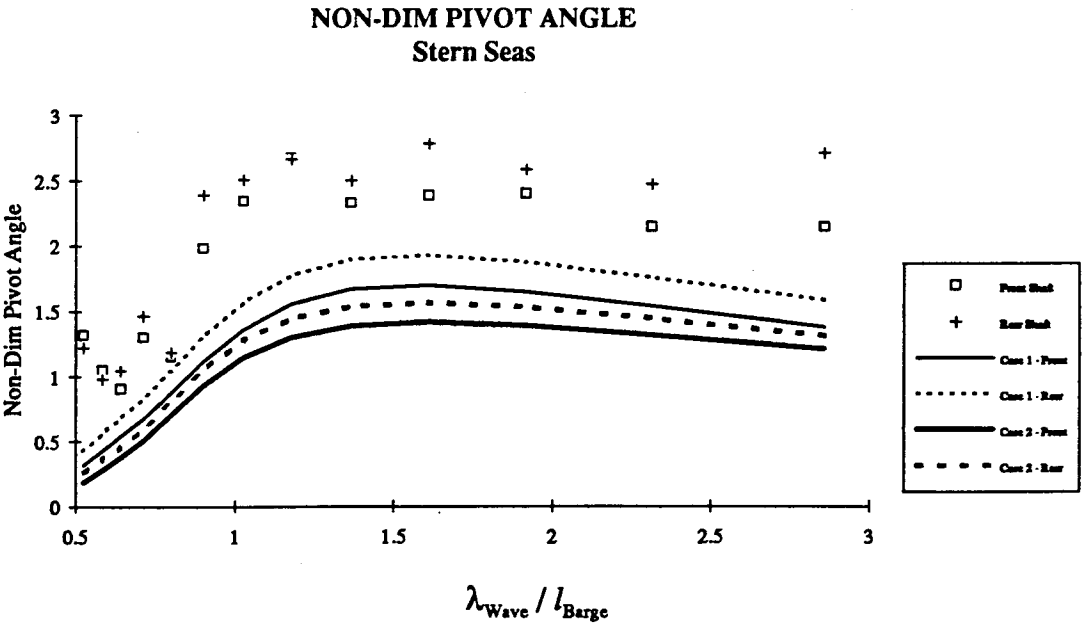

Graph 4.23 : Non-Dimensionalized Pivot Angle in Stern Seas

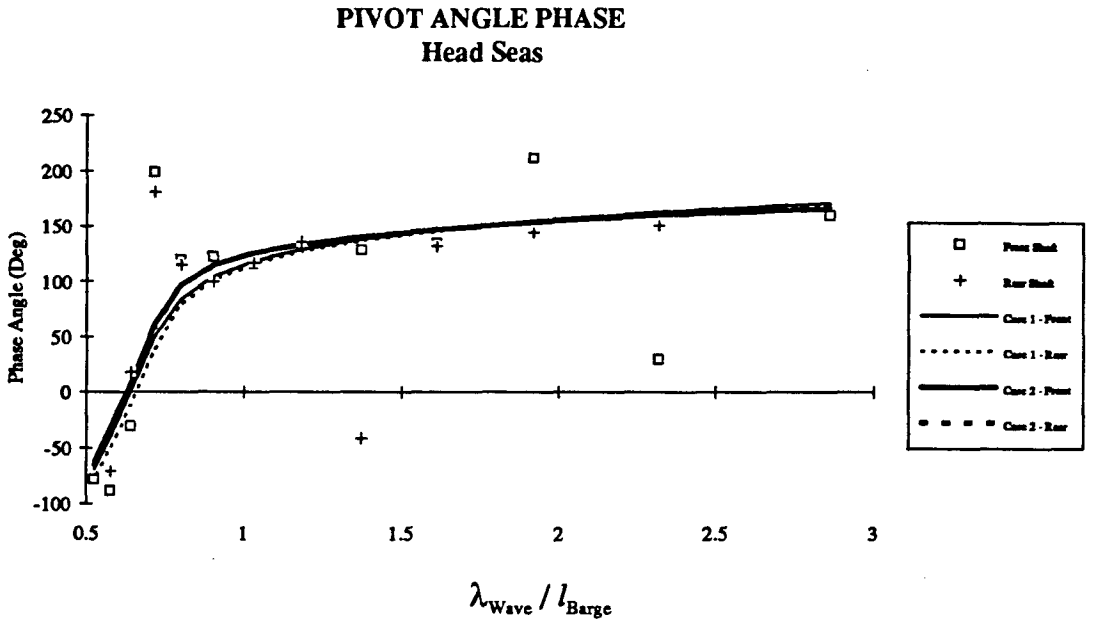

Graph 4.24 : Pivot Angle Phase in Head Seas

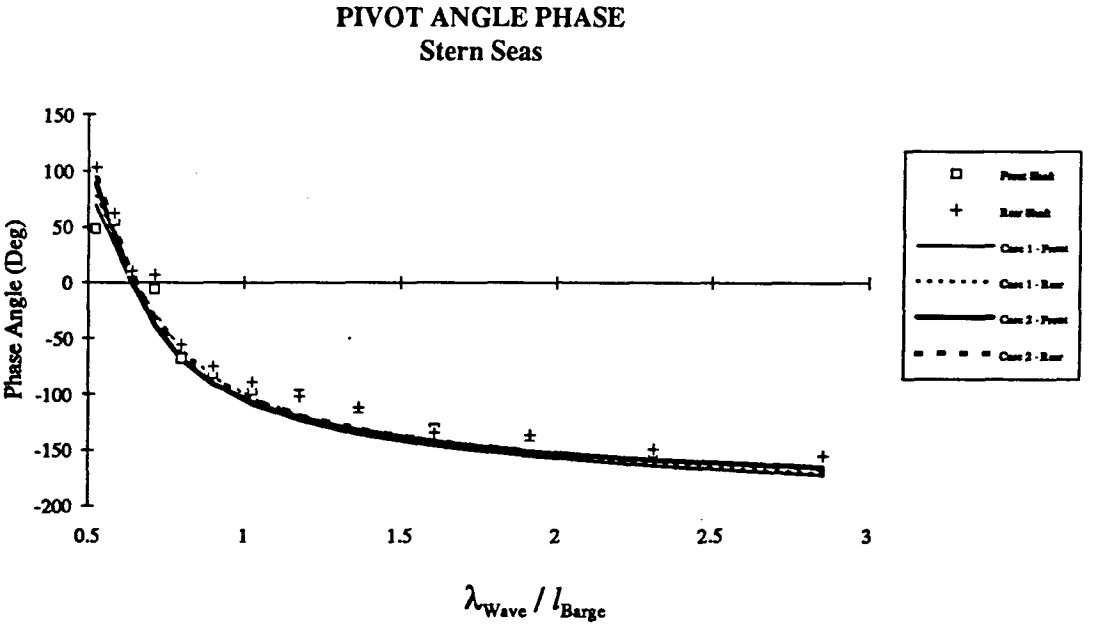

Graph 4.25 : Pivot Angle Phase in Stern Seas

4.5.4 Pin Force

The vertical force at the pivot location is plotted in Graph 4.26 for the head sea condition and Graph 4.27 for the stern sea condition. The effect of the change in pivot location is well represented by both numerical models in both sea conditions with the Case 2 model showing an improvement at shorter wavelengths. At the saddle point ($\lambda \approx 0.6 l_{Barge}$) the coupled model illustrates that the pivot location has less effect on the force calculation.

4.5.4.1 Head Seas

In head seas the Case 2 (coupled) model predicts the pin force well at wavelengths shorter than l_{Barge} and at wavelengths greater than $2l_{Barge}$. The saddle point at $\lambda \approx 0.6 l_{Barge}$ is well defined. The Case 2 model does not predict the magnitude of the peak force although the rear shaft location does peak close to the correct wavelength. The front shaft location shows almost no peak for the Case 2 model. The trend of the numerical pin force is similar to the experimental results; the lower pin force is reasonable since the hull motions are underpredicted in this wavelength regime.

The Case 1 model overpredicts the force at short wavelengths with the saddle point at $\lambda \approx 0.6 l_{Barge}$ occurring at a lower wavelength and a much higher force. As the wavelength increases the pin force decays more quickly for the Case 1 model than for the experimental results. As a result the Case 1 model underpredicts the force at longer wavelengths. The magnitude of the peak pin force is slightly larger than the experimental magnitude.

4.5.4.2 Stern Seas

The stern sea condition for the Case 2 model produces very similar results to the head sea condition. The saddle point at $\lambda \approx 0.6 l_{Barge}$ is again predicted; the Case 2 model calculates a slightly higher force than in head seas - this force is very close to the experimental force. The forces at short and long wavelengths are similar to the experimental results but the peak force is much lower than the experimental force. The peak force predicted by the Case 2 model in stern seas is slightly higher than in head seas. As in the head sea section these results are reasonable due to the underprediction of the hull motions.

The Case 1 model appears to predict the magnitude and trend of the force more accurately than the Case 2 model in stern seas. The front shaft results match the experimental forces at all wavelengths except close to $0.6 l_{Barge}$ where the saddle point is not predicted. The pin forces calculated for the rear pivot location miss the saddle point and are lower than the experimental forces at longer wavelengths.

4.5.4.3 Phase Angles

The phase difference is plotted in Graphs 4.28 and 4.29 (head and stern seas respectively). The Case 1 model reproduces the phase difference between the front and rear shaft locations as the wavelength increases. The Case 2 model does not predict this phase difference at longer wavelengths. At longer wavelengths the Case 1 model leads the experimental results slightly while the Case 2 model lags these results.

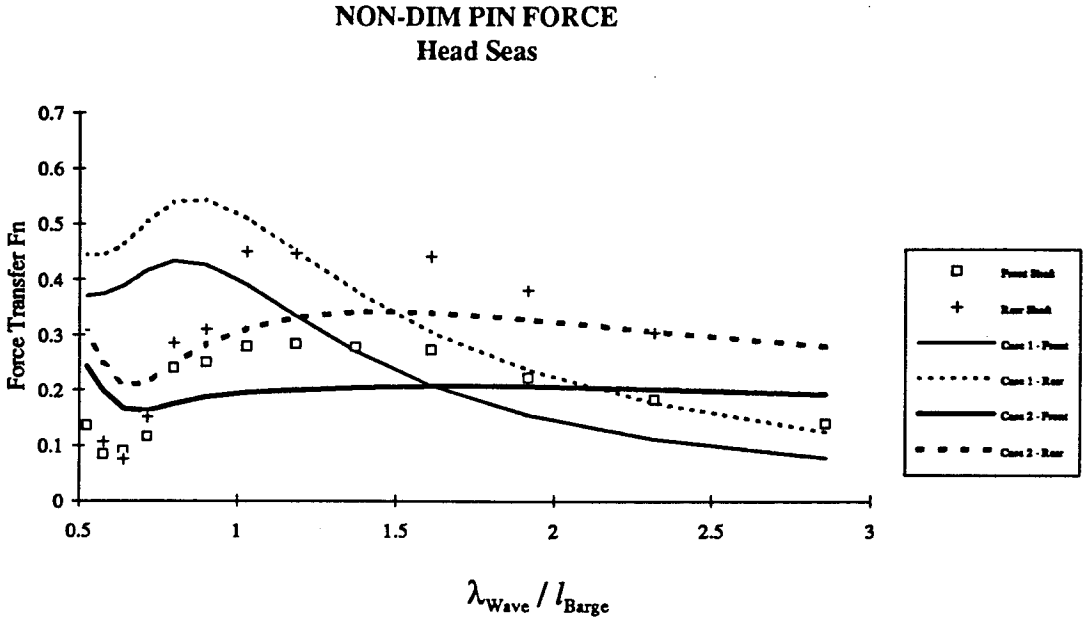

Graph 4.26 : Non-Dimensionalized Pin Force in Head Seas

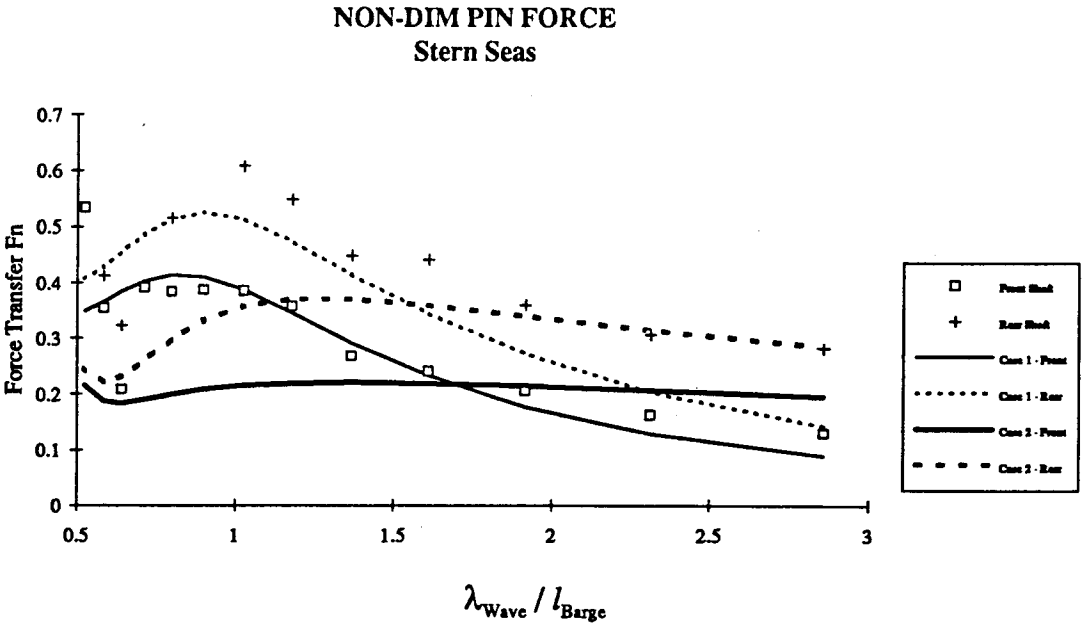

Graph 4.27 : Non-Dimensionalized Pin Force in Stern Seas

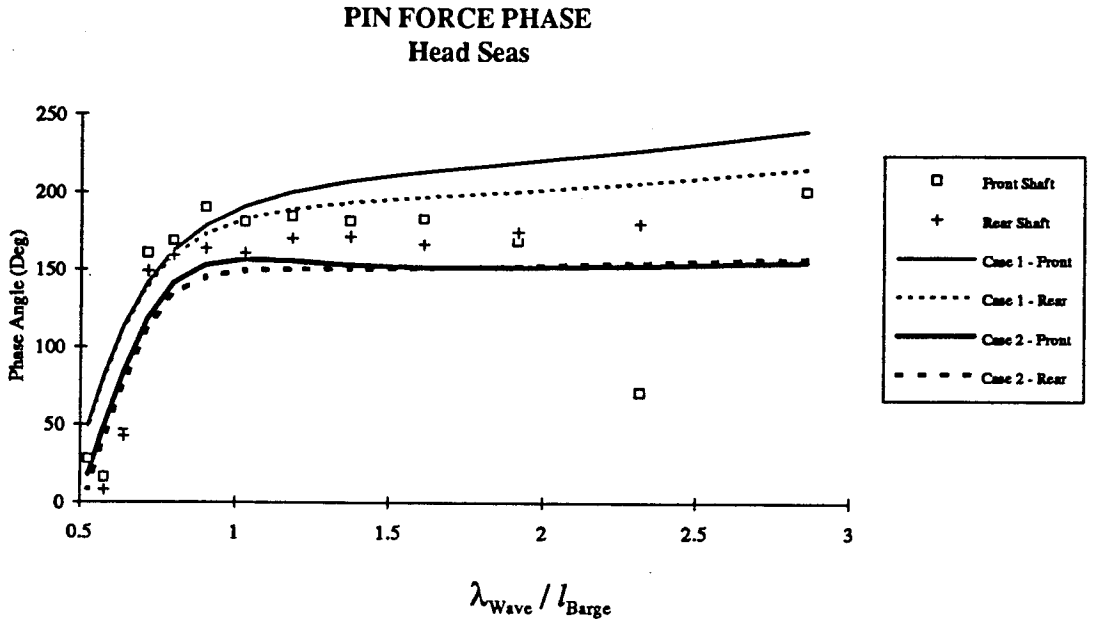

Graph 4.28 : Pin Force Phase in Head Seas

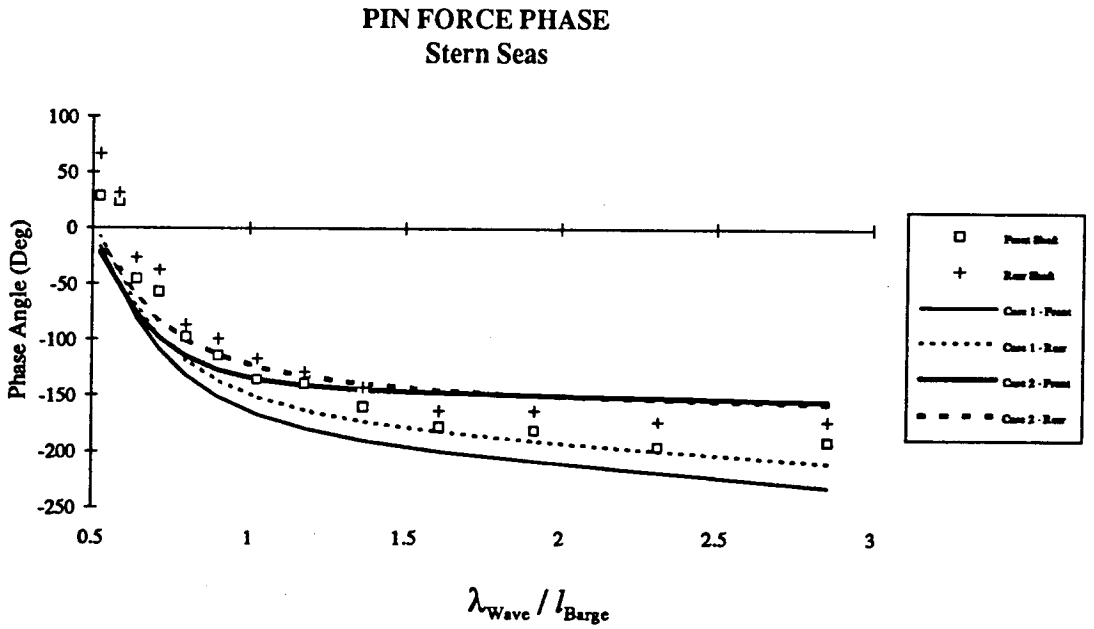

Graph 4.29 : Pin Force Phase in Stern Seas

4.6 Coupled Hydrodynamic Terms

The coupling terms for the added mass and damping predicted by the fully coupled (Case 2) model are contained in graphs 4.30 and 4.31 respectively. All terms are normalized using $a_{ij} = \frac{t_{ij}}{\sqrt{t_{ii} t_{jj}}}$ where t represents either the added mass or damping. The term 'cross-coupling' will be used to denote the terms referenced by the subscripts '13', '14', '23' and '24'. In the Case 1 model these are assumed to be zero. The '12' and '34' coupling terms represent the coupled heave-pitch terms for the tug and barge respectively. The Case 1 and Case 2 models produce similar results for these coupling terms with some minor differences due to the removal of the tug bow for the Case 2 model.

4.6.1 Added Mass

The added mass terms are shown in graph 4.30. The '12' terms and '34' terms are shown as solid lines while the terms coupling the tug and barge are shown as broken lines. The normalized tug-barge cross-coupling terms are of the same order of magnitude as the '12' and '34' terms. As the wavelength increases the tug heave-barge pitch (m_{14}) term becomes larger while the other three tug-barge coupling terms decrease towards the magnitude of the barge heave-pitch term. At short wavelengths the tug pitch-barge pitch (m_{24}) term is the most dominant of the cross-coupling terms. The barge heave-pitch terms do not vary much with the wavelength and are consistently small. The tug heave-pitch term (m_{12}) is also fairly constant with the wavelength. It is the largest coupling term; almost twice as large as the m_{14} term at long wavelengths.

4.6.2 Damping

The damping terms are plotted in graph 4.31. The tug heave-pitch term (c_{12}) is the largest coupling term while the barge heave-pitch term (c_{34}) is the smallest. Both of these terms remain relatively constant at all wavelengths. All four cross-coupling terms increase with the wavelength. At longer wavelengths the tug pitch-barge pitch (c_{24}) and tug heave-barge pitch terms (c_{14}) become the dominant terms approaching the magnitude of the c_{12} term.

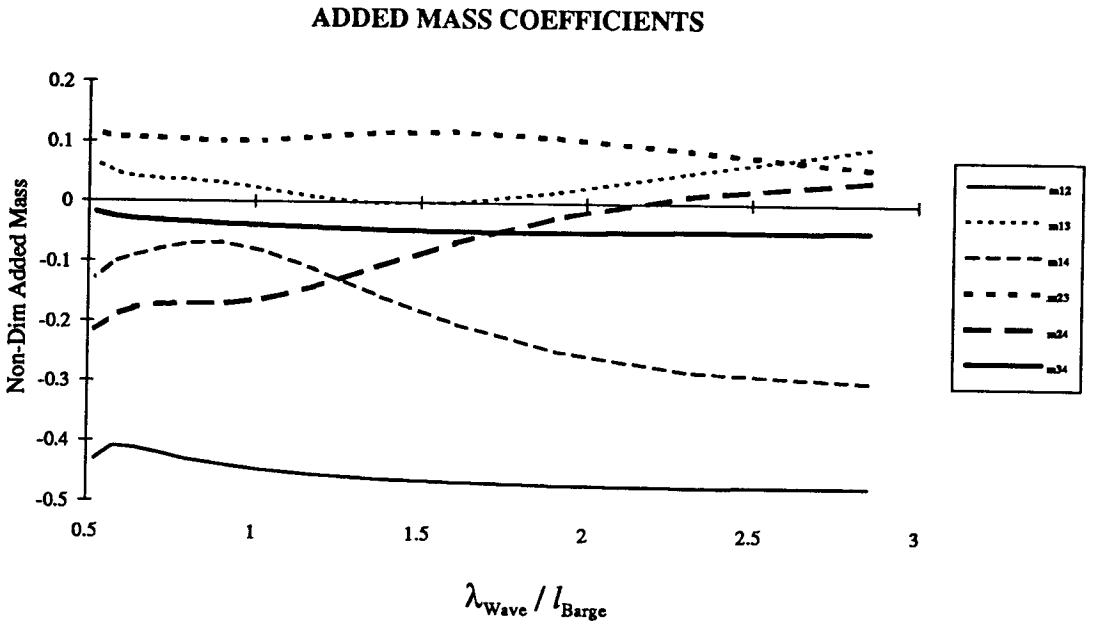

Graph 4.30 : Non-Dimensionalized Added Mass Terms

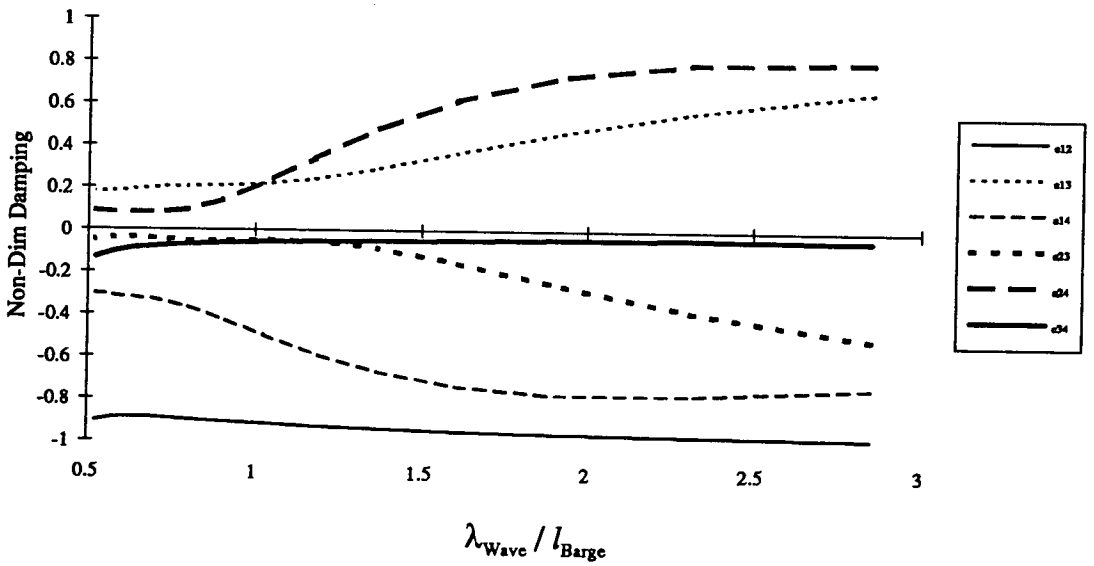

Graph 4.31 : Non-Dimensionalized Damping Terms

4.7 Discussion

The results of the two numerical models indicate that the motions of each hull are underestimated. This suggests that the unified slender body theory is not calculating the motions of the hulls accurately. The assumption of slenderness is inaccurate for both hulls; the length/beam ratios are 3.86 for the tug and 4.22 for the barge. The Case 2 hull is marginally better with a ratio of 5.2. The slenderness ratio for the unified theory should be greater than 10. Additionally the unified theory assumes a deep water approach to the problem while the experimental results may be slightly amplified by the tow tank walls.

Both the Case 1 (uncoupled) and Case 2 models produce similar results for the barge heave while the Case 1 model predicts a slightly larger barge trim than the Case 2 model. Numerically the two barge models are very similar. The numerical solution of the barge stern in Case 1 requires that the last section have a source strength of zero corresponding to a rounded stern; in Case 2 this last section is assigned to the tug. Additionally the barge has a much larger mass than the tug and dominates the motions. The smaller barge trim in Case 2 is probably due to the presence of the m_{14} and m_{24} cross-coupling terms.

The pivot angles are also underestimated by the numerical models. These angles represent the difference in the pitch of the tug and the pitch of the barge. The unified theory therefore appears to underpredict the tug motions as well. The smaller angles calculated by the Case 2 model result from the numerical simplification of the intersection between the tug and barge. The bow of the tug is removed and included as part of the barge. The resultant tug model is reduced by 20% in length (0.91 metres to

0.73 metres) due to the inclusion of its bow with the barge. This reduces the added mass and damping which has a direct effect on the tug motions.

In head seas the vertical pin forces are overestimated by the Case 1 model and underestimated by the Case 2 model. In stern seas the Case 1 model appears to be accurate at wavelengths greater than $0.6l_{Barge}$ while the Case 2 model is still too low. As the unified theory is calculating smaller motions than expected the pin force should also be correspondingly lower. This suggests that the coupled model is more accurate and that the cross-coupling terms are important. This is confirmed by graphs 4.30 and 4.31. The cross-coupling terms may even be overpredicted at the longer wavelengths as the Case 2 model overpredicts the forces in this region while the Case 1 model underpredicts the forces. The larger experimental forces in stern seas may be due to the bluff stern of the barge and the hydrodynamic excitation of the tug in direct seas. The Case 2 model is unable to predict the rapid section change at the intersection of the tug and barge and models this area as a smooth slope due to the use of Simpson's method to integrate along the hull. This discontinuity in the hull combined with the bluff face presented to the waves in stern seas means that the unified theory will be unable to accurately predict the pin forces in stern seas. The hydrodynamic forces at this junction appear to outweigh the advantages of including the coupling terms in stern seas.

4.8 Summary

The numerical solution to the full three-dimensional flow problem was encoded and tested successfully against known results. The hydrodynamic terms (added mass, damping and the excitation force) all agreed with the results of Newman and Sclavounos.

The tug-barge unit was built numerically using two different cases. Case 1 assumed no hydrodynamic interaction between the hulls while Case 2 assumed the two hulls affected the hydrodynamics of each other. These two cases were compared to the experimental results in Chapter 3.

The effect of altering the pivot locations posed no problem for either the Case 1 or the Case 2 models. Both models underestimated the vessel motions in head and stern sea conditions. The Case 2 model predicted even smaller motions for the tug due to the missing bow section. The peak pin forces were underestimated by the Case 2 model and overpredicted by the Case 1 model. The underpredicted pin force is more reasonable as the motions are underpredicted. The cross-coupling terms can therefore be considered as significant.

Chapter 5

Conclusions and Recommendations

5.1 Conclusions

5.1.1 Theoretical Results

A new approach was derived to calculate the pin forces on a pusher tug-barge unit where the tug and barge are free to pitch relative to each other. This method relied on either a separate solution for the hydrodynamic forces on each of the two hulls or a full solution for the tug-barge unit treated as one hull. Unified slender body theory, a three-dimensional solution method derived by Newman, was chosen for its speed and applicability to the numerical problem.

The main advantage of the unified theory is the interaction coefficient :

$$C_j = \frac{\frac{q_j}{n_j} - \sigma_{2D}}{\sigma_{2D} + \sigma_{2D}} \tag{2.29}$$

where C_j links the two and three-dimensional solutions. This coefficient allows the calculation of the off-diagonal terms in the hydrodynamic matrix. The off-diagonal added mass and damping term can thus be determined from the term $\int_L n_i \frac{q_j}{\sigma_{2D} + \sigma_{2D}} \left(2i\omega c_{22}^{2D}\right) dx$ while the excitation force term includes a similar factor for the force on the other hull.

The vertical forces on the connecting pin are determined by balancing the forces on each hull and then applying the constraint that the motion of the two hulls at the pin must be the same. The resulting formula for the pin force is

$$F_{Pin} = \frac{\{B\}^T\left(-\omega^2[M]+[HD]+[HS]\right)^{-1}\{F\}}{\{B\}^T\left(-\omega^2[M]+[HD]+[HS]\right)^{-1}\{B\}} \tag{2.45}$$

where $\{B\}$ is the constraint vector on the hull motion, [M] is the mass and inertia matrix, [HD] is the hydrodynamic matrix, [HS] is the hydrostatic matrix and {F} is the excitation force vector. The vector elements represent the linearized tug and barge motions. This formula is valid for the pin force regardless of the theory used to determine the hydrodynamic terms.

5.1.2 Experimental Results

The tug-barge model was tested in head and stern seas in the towing tank at B.C. Research. The barge heave and pitch motions and the relative angle of the tug were measured as well as the vertical and horizontal forces at the pivot locations. Two different pivot locations were used to determine the effect of shifting the connecting pin. The effect of altering the pivot location can be summarized as:

1. Moving the pivot location back towards the centre of gravity of the tug increases the relative pivot angle and the vertical pin forces.
2. The barge heave is unaffected by the location of the pivot. This can be attributed to the much greater mass of the barge.
3. The barge trim increases slightly at longer wavelengths when the pivot location is moved rearwards. This may be the combined effect of moving the

bearing system mass rearward and the altered moment of inertia due to the new axis of relative pitch for the tug.

4. The phase angle difference between the rear and front pivot locations for the vertical force corresponds approximately to the distance the pivot was moved.

The results in head and stern seas lead to the following conclusions:

1. The horizontal pin forces are non-linear. They are a combination of the drag on the aft hull (the tug in head seas) and the moment created by the surge of the hulls about the pivot.
2. The pivot angle peaks at a lower wavelength in stern seas than in head seas. The barge trim is virtually unaffected by the heading so the tug trim must be greater in stern seas. This is probably caused by the direct effect of the waves on the tug in stern seas as well as the wave action against the bluff stern of the barge. When the model is in a head sea condition the tug is sheltered by the greater beam of the barge.
3. The vertical pin force is affected more by the pivot angle than the heave and trim of the barge regardless of sea direction. Although the tug heave is not measured the tug motions are expected to affect the pin forces much more than the barge motions. This is due to the greater weight of the barge.
4. The peak vertical pin force occurs at $\lambda_{Wave} \approx 1.2 l_{Barge}$ in head seas and at $\lambda_{Wave} \approx l_{Barge}$ in stern seas. The peak forces are also larger in the stern sea condition. This agrees with conclusions 2 and 3.
5. The phase angles are unaffected by the change in sea direction as expected.

5.1.3 Numerical Results

Two models were compared with the experimental data; one model (Case 1) evaluated the two hulls separately (following previous work) while the other (Case 2) combined them as a single hinged hull. The numerical models replicate the experimental model as closely as possible.

1. The assumptions of linearity and of the independence of each mode are reasonable for both models.
2. The assumption of slenderness is not met by either the separate models or the combined hull model.
3. The numerical models both under-estimate the motions of the hulls. This may be due to the deep water assumption of the unified theory. Reflection off the tow tank walls may have increased the experimental motions of the models. Additionally the lack of slenderness of the hulls may also reduce the motion prediction. The relatively small size of the models suggests that viscous forces may have a minor effect.
4. The calculated magnitudes of the barge heave and trim are very similar for each model because the numerical barge models are very similar in each case.
5. The pivot angle is calculated more accurately by the Case 1 model at longer wavelengths. The Case 2 model is very poor in this wavelength regime indicating a poor prediction of tug pitch. This is caused by the missing bow section on the Case 2 tug model which thus decreases the added mass and damping as well as the excitation force.
6. The excitation force is similar in magnitude for the Case 1 and Case 2 models.

7. Both models predict the effect of altering the pivot location.
8. The peak pin force is under-predicted in both head and stern seas by the Case 2 (coupled hull) model. The lower forces are related to the lower motions calculated for the Case 2 model. At longer wavelengths the cross-coupling terms may be over-estimated resulting in the prediction of a higher pin force.
9. The pin force calculated by the Case 1 model is too high in head seas and close to the experimental results in stern seas. The Case 1 model does not predict well at short wavelengths. The small motions predicted by the Case 1 model should produce a lower pin force than the experimental results.
10. The cross-coupling terms are significant in magnitude especially at longer wavelengths. The pin forces at longer wavelengths are over-predicted by the Case 2 model and under-predicted by the Case 1 model. Therefore at long wavelengths the cross-coupling terms may be over-predicted.
11. The phase angles agree very well with the experimental results for the vessel motions. The pivot angle phase for the Case 2 model is inconsistent at longer wavelengths in head seas but is otherwise acceptable. The Case 1 model is consistently accurate.

The results suggest that the inclusion of the cross-coupling hydrodynamic terms in the Case 2 model is an improvement. The model suffers from certain simplifications due to the inclusion of the tug bow as part of the barge and to the smooth transition between tug and barge at the notch. The low pin forces predicted are acceptable when the low amplitudes of motion for each hull are considered.

5.2 Recommendations

1. Experimental results should be obtained for sea directions other than head or stern seas. These could be used to verify the numerical model in Chapter 4 which is able to accept different headings. The only term dependent on the incident wave direction is the excitation force and Sclavounos has shown that this can be accurately determined by unified slender body theory. Experimentally this would require a wave tank and a more sophisticated setup than was utilized for the towing tank experiments.
2. Experimental results should be obtained for different tug-barge mass ratios and for different length/beam ratios for further comparison of the hull motions and pin forces.
3. An improved numerical model of the coupling between the tug and barge needs to be developed. At present the program is unable to model the notch where the tug and barge are connected. The current method assigns the bow of the tug to the stern of the barge. This reduces the total hydrodynamic force on the tug which particularly affects the pin force and the tug motions. One possible improvement would be to develop factors which adjust the hydrodynamic forces on the tug and barge.
4. The discontinuity where the two hulls meet can be improved. This could be done by adding many more equally spaced stations to more closely define this area or by revising the numerical solution to the three-dimensional problem so that it uses a variable step size for the integration along the hull. The former

method will increase execution time considerably (as well as preparation time for the model) while the latter method will increase the coding complexity.

5. The existing model can be extended to work on the forward speed problem as the unified theory is capable of handling this.

Appendix A

Solution of Two-Dimensional Potential Flow

A.1 General

The potential flow problem around a two-dimensional body section is solved by locating two-dimensional pulsating sources around the hull. The numerical solution for a two-dimensional body section can be obtained by using numerous methods such as panelling or the Frank close-fit method. The method used here is to fit a continuous line of two-dimensional pulsating sources ϕ_S around the hull section and then determine the potential ϕ_{2D} by integrating ϕ_S over the hull section using some source strength distribution A_j. The source strength distribution is found by using least squares to minimize the error on the hull boundary condition.

A.2 Definition of Hull Shape

The two-dimensional hull section must be defined as a continuous curve so that a line of pulsating sources can be distributed on it. By using Gauss-Legendre integration around the hull section a set of N non-equally spaced points can be selected which adequately define the section. This also scales the range of integration from (x_1,x_2) down to (-1,1). For most hulls the shape is symmetrical about the centre-line; by choosing suitable boundary conditions only half the hull need be solved. This gives a full scale range of integration from $x_1 = 0$ to x_2 = beam.

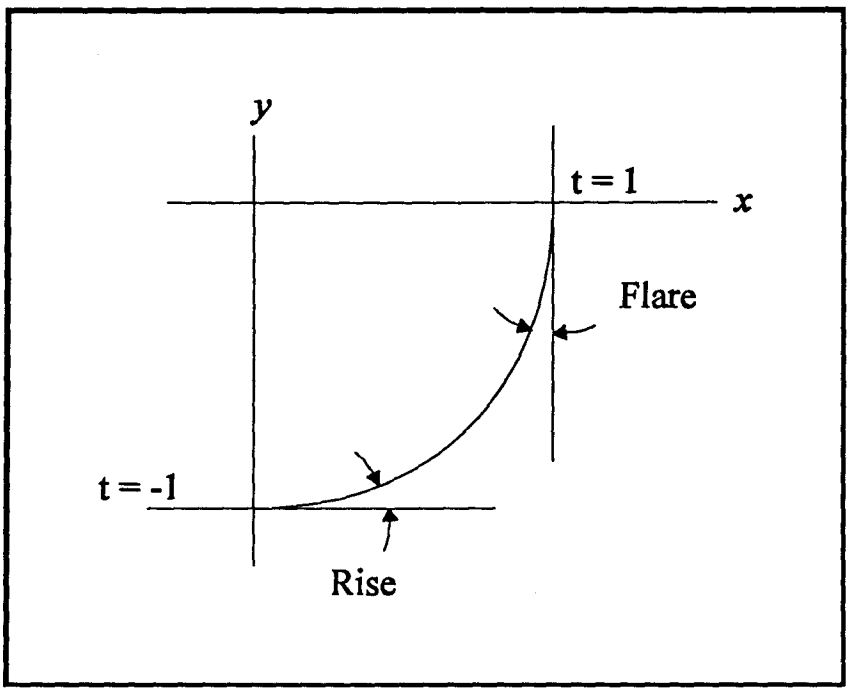

Figure A.1 Hull Shape

The hull shape can be defined by the end-points of the curve, the slope at each end and a weighting factor. Combining these with shape functions (to interpolate between points). the (x,y) values can be defined from t = -1 to t = 1. i.e. $x(t) = \sum_i X_i F_i$ and $y(t) = \sum_i Y_i F_i$. The X_i and Y_i terms can be defined as:

$X_1 = 0$ and $Y_1 = T$ where T is the draft (negative).

$X_2 = M_1\sqrt{(1-\text{Rise}^2)}$ and $Y_2 = (M_1 \cdot \text{Rise})$ where M_1 is the rise weighting factor.

$X_3 = B/2$ and $Y_3 = 0$ where B is the beam.

$X_4 = (M_2 \cdot \text{Flare})$ and $Y_4 = M_2\sqrt{(1-\text{Flare}^2)}$ where M_2 is the flare weighting factor

The shape functions can be defined as:

$F_1(t) = 0.5 - 0.75t + 0.25t^3$

$$F_2(t) = 0.25 - 0.25t - 0.25t^2 + 0.25t^3$$

$$F_3(t) = 0.5 + 0.75t - 0.25t^3$$

$$F_4(t) = -0.25 - 0.25t + 0.25t^2 + 0.25t^3$$

There are N elements on t so that the interpolation matrix $[F(t)]$ is a $4 \times N$ matrix and the $x(t)$ and $y(t)$ vectors have N elements each. The curve from t = -1 to t = 1 is defined as c. Figure A.1 details the parametrization of the hull section.

The second step in setting up the hull shape involves the definition of the normals and derivatives around the hull. Integration of a function of the hull $f(c)$ requires:

$$\int_C f(c)dc = \int_{-1}^{1} f(t)\frac{dc}{dt}dt \tag{A.1}$$

where $$\frac{dc}{dt} = \sqrt{\left(\frac{dx}{dt}\right)^2 + \left(\frac{dy}{dt}\right)^2} \tag{A.2}$$

and $$\frac{dx}{dt} = X_i F_i'(t), \quad \frac{dy}{dt} = Y_i F_i'(t) \tag{A.3}$$

i.e. $$\frac{dc}{dt} = \sqrt{\left(X_i F_i'(t)\right)^2 + \left(Y_i F_i'(t)\right)^2} \tag{A.2a}$$

Therefore using the Gauss-Legendre weighting functions for the integration gives

$$\int_C f(c)dc = \sum_i W_i f(t_i)\sqrt{\left(X_i F_i'(t_i)\right)^2 + \left(Y_i F_i'(t_i)\right)^2} \tag{A.4}$$

Finally the normals can be defined by :

$$N_x = \left(\frac{dy/dt}{dc/dt}\right) \text{ and } N_y = \left(\frac{-dx/dt}{dc/dt}\right) \tag{A.5}$$

With the hull shape fully defined the potential solution around the hull can be formulated.

A.3 Pulsating 2-D Source Derivation

The free surface boundary condition equates the pressure on the surface.

$$-\omega^2\phi + g\frac{\partial\phi}{\partial y} = 0\Big|_{y=y_f} \tag{A.6}$$

$$-\omega^2 \ln r + g\frac{d\phi}{dr}\frac{dr}{dy} = 0\Big|_{y=y_f} \tag{A.7}$$

$$-\omega^2 \ln r + g\frac{1}{r}\frac{(y-\eta)}{\sqrt{(x-\chi)^2+(y-\eta)^2}} \neq 0\Big|_{y=y_f} \tag{A.8}$$

$$\phi = \ln r - \ln r^* + \int_{-\infty}^{\infty} A(k)e^{|k|y}e^{-ikx}\,dk \tag{A.9}$$

where $r^* = \sqrt{(x-\chi)^2+(y+\eta-2y_f)^2}$ (A.10)

$$\phi = \frac{1}{2}\ln\left((x-\chi)^2+(y-\eta)^2\right) - \frac{1}{2}\ln\left((x-\chi)^2+(y+\eta-2y_f)^2\right) + \int_{-\infty}^{\infty} A(k)e^{|k|y-ikx}\,dk \tag{A.11}$$

This form of the potential satisfies Laplace and the free surface condition.

$$\frac{\partial\phi}{\partial y} = \frac{(y-\eta)}{(x-\chi)^2+(y-\eta)^2} - \frac{(y+\eta-2y_f)}{(x-\chi)^2+(y+\eta-2y_f)^2} + \int_{-\infty}^{\infty} A(k)|k|e^{|k|y-ikx}\,dk \tag{A.12}$$

On $y = y_f$:

$$\phi = \int_{-\infty}^{\infty} A(k)e^{|k|y_f-ikx}\,dk \tag{A.13}$$

and $$\frac{\partial\phi}{\partial y} = \frac{2(y_f-\eta)}{(x-\chi)^2+(y_f-\eta)^2} + \int_{-\infty}^{\infty} A(k)|k|e^{|k|y_f-ikx}\,dk \tag{A.14}$$

Using the free surface boundary condition (A.6) gives :

$$\int_{-\infty}^{\infty}\left(\frac{\omega^2}{g}-|k|\right)A(k)e^{|k|y_f-ikx}dk=\frac{2(y_f-\eta)}{(x-\chi)^2+(y_f-\eta)^2} \tag{A.15}$$

By applying a Fourier transform to equation (A.15) $A(k)$ can be solved so that the potential ϕ_S at each source is :

$$\phi_S=\frac{1}{2}\ln\left(\frac{(x-\chi)^2+(y-\eta)^2}{(x-\chi)^2+(y+\eta-2y_f)^2}\right)-\int_{-\infty}^{\infty}\frac{e^{|k|(y+\eta-2y_f)-ik(x-\chi)}}{|k|-\frac{\omega^2}{g}}dk \tag{A.16}$$

This can then be reduced using the method of residues for the integration of the complex analytic function. The final form of ϕ_S is therefore:

$$\begin{aligned}\phi_S=&\frac{1}{2}\ln\left(\frac{(x-\chi)^2+(y-\eta)^2}{(x-\chi)^2+(y+\eta-2y_f)^2}\right)+2\pi i e^{k(y+\eta-2y_f)-ik|x-\chi|}\\&+2\int_{-\infty}^{0}\frac{p\cos\left(p(y+\eta-2y_f)\right)+k\sin\left(p(y+\eta-2y_f)\right)}{p^2+k^2}e^{p|x-\chi|}dp\end{aligned} \tag{A.17}$$

A.4 Forced Motion of Hull Section

The two-dimensional potential ϕ_j is solved by integrating the pulsating source terms around the hull with a suitable source strength distribution $A_j(c)$. The source strength distribution is found using a least squares solution.

$$\phi_j(x,y)=\int_C A_j(c)\phi_S(x,y,\chi(c),\eta(c))dc \tag{A.18}$$

The hull boundary condition is :

$$\frac{d\phi_j}{dn}=i\omega n_j\Big|_{on\,C} \tag{A.19}$$

$$i\omega n_j = n_j \int_C A_j(c)\phi_{s,j}(x,y,\chi(c),\eta(c))dc \tag{A.20}$$

Define the error as the difference between these terms; i.e.

$$\text{error}(c) = n_i\left(\int_C A_\alpha(c)\phi_{s,i}(x,y,\chi(c),\eta(c))dc - i\omega\right) \tag{A.21}$$

The best possible solution is the one with the smallest $\overline{(\text{error})(\text{error})^*}$ where :

$$\overline{(\text{error})(\text{error})^*} = \frac{1}{c}\int_C \{\text{error}(c)\cdot\text{error}^*(c)\}dc$$

The solution of the forced motion problem reduces to :

1. defining a set of potential $A_j(c)$ solutions and
2. selecting the best member from that set.

The source strength distribution $A_j(c)$ can be described in terms of amplitudes A_k and the shape functions $F_k(c)$ defined in section A.1.1 : $A_j(c) = A_k F_k(c)$. The potential is therefore :

$$\phi_j(x,y) = A_k \int_C F_k(c)\phi_s(x,y,\chi(c),\eta(c))dc \tag{A.22}$$

The boundary condition on the normal velocity (equation A.19) applies everywhere on the hull surface. For some location $(x(g),y(g))$ the error is:

$$\text{error}(g) = n_i\left(A_k \int_C F_k(c)\phi_{s,j}(x(g),y(g),\chi(c),\eta(c))dc - i\omega\right) \tag{A.23}$$

Therefore :

$$\text{error}(g) = A_k G_k(g) - H(g) \tag{A.24}$$

where :

$$G_k(g) = n_j(g)\int_C F_k(c)\phi_{s,j}(x(g), y(g), \chi(c).\eta(c))dc \tag{A.25}$$

$$H(g) = i\omega n_j(g) \tag{A.26}$$

The mean square error is :

$$\overline{(\text{error})(\text{error})^*} = \int_g \{\text{error}(g)\cdot \text{error}^*(g)\}dg \tag{A.27}$$

$$\overline{(\text{error})(\text{error})^*} = \int_g (A_k G_k(g) - H(g))(A_l^* G_l^*(g) - H^*(g))dg \tag{A.28}$$

$$\begin{aligned}\overline{(\text{error})(\text{error})^*} = A_k A_l^* \int_g G_k(g)G_l^*(g)dg - A_k \int_g G_k(g)H^*(g)dg \\ -A_l^* \int_g G_l^*(g)H(g)dg + \int_g H(g)H^*(g)dg\end{aligned} \tag{A.29}$$

The minimum mean square error exists when :

$$\frac{\partial(\overline{\text{error}^2})}{\partial\{\text{Re}[A_i]\}} = \frac{\partial(\overline{\text{error}^2})}{\partial\{\text{Im}[A_i]\}} = 0 \tag{A.30}$$

This reduces to :

$$2\,\text{Re}\left\{A_k \int_g G_k(g)G_l^*(g)dg\right\} - 2\,\text{Re}\left\{\int_g G_l^*(g)H(g)dg\right\} = 0 \text{ and}$$

$$2\,\text{Im}\left\{A_k \int_g G_k(g)G_l^*(g)dg\right\} - 2\,\text{Im}\left\{\int_g G_l^*(g)H(g)dg\right\} = 0 \tag{A.31}$$

$$\text{i.e. } A_k \int_g G_k(g)G_l^*(g)dg = \int_g G_l^*(g)H(g)dg \tag{A.32}$$

$$A_k = \left(\int_g G_k(g) G_l^*(g) dg \right)^{-1} \int_g G_l^*(g) H(g) dg \tag{A.33}$$

Using symmetry and equation (A.18) the potential in mode j is :

$$\phi_j(x,y) = A_k \int_{-1}^{1} F_k(t) \left[\phi_S(x,y,\chi(t),\eta(t)) + \phi_S(x,y,-\chi(t),\eta(t)) \right] \frac{dc}{dt} dt \tag{A.34}$$

There is an integrable discontinuity in the natural log term in ϕ_S. This presents a numerical integration problem which can be avoided in the following way :

$$\begin{aligned} \phi_j(x,y) = {} & A_k \int_{-1}^{1} F_k(t) \left[\phi_S(x,y,\chi(t),\eta(t)) + \phi_S(x,y,-\chi(t),\eta(t)) \right] \frac{dc}{dt} dt \\ & - A_k \int_{-1}^{1} F_k(t_i) \left. \frac{dc}{dt} \right|_{t_i} \ln \left(\left. \frac{dc}{dt} \right|_{t_i} |t - t_i| \right) dt + A_k F_k(t_i) \left. \frac{dc}{dt} \right|_{t_i} \int_{-1}^{1} \ln \left(\left. \frac{dc}{dt} \right|_{t_i} |t - t_i| \right) dt \end{aligned} \tag{A.35}$$

The last integral is evaluated directly as :

$$A_k F_k(t_i) \left. \frac{dc}{dt} \right|_{t_i} \left((1+t_i) \ln \left(\left. \frac{dc}{dt} \right|_{t_i} (1+t_i) \right) + (1-t_i) \ln \left(\left. \frac{dc}{dt} \right|_{t_i} (1-t_i) \right) - 2 \right). \tag{A.36}$$

With this potential solved the two-dimensional added mass and damping terms can be easily obtained by integrating the pressure around the hull section.

$$-\omega^2 m_{ij} + i\omega c_{ij} = -i\omega\rho \int_C n_i \phi_j(x(c), y(c)) dc \tag{A.37}$$

Numerically integrating this term follows the form of equation (A.4).

A.5 Far-Field Wave Amplitude

The far-field amplitude represents the wave amplitude far from the hull and can be derived in terms of ϕ_j.

$$\lim_{x\to\infty}\phi_j = i\frac{g}{\omega}A_j e^{ky}e^{-ikx} \tag{A.38}$$

The potential ϕ_j was derived in equation (A.34) as a function of the source strength distribution and ϕ_s. The potential ϕ_s is defined in equation (A.17) and consists of a direct source term, a propagating wave term and an integral over the free surface. The direct source term and integral reduce to 0 for large x and ϕ_s for the far-field waves can be determined from the propagating wave term:

$$\phi_s = 2\pi i e^{k(y+\eta)}\left(e^{-ik(x-\chi)} + e^{-ik(x+\chi)}\right) \tag{A.39}$$

where x is much larger than χ . This can be written as:

$$\phi_s = 2\pi i e^{k\eta}\left(e^{ik\chi} + e^{-ik\chi}\right)e^{ky}e^{-ikx} \tag{A.40}$$

Therefore:

$$\phi_j = \sum_{t=-1}^{t=1} A_k w_i F_k(t_i)\left[2\pi i e^{k\eta}\left(e^{ik\chi} + e^{-ik\chi}\right)\right]e^{ky}e^{-ikx}\frac{dc}{dt} \tag{A.41}$$

and:

$$A_j = -i\frac{\omega}{g}\left(\lim_{\chi\to\infty}\phi_j\right)e^{-ky}e^{ikx} \tag{A.42}$$

For large x:

$$A_j = 2\pi\frac{\omega}{g}\left(\sum_{t=-1}^{t=1} A_k w_i F_k(t_i)e^{k\eta}\left(e^{ik\chi} + e^{-ik\chi}\right)\frac{dc}{dt}\right) \tag{A.43}$$

Note that F_k are the shape functions defined in section A.1 while w_j are the weighting functions for the Gauss-Legendre integration around the hull.

The three-dimensional solution uses the two-dimensional source strength σ_j. Newman (1978) relates this source strength to the far-field wave amplitude A_j by:

$$\sigma_j = 2g/\omega A_j$$

The σ_j values are computed for each hull station.

Appendix B

Numerical Solution of Three-Dimensional Potential Flow

B.1 Governing Equation

The governing equation for the three-dimensional solution is derived in Chapter 4 as:

$$q_j(x)-\left(\frac{\sigma_j+\bar{\sigma}_j}{2\pi i\bar{\sigma}_j}\right)L(q_j)=\sigma_j \tag{B.1}$$

where:

$$\begin{aligned} L(q_j)=&[\gamma+\pi i]q_j(x)+\tfrac{1}{2}\int_L \operatorname{sgn}(x-\xi)\ln(2k|x-\xi|)\frac{d}{d\xi}q_j(\xi)d\xi \\ &-\frac{\pi}{4}k\int_L\left[Y_0(k|x-\xi|)+H_0(k|x-\xi|)+2iJ_0(k|x-\xi|)\right]q_j(\xi)d\xi \end{aligned} \tag{B.2}$$

The $q_j(x)$ terms are the unknown three-dimensional source strengths which are distributed along the centreline of the hull. The numerical solution for the $q_j(x)$ terms assumes that there are an odd number (N) of equally spaced source strengths allowing a Simpson's integration along the hull. The integration of the three-dimensional source strength velocity in the first integral of (B.2) requires that one additional assumption be made: each end of the hull is assumed to be slender and therefore have a source strength of 0.

Equation (B.1) can be solved by putting it in the form $[A(x,\xi)]\{q_j(x)\}=\{\sigma_j(x)\}$ where $q_j(x)$ and $\sigma_j(x)$ can be reduced to $(N\text{-}2)\times 1$ vectors and $A(x,\xi)$ to a $(N\text{-}2)\times(N\text{-}2)$ matrix because of the zero end source terms. The only unknowns are the three-

dimensional source strengths $q_j(x)$ which can be solved using any matrix solver or inversion routine.

B.2 Solving Matrix Terms

By envisioning each term in equations (B.1) and (B.2) as matrices the overall matrix $A(x,\xi)$ can be developed. The initial $q_j(x)$ and $\left(\frac{\sigma_j+\overline{\sigma_j}}{2\pi i\overline{\sigma_j}}\right)$ terms can be treated as diagonal matrices but the $L(q_j(x))$ term is more complex. The γ term is the Euler constant (0.5772...). The Struve function H_0 and Bessel functions J_0 and Y_0 are described by Abramowitz and Stegun (1964); the Bessel functions are solved in "Numerical Recipes in C". The first integral along the hull, $\frac{1}{2}\int_L \mathrm{sgn}(x-\xi)\ln\left(2k|x-\xi|\right)\frac{d}{d\xi}q_j(\xi)d\xi$, involves an integrable singularity at $x = \xi$. This singularity evaluates to 0 so the integral can be calculated directly. The Bessel function Y_0 in the second integral also contains an integrable singularity at $x = \xi$. This must be evaluated in the following way

$$\begin{aligned}\frac{\pi}{4}\int_{L_1}^{L_2} Y_0\left(k|x-\xi|\right)q_j(\xi)d\xi = \frac{\pi}{4}\int_{L_1}^{L_2} Y_0\left(k|x-\xi|\right)q_j(\xi)d\xi \\ -\frac{1}{2}q_j(x)\int_{L_1}^{L_2}\left(\ln\left(\tfrac{k|x-\xi|}{2}\right)+\gamma\right)d\xi \\ +\frac{1}{2}q_j(x)\begin{bmatrix}(L_2-x)\ln\left(\frac{k}{2}(L_2-x)\right)+\\ (x-L_1)\ln\left(\frac{k}{2}(x-L_1)\right)+\\ (\gamma-1)(L_2-L_1)\end{bmatrix}\end{aligned} \qquad \text{(B.3)}$$

where the integrals are evaluated everywhere except at $x = \xi$.

The numerical form of each integral is obtained by multiplying the terms in each one by a second matrix containing the Simpson's weighting factors. The matrix in this form is $N \times N$ in size.

$$[S] = \frac{dx}{3}\begin{bmatrix} 1 & 4 & 2 & \cdots & 2 & 4 & 1 \\ \vdots & \vdots & \vdots & \vdots & \vdots & \vdots & \vdots \\ 1 & 4 & 2 & \cdots & 2 & 4 & 1 \end{bmatrix} \tag{B.4}$$

The dx term represents the step size between stations. As the end terms are zero this matrix can be reduced to a $(N\text{-}2)\times(N\text{-}2)$ matrix by deleting the border columns and rows.

The derivative term in the first integral is solved by using central differencing. The derivative of the source at each end of the hull is non-zero and is evaluated by assuming an extra term is extended beyond the hull limits. The central differencing term in general form is

$$\frac{d}{dx} f(x) = \frac{f(x+h) - f(x-h)}{2h} \tag{B.5}$$

where h is any step size. In matrix form for the first integral this can be written as:

$$\begin{Bmatrix} q_0' \\ q_1' \\ \vdots \\ q_{n-1}' \\ q_n' \end{Bmatrix} = \frac{1}{2\,dx}\begin{bmatrix} 2 & 0 & 0 & \cdots & 0 & 0 & 0 \\ -1 & 0 & 1 & \cdots & 0 & 0 & 0 \\ \vdots & \vdots & \vdots & \ddots & \vdots & \vdots & \vdots \\ 0 & 0 & 0 & \cdots & -1 & 0 & 1 \\ 0 & 0 & 0 & \cdots & 0 & 0 & -2 \end{bmatrix}\begin{Bmatrix} q_1 \\ q_2 \\ \vdots \\ q_{n-2} \\ q_{n-1} \end{Bmatrix} = [D]\begin{Bmatrix} q_1 \\ q_2 \\ \vdots \\ q_{n-2} \\ q_{n-1} \end{Bmatrix} \tag{B.6}$$

where the end diagonal terms account for the source velocity at the bow and stern of the hull. This matrix is $N\times(N\text{-}2)$ in size and is multiplied by the matrix for the first integral which is $(N\text{-}2)\times N$ in size.

By combining the matrices for each term a single matrix $[A(x,\xi)]$ can be determined. Solving $\left[A(x,\xi)\right]\left\{q_j(x)\right\}=\left\{\sigma_j(x)\right\}$ thus defines the three-dimensional source strengths $q_j(x)$.

Appendix C

Experimental Results

C.1 Head Seas

Experimental Data from Tug/Barge

Front Shaft Model - FFT Analysis combined with Std. Dev.

Model Leng	3.35 m		lbs		N
Barge Leng	2.7 m	Barge Weight =	411		1831.939
(at waterline)		Tug Weight =	23.5		104.746

Heading = 0 Deg

Frequency	Barge Trim (Deg)	Barge Heave (m)	Tug Trim (Deg)	Wave Probe (m)	Port Hor. Force (N)	Port Ver. Force (N)	Starboard Hor. Force (N)	Starboard Ver. Force (N)
0.44959	0.58951	0.01221	1.34578	0.01530	0.61182	0.77291	1.06275	0.67849
0.49932	0.72575	0.01170	1.97960	0.01624	1.21058	1.22096	0.40306	0.79408
0.54912	0.81461	0.00991	2.66455	0.01696	0.99656	1.41498	0.80710	1.14557
0.59895	1.01803	0.00787	3.44352	0.01763	1.35874	1.76614	0.64094	1.49788
0.64897	1.08626	0.00410	3.77498	0.01984	1.49989	1.93079	0.84243	1.81417
0.69883	0.94774	0.00682	3.88938	0.02016	1.23356	1.99997	1.16761	1.88108
0.74931	0.88345	0.00432	3.71984	0.01895	1.05623	1.89945	1.03673	1.69442
0.80073	0.64120	0.00391	2.39506	0.01692	0.98191	1.52429	0.89779	1.35391
0.85044	0.42650	0.00281	2.07846	0.01829	1.65540	1.69148	1.40980	1.28515
0.89843	0.34363	0.00847	0.84171	0.01655	1.32782	0.47905	1.06628	0.81723
0.95043	0.52794	0.00417	0.54038	0.02122	0.77533	0.69562	0.52292	0.60865
1.00082	0.47417	0.00248	1.67276	0.02780	0.92270	0.80666	0.73348	0.78554
1.04885	0.44385	0.00177	1.84980	0.02550	0.98306	1.19631	1.17135	1.15413

Wavelen	LamW / Blen	Heave / Probe	Non-Dim Angles Barge	Tug	Forces Hor	Ver
7.72	2.85966	0.79803	0.82643	1.88663		0.13982
6.26	2.31842	0.72048	0.77725	2.12008		0.18292
5.18	1.91694	0.58400	0.69051	2.25862		0.22250
4.35	1.61128	0.44667	0.69793	2.36078		0.27291
3.71	1.37245	0.20642	0.56346	1.95814	0.17397	0.27814
3.20	1.18359	0.33826	0.41738	1.71285	0.17557	0.28378
2.78	1.02949	0.22811	0.35990	1.51540	0.16276	0.27947
2.43	0.90153	0.23090	0.25625	0.95716		0.25073
2.16	0.79920	0.15369	0.13978	0.68119		0.23988
1.93	0.71612		0.11154	0.27321		0.11546
1.73	0.63990	0.19665	0.11942	0.12224		0.09061
1.56	0.57708	0.08913	0.07382	0.26043		0.08441
1.42	0.52544	0.06950	0.06858	0.28583	0.12450	0.13583

Phase angles :

Relative to Wave Probe at LCB

					Relative to Ch. 4				
					Port		Starboard		Avg.
	Barge	Barge	Tug	Wave	Hor.	Ver.	Hor.	Ver.	Ver.
Frequency	Trim	Heave	Trim	Probe	Force	Force	Force	Force	Force
(Hz)	(Deg)	(Deg)	(Deg)	(Deg)	(Deg)	(Deg)	(Deg)	(Deg)	(Deg)
0.450	108.15	-1.72	160.13	0.00	154.45	-167.50	-136.31	-150.65	200.9261
0.499	94.81	-128.42	29.96	0.00	59.99	65.16	78.74	76.72	70.93654
0.549	-96.62	3.48	212.33	0.00	-145.78	178.17	167.94	159.93	169.0493
0.599	91.38	-5.55	134.65	0.00	127.32	173.95	167.47	192.37	183.1588
0.649	84.34	20.81	128.48	0.00	88.00	171.49	167.12	191.49	181.4918
0.699	90.12	66.16	133.13	0.00	73.78	177.21	129.64	191.98	184.5927
0.749	95.64	70.53	116.09	0.00	70.49	173.90	90.89	187.45	180.6724
0.801	101.64	91.18	122.40	0.00	30.59	183.49	82.39	196.45	189.9682
0.850	100.19	142.36	119.20	0.00	84.42	153.85	-30.08	183.51	168.6819
0.898	170.19	128.11	199.21	0.00	-6.65	152.84	162.28	168.47	160.6572
0.950	127.98	118.89	-30.34	0.00	-68.60	32.07	37.01	55.29	43.67876
1.001	176.00	144.50	-88.31	0.00	-156.79	4.16	-176.23	27.84	16.001
1.049	214.20	-138.90	-78.55	0.00	-144.13	17.86	-124.38	37.89	27.87302

Averaged Forces and Percentage Difference

Horizontal Force:			Vertical Force:		
Ave.	% Diff		Ave.	% Diff	
0.83728	26.92777		0.72570	-6.50572	Y
0.80682	-50.04326		1.00752	-21.18479	
0.90183	-10.50423	Y	1.28027	-10.52152	Y
0.99984	-35.89583		1.63201	-8.21877	Y
1.17116	-28.06914		1.87248	-3.11416	Y
1.20058	-2.74655	Y	1.94052	-3.06330	Y
1.04648	-0.93146	Y	1.79694	-5.70502	Y
0.93985	-4.47474	Y	1.43910	-5.91979	Y
1.53260	-8.01227	Y	1.48832	-13.65099	
1.19705	-10.92443	Y	0.64814	26.08797	
0.64912	-19.44215		0.65213	-6.66762	Y
0.82809	-11.42511		0.79610	-1.32655	Y
1.07721	8.73955	Y	1.17522	-1.79446	Y

Experimental Data from Tug/Barge

Rear Shaft Model - Standard Deviations

				lbs		N
Model Length	3.35	m	Barge Weight	411		1831.9391
Barge Length (at waterline)	2.7	m	Tug Weight	23.5		104.74591

Heading = 0 Deg

Frequency	Barge Trim (Deg)	Barge Heave (m)	Tug Trim (Deg)	Wave Probe (m)	Port Hor. Force (N)	Port Ver. Force (N)	Starboard Hor. Force (N)	Starboard Ver. Force (N)
0.50055	0.9634393	0.0124134	2.5017676	0.017833	1.1460518	2.1841999	0.46132	1.5015454
0.551065	1.1205567	0.0111352	3.4048765	0.018692	1.1612117	2.7430385	0.6634673	2.0964981
0.60273	1.2681009	0.0084983	4.2817745	0.019065	1.4879799	3.2005723	0.7089543	2.5278843
0.65197	1.1897948	0.0046616	4.0790521	0.02221	1.3690079	3.2182091	0.4746214	2.8546247
0.699768	0.9727347	0.0058829	4.5246	0.021482	1.2898264	3.6300526	0.7792975	2.8850235
0.750727	0.8994304	0.0039126	4.3902239	0.018986	1.156645	3.1853214	0.8817956	2.6173696
0.802315	0.671475	0.0047369	2.8046411	0.018502	0.8812542	2.1657039	0.9646652	1.7326321
0.852546	0.3919808	0.0032006	2.0999949	0.020359	0.8648872	2.385347	1.7208509	1.5662699
0.900529	0.3583107	0.0072482	0.9834454	0.01724	0.6141872	0.8369881	0.352493	0.9291639
0.953852	0.5260528	0.0031281	0.9262272	0.026621	0.5082501	0.7200457	0.6384236	0.6440401
1.010107	0.4763185	0.0033113	2.1784287	0.030679	0.8776332	1.2127665	0.4750715	0.9931303

Wavelen	LamW / Blen	Heave / Probe	Non-Dim Angles Barge	Tug	Forces Hor	Ver
6.23	2.3070304	0.69609	0.934791	2.4273765	0.1328448	0.3046167
5.14	1.9034549	0.59572	0.855819	2.6004557	0.1438744	0.3815933
4.30	1.5911189	0.44575	0.7937448	2.6800993	0.1698373	0.4428468
3.67	1.3598563					
3.19	1.1804296	0.27385	0.4008862	1.8646909	0.1419595	0.4469897
2.77	1.0256146	0.20608	0.364401	1.7786834	0.1582404	0.4504522
2.42	0.897963	0.25602	0.2444167	1.0208885	0.1470438	0.310537
2.15	0.7952664	0.15721	0.1148371	0.6152274	0.1871892	0.2860692
1.92	0.7127756		0.1111058	0.3049489		0.1509884
1.72	0.6353108	0.11751	0.094157	0.1657833		0.0755214
1.53	0.5665177	0.10793	0.0659677	0.3017011		0.1059734

Phase angles :

Relative to Wave Probe at LCB

					Relative to Ch. 4				
					Port		Starboard		
	Barge	Barge	Tug	Wave	Hor.	Ver.	Hor.	Ver.	
Frequency	Trim	Heave	Trim	Probe	Force	Force	Force	Force	
(Hz)	(Deg)	(Deg)	(Deg)	(Deg)	(Deg)	(Deg)	(Deg)	(Deg)	
0.501	84.84	-3.87	150.80	0.00	-176.17	177.41	-169.61	182.78	180.09319
0.551	83.51	-5.21	144.48	0.00	159.15	170.37	179.28	179.17	174.77444
0.603	79.82	-6.50	132.00	0.00	110.99	159.48	-174.61	173.39	166.43288
0.652	-97.08	173.04	-41.46	0.00	108.81	167.20	163.74	176.13	171.66499
0.700	85.40	58.78	135.60	0.00	105.91	165.50	82.33	174.62	170.06312
0.751	91.77	60.52	117.01	0.00	74.24	156.63	67.97	164.47	160.55099
0.802	95.12	89.85	99.64	0.00	18.71	161.16	60.79	165.80	163.47818
0.853	102.93	145.91	115.38	0.00	114.24	155.12	3.65	163.92	159.52266
0.901	166.07	109.36	181.22	0.00	-9.51	146.71	90.95	151.60	149.15503
0.954	137.95	117.76	17.73	0.00	-189.30	61.47	-3.62	23.34	42.405615
1.010	201.99	161.08	-70.82	0.00	-139.79	1.81	-126.50	14.21	8.0110478

Averaged Forces and Percentage Difference

Horizontal Force:

Ave.	% Diff
0.8036859	-42.599467
0.9123395	-27.278464
1.0984671	-35.459666
0.9218147	-48.512271
1.0345619	-24.673677
1.0192203	-13.483318
0.9229597	4.5186738
1.2928691	33.103266
0.4833401	-27.071434
0.5733369	11.352269
0.6763524	-29.759761

Vertical Force:

Ave.	% Diff
1.8428726	-18.521479
2.4197683	-13.359551
2.8642283	-11.742919
3.0364169	-5.9870636
3.257538	-11.435463
2.9013455	-9.787732
1.949168	-11.109146
1.9758084	-20.727644
0.883076	5.2190161
0.6820429	-5.5719086
1.1029484	-9.9567741

C.2 *Stern Seas*

Experimental Data from Tug/Barge

Front Shaft Model - FFT Analysis combined with Std. Dev.

Model Length	3.35	m		lbs	N
Barge Length	2.7	m	Barge Weight =	411	1831.9391
(at waterline)			Tug Weight =	23.5	104.74591

Heading = 180 Deg

Frequency	Barge Trim (Deg)	Barge Heave (m)	Tug Trim (Deg)	Wave Probe (m)	Port Hor. Force (N)	Ver. Force (N)	Starboard Hor. Force (N)	Ver. Force (N)
0.449616	0.4626102	0.0111391	1.2118729	0.012099	0.3887102	0.5148362	0.7374031	0.5604195
0.499736	0.6224974	0.009713	1.6956236	0.013679	0.8948832	0.6885107	1.3251402	0.8309378
0.54933	0.7400409	0.0084929	2.3618037	0.014099	0.4241951	0.9642795	0.846004	1.0072295
0.599178	0.8378198	0.0068051	3.0322662	0.015315	1.6017512	1.3348131	0.6196792	1.1715608
0.650324	0.9251729	0.0025841	3.622702	0.015906	0.7333953	1.4967657	0.8315234	1.3955406
0.70054	0.7932563	0.0041811	4.1731182	0.013758	1.0532956	1.7547596	0.9931911	1.5883301
0.750594	0.692746	0.0027262	4.2366928	0.013886	0.8708075	1.8610593	1.2263853	1.7720412
0.801088	0.6111854	0.0025691	4.6648649	0.015891	1.2445541	2.1573609	0.8281826	2.0170784
0.850892	0.3624833	0.0019147	3.1904798	0.016495	1.6025706	2.2486703	0.4329898	2.0541874
0.900124	0.3148736	0.0071031	3.5726169	0.014714	1.1493906	1.9558351	1.306027	1.957846
0.949627	0.4636435	0.0026125	4.0271164	0.021393	0.8453171	1.5996498	0.8341152	1.428723
0.993704	0.3372434	0.0025553	4.2077815	0.017584	1.4762332	2.1888946	0.8173483	2.0442408
1.049316	0.4312366	0.001655	4.1424337	0.012363	1.5352732	2.3416667	1.6659119	2.1318116

Wavelen	LamW / Blen	Heave / Probe	Non-Dim Angles Barge	Tug	Forces Hor	Ver
7.72	2.859333	0.92066	0.8199583	2.1479966		0.130983
6.25	2.3145522	0.71006	0.7899716	2.1518071		0.1637135
5.17	1.9154976	0.60238	0.7540676	2.4065694		0.206093
4.35	1.6100395	0.44434	0.6605891	2.3908269		0.2412024
3.69	1.3667488	0.16246	0.5962274	2.334649	0.1450052	0.2680008
3.18	1.1778294	0.30390	0.509333	2.6794708	0.2192332	0.3581339
2.77	1.0259781	0.19633	0.3838806	2.3477355		0.3856142
2.43	0.9007158	0.16167	0.2598189	1.9830648		0.3871682
2.16	0.7983611	0.11608	0.1315819	1.1581487		0.3844655
1.93	0.7134172		0.1145013	1.2991537	0.2459503	0.3920193
1.73	0.6409766	0.12212	0.1041876	0.9049527		0.2086365
1.58	0.585375	0.14532	0.0842018	1.0505844		0.3548111
1.42	0.5249714	0.13387	0.1373373	1.3192546	0.3816275	0.5333032

Phase angles :

Relative to Wave Probe at LCB

					Relative to Ch. 4			
					Port		Starboard	
	Barge	Barge	Tug	Wave	Hor.	Ver.	Hor.	Ver.
Frequency (Hz)	Trim (Deg)	Heave (Deg)	Trim (Deg)	Probe (Deg)	Force (Deg)	Force (Deg)	Force (Deg)	Force (Deg)
0.450	-62.003	-0.046	-155.533	0.000	-163.383	176.047	142.609	161.732
0.500	-77.909	-8.580	-152.837	0.000	57.174	153.393	-155.999	174.962
0.549	-75.460	-0.195	-138.251	0.000	-147.796	177.724	-158.761	179.294
0.599	-83.039	-0.644	-130.806	0.000	-125.505	-171.026	96.139	-184.755
0.650	-82.012	21.272	-112.922	0.000	-98.896	-161.423	-89.068	-159.132
0.701	-86.561	52.182	-100.439	0.000	-85.107	-142.139	-65.470	-137.813
0.751	-88.789	46.891	-97.136	0.000	-58.182	-139.329	-64.819	-133.021
0.801	-85.992	91.753	-81.990	0.000	-52.036	-117.520	-47.660	-111.812
0.851	-80.080	180.811	-68.201	0.000	5.066	-96.111	-159.517	-99.200
0.900	19.835	142.579	-5.845	0.000	96.089	-61.899	85.040	-52.640
0.950	-12.962	163.563	8.946	0.000	64.512	-48.048	113.182	-43.784
0.994	45.758	194.093	55.982	0.000	129.854	22.545	-141.716	24.153
1.049	27.147	-70.880	48.515	0.000	-114.954	16.664	164.032	39.483

Averaged Forces and Percentage Difference

Horizontal Force:		Vertical Force:	
Ave.	% Diff	Ave.	% Diff
0.5630566	30.96428	0.5376279	4.2393028
1.1100117	19.380739	0.7597243	9.3736079
0.6350995	33.208101	0.9857545	2.1785327
1.1107152	-44.208992	1.2531869	-6.5134859
0.7824594	6.2704956	1.4461532	-3.4998062
1.0232433	-2.93696	1.6715448	-4.9783138
1.0485964	16.954941	1.8165503	-2.4501965
1.0363683	-20.088009	2.0872196	-3.3605117
1.0177802	-57.457439	2.1514289	-4.5198543
1.2277088	6.3792161	1.9568405	0.0513806
0.8397161	-0.6670058	1.5141864	-5.6441782
1.1467907	-28.727335	2.1165677	-3.4171785
1.6005925	4.0809459	2.2367391	-4.6910939

Experimental Data from Tug/Barge

Rear Shaft Model - Standard Deviations

Model Length	3.35 m		lbs		N
Barge Length	2.7 m	Barge Weight =	411		1831.9391
(at waterline)		Tug Weight =	23.5		104.74591

Heading = 180 Deg

Frequency	Barge Trim (Deg)	Barge Heave (m)	Tug Trim (Deg)	Wave Probe (m)	Port Hor. Force (N)	Ver. Force (N)	Starboard Hor. Force (N)	Ver. Force (N)
0.452809	0.4638454	0.0093503	1.2251013	0.009555	0.2795857	0.9100883	0.9558203	0.9233558
0.499824	0.5712191	0.0078847	1.5624223	0.010939	0.5949157	1.1698848	0.8354185	1.1053667
0.550661	0.6382316	0.006404	1.9986744	0.011036	0.5129112	1.4636289	0.5931719	1.2437071
0.598638	0.697287	0.0050086	2.5928778	0.011258	0.9624569	1.7771752	0.8921744	1.6054872
0.650333	0.7396844	0.0023452	3.071852	0.012554	1.009707	2.1690608	0.148421	1.6611009
0.698746	0.542904	0.0052757	3.4269167	0.011405	1.1157106	2.3736099	0.4576474	1.8712624
0.750993	0.5168169	0.0042893	3.7004456	0.01133	0.821578	2.5237991	0.7138695	2.1549223
0.799099	0.4622669	0.0025977	4.2447395	0.012046	1.1715972	2.8657808	0.455776	2.4008124
0.850146	0.202223	0.0018886	2.5777012	0.013003	1.1030857	2.4654907	0.2701078	2.0889012
0.901127	0.2956158	0.0055677	3.299572	0.012046	1.1923669	2.2933301	0.3269703	2.1289358
0.95081	0.3943181	0.0027711	3.7034829	0.016972	0.8275693	2.0902678	0.7173988	1.6264238
0.997911	0.2564683	0.0016785	3.5917902	0.015923	0.9131255	2.3817961	0.5732007	2.0767584
1.045919	0.3022121	0.0013182	3.2501621	0.010528	1.0716305	2.4978122	0.8801282	2.2054084

Wavelen	LamW / Blen	Heave / Probe	Non-Dim Angles Barge	Tug	Forces Hor	Ver
7.61	2.8191498	0.97858	1.0264127	2.7109451		0.2828067
6.25	2.3137373	0.72078	0.9061507	2.4785411	0.1927137	0.3065523
5.15	1.906249	0.58028	0.8268134	2.5892337	0.1477164	0.3615624
4.35	1.6129455	0.44489	0.7492578	2.7861325	0.2428002	0.4428434
3.69	1.3667109	0.18681	0.6039518	2.508165		0.4496636
3.20	1.1838852	0.46257	0.4226673	2.6679587		0.5485574
2.77	1.0248882	0.37858	0.3506263	2.5105094	0.1997367	0.6086253
2.44	0.9052053	0.21565	0.2605303	2.3923049		
2.16	0.7997628	0.14525	0.0932845	1.1890812		0.5162256
1.92	0.7118299		0.1310154	1.4623532	0.1858934	
1.73	0.6393825		0.111413	1.0464039	0.134165	0.3227574
1.57	0.5804498		0.0701188	0.9820011	0.1375758	0.4126881
1.43	0.528387		0.1137573	1.2234115	0.2732329	

Phase angles :

Relative to Wave Probe at LCB

					Relative to Ch. 4				
					Port		Starboard		Avg.
	Barge	Barge	Tug	Wave	Hor.	Ver.	Hor.	Ver.	Ver.
Frequency (Hz)	Trim (Deg)	Heave (Deg)	Trim (Deg)	Probe (Deg)	Force (Deg)	Force (Deg)	Force (Deg)	Force (Deg)	Force (Deg)
0.453	-103.377	-1.053	-155.298	0.000	-54.313	-163.591	151.315	-181.446	-172.519
0.500	-95.397	-6.716	-149.408	0.000	68.448	-174.465	-168.705	-171.296	-172.880
0.551	-90.089	-1.331	-136.815	0.000	-147.543	-162.246	169.038	-164.698	-163.472
0.599	-96.486	-7.332	-134.575	0.000	-98.318	-157.328	150.190	-169.610	-163.469
0.650	-85.778	-15.188	-111.522	0.000	-114.795	-143.902	-62.871	-141.258	-142.580
0.699	-92.893	-4.423	-101.803	0.000	-89.277	-130.561	-54.197	-126.891	-128.726
0.751	-80.715	62.598	-88.960	0.000	-62.059	-121.265	-51.098	-113.062	-117.164
0.799	-73.915	99.014	-74.909	0.000	-51.029	-102.640	-28.001	-95.691	-99.166
0.850	-51.961	160.865	-55.539	0.000	1.509	-87.583	139.281	-85.840	-86.711
0.901	40.562	152.481	7.022	0.000	69.499	-39.631	73.199	-34.941	-37.286
0.951	-14.008	168.193	10.617	0.000	35.951	-31.447	117.899	-21.315	-26.381
0.998	59.211	189.454	62.627	0.000	132.864	28.078	-158.075	35.231	31.654
1.046	84.298	186.530	103.433	0.000	-136.167	58.515	-149.459	74.525	66.520

Averaged Forces and Percentage Difference

Horizontal Force:

Ave.	% Diff
0.617703	54.737847
0.7151671	16.81445
0.5530416	7.256297
0.9273156	-3.7895698
0.579064	-74.368815
0.786679	-41.825393
0.7677238	-7.0147893
0.8136866	-43.986298
0.6865968	-60.659905
0.7596686	-56.958827
0.7724841	-7.1309217
0.7431631	-22.870133
0.9758794	-9.8117811

Vertical Force:

Ave.	% Diff
0.916722	0.7236387
1.1376257	-2.8356479
1.353668	-8.12318
1.6913312	-5.0755289
1.9150808	-13.2621
2.1224362	-11.834219
2.3393607	-7.8841376
2.6332966	-8.8286369
2.277196	-8.26871
2.2111329	-3.7174223
1.8583458	-12.480024
2.2292772	-6.8416261
2.3516103	-6.2170985

C.3 Calculation of Tank Natural Frequencies

The tow tank is 12 feet or 3.6576 metres wide. The natural frequency of the tank can be calculated by using this width as a transverse wavelength. The wavelength is defined by

$$\lambda = 2\pi/k = 2\pi g/\omega^2 \qquad \text{(C.1)}$$

The natural frequency can then be written as

$$\omega = \sqrt{2\pi g/\lambda}$$

Equation (C.2) produces the following natural frequencies:

λ = 3.6576 ω = 4.104 rads/sec ω = 0.653 Hz

λ = 1.8288 ω = 5.804 rads/sec ω = 0.924 Hz

Bibliography

------. 1979. Linkage System for Ocean-Going Tug-Barges. National Ocean-Going Tug-Barge Planning Conference.

Arcos, M.D. 1980. Integrated Tug-Barge Combinations. The Motor Ship, 67-74.

Bhattacharyya, R. 1978. Dynamics of Marine Vehicles. New York:Wiley-Interscience Publication.

Bougis, J. and P. Valier. 1981. Forces and Moments in the Rigid Connections Between a Barge and its Tug with Forward Speed in Wave. Proceedings of the Third International Conference on Numerical Ship Hydrodynamics, 517-531.

Boutan, C. and J-P. Colin. Coastal and Ocean-Going Tug/Barges. The Sixth International Tug Convention, 71-76.

Brady, E.M. 1967. Tugs, Towboats and Towing. Cambridge: Cornell Maritime Press Inc.

Brown, D.L. 1977. Computer Program for the Analytical Assessment of Flexibly Connected Barge Trains. Vol.1 & 2, MARAD Report.

Filson, J.J. 1972. Advanced Ocean Tug-Barge System: A Program for Evaluating Ocean Going Connected Tug-Barge. Galveston, Texas:National Maritime Research Center.

Fletcher, E.H. 1976. Artubar-What it is All About. The Fourth International Tug Convention, 183-195.

Glosten, L.R. 1967. SEA-LINK. Paper for Presentation to the Pacific Northwest Section of SNAME.

Glosten, L.R. 1972. A Tug/Barge Transportation System. The Second International Tug Convention, D7.1-D7.11.

Heuser, H.H. 1970. Push-Towing on German Inland Waterways. The First International Tug Convention, 361-366.

Heuser, H.H. 1976. Further Development in Push Towing Systems Stimulated and Prepared by Model Testing and Full Scale Measurements. The Fourth International Tug Convention, 167-182.

Heuser, H.H. 1982. Push-Tows for Inland Waterways - How to Reduce their Energy Requirement. The Seventh International Tug Convention, 87-100.

Jones, R.M. and C.S. Smith. Large Seagoing Unmanned Barge/Tug Developments. (Unknown Date and Publisher)

Keuning, J.A. and W. Beukelman. 1979. Hydrodynamic Coefficients of Rectangular Barges in Shallow Water. Proceedings of the Second International Conference on the Behaviour of Offshore Structures, Paper 55, 105-124.

Loukakis, T.A. and P.D. Sclavounos. 1978. Some Extensions of the Classical Approach to Strip Theory of Ship Motions, Including the Calculation of Mean Added Forces and Moments. Journal of Ship Research, 22:1, 1-19.

Mays, J.H. 1978. Wave Radiation and Diffraction by a Floating Slender Body. Cambridge, Massachusetts:Ph.D. Thesis, Massachusetts Institute of Technology.

Mineyev, V. 1988. Optimization of Push-Tow Sizes. The Permanent International Association of Navigation Congresses, 62, 111-118.

Newman, J.N. 1959. The Damping and Wave Resistance of a Pitching and Heaving Ship. Journal of Ship Research, 3:1, 1-19.

Newman, J.N. 1961. A Linearized Theory for the Motion of a Thin Ship in Regular Waves. Journal of Ship Research, 5:1, 34-55.

Newman, J.N. 1964. A Slender-Body Theory for Ship Oscillations in Waves. Journal of Fluid Mechanics, 18, 602-618.

Newman, J.N. 1967. The Drift Force and Moment on Ships in Waves. Journal of Ship Research, 11:1, 51-60.

Newman, J.N. 1975. Interaction of Waves with Two-Dimensional Obstacles: a Relation between the Radiation and Scattering Problems. Journal of Fluid Mechanics, 71, 273-282.

Newman, J.N. 1978. The Interaction of Stationary Vessels with Regular Waves. Eleventh Symposium of Naval Hydrodynamics.

Newman, J.N. 1978. The Theory of Ship Motions. Advances in Applied Mechanics, 18, 221-283.

Newman, J.N. and P.D. Sclavounos. 1980. The Unified Theory of Ship Motions. Thirteenth Symposium of Naval Hydrodynamics.

Newman, J.N. The Exciting Forces on Fixed Bodies in Waves. Journal of Ship Research, 6:3, 10-17.

Robinson, J.H. 1976. Experimental Research Relative to Improving the Hydrodynamic Performance of Ocean-Going Tug/Barge System. Bethesda, MD:David W. Taylor Naval Ship Research and Development Center.

Rossignol, G.A. 1974. Experimental Research Relative to Improving the Hydrodynamic Performance of Ocean-Going Tug/Barge System. Bethesda, MD:David W. Taylor Naval Ship Research and Development Center.

Rossignol, G.A. 1975. Experimental Evaluation of the Seaworthiness Characteristics of Flexibly Connected Barge Trains. Bethesda, MD:David W. Taylor Naval Ship Research and Development Center.

Rossignol, G.A. 1975. Experimental Research Relative to Improving the Hydrodynamic Performance of Ocean-Going Tug/Barge System. Bethesda, MD:David W. Taylor Naval Ship Research and Development Center.

Salvessen, N., E.O. Tuck and O. Faltinsen. 1970. Ship Motions and Sea Loads. SNAME Transactions, 78, 250-287.

Schmitke, R.T. 1978. Ship Sway, Roll and Yaw Motions in Oblique Seas. SNAME Transactions, 86, 26-46.

Sclavounos, P.D. 1981. The Interaction of an Incident Wave Field with a Floating Slender Body at Zero Speed. Proceedings of the Third International Conference on Numerical Ship Hydrodynamics, 481-498.

Stockdale, G. 1970. Development of Hinged and Articulated Ships. The First International Tug Convention, 369-385.

Stockdale, G. 1972. Economic Advantages of Sectional Vessels & Push Towing. The Second International Tug Convention, D3.1-D3.6.

Taisei Engineering Consultants Inc. Articouple-Automatic Articulate Coupler for Pusher-Barge System. BROCHURE.

Taisei Engineering Consultants Inc. Articouple-KD-Deck-Mountable Automatic Articulate Coupler for Pusher-Barge System. BROCHURE.

Teasdale, J.A. 1976. An Approach to the Design of Push-Tow Linkages. The Fourth International Tug Convention, 251-261.

Timman, R. and J.N. Newman. 1962. The Coupled Damping Coefficients of a Symmetric Ship. Journal of Ship Research, 5:4, 1-7.

Timman, R., A.J. Hermans and G.C. Hsiao. 1985. Water Waves and Ship Hydrodynamics. Delft, The Netherlands:Martinus Nijhoff Publishers.

Ursell, F. 1962. Slender Oscillating Ships at Zero Forward Speed. Journal of Fluid Mechanics, 14, 496-516.

Van Oortmerssen, G. 1979. Hydrodynamic Interaction Between Two Structures, Floating in Waves. Proceedings of the Second International Conference on the Behaviour of Offshore Structures, Paper 26, 339-356.

Vugts,J.H. 1968. The Hydrodynamic Coefficients for Swaying, Heaving and Rolling Cylinders in a Free Surface. International Shipbuilding Progress, 15, 251-276.

Wright, C. 1973. Large Tug/Barge System - An Overview. The First North American Tug Convention, 171-186.

Wu, G.X. and R. Eatock Taylor. 1990. The Hydrodynamic Force on an Oscillating Ship with Low Forward Speed. Journal of Fluid Mechanics, 211, 333-353.

Yamaguchi, T. 1985. `Twelve Years' Experience with Articouple Pusher-Barge System. The Eighth International Tug Convention, 211-226.